THE UNIVERSITY *of* EDINBURGH

Interpreting Earth's top-of-the-atmosphere broadband radiation flux variability using observations and models

Anna Mackie

THE UNIVERSITY
of EDINBURGH

Thesis submitted in fulfilment of
the requirements for the degree of
Doctor of Philosophy
to the
University of Edinburgh — 2020

Declaration

I declare that this thesis has been composed solely by myself and that it has not been submitted, either in whole or in part, in any previous application for a degree. Except where otherwise acknowledged, the work presented is entirely my own.

Anna Mackie

March 2020

Abstract

Observed broadband radiation fluxes at the top-of-the atmosphere (TOA) and at the Earth's surface are determined by a complex network of atmospheric and surface processes. It is imperative that climate models are able to accurately simulate these observed variations and relationships in order to provide confidence in projections of our future climate. In this thesis I use a combination of observations, reanalysis fields and output from global circulation models (GCMs) to interpret radiation flux variability with respect to atmospheric properties and processes, in particular clouds, atmospheric water vapour and aerosols.

I use observations and models in two ways. In Chapters 3 and 4 I evaluate model output using observations from satellite instruments and surface measurement stations to characterise the model ability to 1) recreate observed variability and 2) contrast TOA and surface radiation flux co-variability with atmospheric properties. In Chapter 5 I use satellite observations of atmospheric temperature and humidity profiles, as well as broadband radiation flux, to assess evidence of physical mechanisms which have recently been hypothesised using output from GCMs. The chapters are based on two regions of the tropics. I focus on the first of these, a region in western Africa, partly due to the presence of aerosols, such as Saharan mineral dust, and also the west African monsoon. Both of these factors have large impacts on the radiation balance and therefore make this region interesting from a radiation perspective. Additionally, west Africa is a region

vulnerable to changes in climate, having already suffered from extended droughts in the last decades. My second focus region is the tropical ocean, where changes in tropical low clouds play an important role in the TOA radiation balance, and has therefore been linked to climate model sensitivity. The spatial and temporal scales used in the studies vary dramatically, which determines both the model output evaluated and also the methods I employ.

In Chapter 3, I exploit the 2006 high frequency observational data at Niamey, Niger from the Atmospheric Radiation Measurement (ARM) Mobile Facility, the Geostationary Earth Radiation Budget (GERB) and Spinning Enhanced Visible and Infrared Imager (SEVIRI) instruments, and products from the Climate Monitoring Satellites Applications Facility (CMSAF) to evaluate daily output from the European Centre for Medium-Range Weather Forecasts (ECWMF) Integrated Forecasting System 43r1. The data available include surface, atmospheric profile and TOA measurements. By constructing multi-variate linear models of each component in the energy budget, I test their sensitivity to changes in atmospheric properties, including 2m air temperature, aerosol optical depth (AOD), cloud properties and total column water vapour (TCWV). I find that the lack of ice in clouds, manifested as a reduced ice water path (IWP) in 43r1 with respect to the estimate from CMSAF, results in too much shortwave radiation passing through the atmosphere in 43r1, and therefore too much downwelling shortwave radiation (DSR) at the surface and too little reflected shortwave radiation (RSR) at the TOA. I also identify the use of an aerosol climatology in 43r1 as a cause of discrepancy between the observation and the model in the surface fluxes, with the lower aersol loading in the model leading to a reduction in downwelling longwave radiation (DLR) and an increase in DSR. This work is published in Atmospheric Chemistry and Physics as Mackie et al. (2017).

In Chapter 4, I examine a wider region in western Africa, which I refer to as 'west Africa', which encompasses three distinct sub regions: the Sahel, the

Sahara and the south-western coastal region. As observational references, I use a range of radiation data from the TOA and surface from satellite products and surface station measurements to construct mean annual cycles with which to evaluate output from GCMs submitted to the Intergovernmental Panel on Climate Change's Coupled Model Intercomparison Project Phase 5 (CMIP5). This chapter has two aims: firstly, to compare the reference data and to establish the observational range in the targeted metrics, and secondly to evaluate how the CMIP5 multi-model mean and range fit with this range. By contrasting coupled and atmosphere-only model output, I link differences in radiation at the TOA to the models' tendency to model the west African monsoon onset too late and to model the limit of its northwards progression to too far south. By contrasting the sensitivity of the models to changes in AOD and TCWV to that of the Clouds and the Earth's Radiant Energy System Energy Balanced and Filled (CERES EBAF) product, I find some indication that DSR in the CMIP5 models may be too sensitive to changes in water vapour, and not sensitive enough to changes in AOD. This work is under review at the AGU journal Earth and Space Science.

In Chapter 5, I evaluate observational evidence for a model-based hypotheses which links tropospheric temperature and humidity changes to patterns in tropical sea surface temperature (SST) warming. The hypothesis states that if SSTs in regions of strong ascent warm relative to the tropical ocean mean, the warming is efficiently lofted to the upper troposphere. In contrast, if warming is concentrated in regions of subsidence, the effects are limited to below the inversion which is characteristic of these regions. The subsequent effects of SST warming patterns are hypothesised to be key in determining the feedbacks from low cloud, and has thus been linked to climate sensitivity. To test this hypothesis I use co-located Atmospheric Infrared Sounder (AIRS) temperature and humidity profiles and CERES radiation data, including window region data, and subset these data using vertical velocity at 500 hPa from ECMWF's ERA-Interim reanalysis. I

find some evidence which supports the hypothesised mechanism, specifically that if subsiding regions warm preferentially, there is a strong decrease in low cloud, with associated decrease in reflected shortwave radiation (RSR), and evidence that temperature increases are suppressed above the inversion. I also find small, but statistically significant, increases in humidity above the boundary layer inversion, though the origin of this is not clear. If regions of convection preferentially warm, the observations suggest that changes in relative humidity in the upper troposphere are due to changes in specific humidity rather than temperature, with temperatures in the upper troposphere relatively insensitive to relative warming. The largest changes in TOA radiation are in the longwave, which I hypothesise are linked to the observed increase in high cloud. This work is being prepared for publication.

Lay Summary

The Sun provides the energy which warms our planet, supports life and drives the Earth's atmospheric and oceanic systems. A portion of this energy is reflected back to space from the surface or atmospheric constituents, primarily clouds, while some is absorbed or scattered. The Earth also radiates energy, which either passes through the atmosphere and escapes to space, or is absorbed or scattered by the atmosphere. The atmosphere also radiates, both to space and towards the Earth. The absorption and emission of radiation by the atmosphere, largely by clouds and greenhouse gases, increases the temperature of the Earth's surface to a habitable temperature: this whole process is termed the greenhouse effect. The incoming and reflected solar radiation, also known as shortwave radiation, and the outgoing longwave radiation of the Earth and atmosphere, constitutes the Earth's radiation budget.

This radiation, or energy, budget between incoming and outgoing energy at the top-of-the-atmosphere (TOA) therefore quantifies the net energy trapped within the Earth-atmosphere system and is fundamental to our understanding of weather and climate. Climate models are computer models which approximate the Earth-atmosphere system, and are used for both improving our understanding of the climate system and, crucially, for projections of how it might change in the future. These projections can be short-term weather forecasts or for understanding how the climate system may evolve in the next years, decades or centuries. It is

therefore vital that we can demonstrate that these models are able to describe the present day energy budget, in order to have confidence in their future projections. Satellite instruments are ideal for providing the observations required for such validation, as they provide large spatial coverage over a number of decades. Radiation at the surface is harder to observe using satellite instruments, due to the assumptions and modelling required to remove the effects of the atmosphere, but a number of surface stations provide measurements which can also be used to evaluate model output.

As the radiation budget at both the TOA and the surface is highly dependent on the Earth's surface and the atmosphere, there are large variations in the contributions of longwave and shortwave radiation in both space and time. In this thesis, I study how the radiation budget differs between the observations and model output, and how variations in clouds, water vapour and aerosols (liquid or solid particles suspended in the air, for example desert dust) may be linked to the differences. For the first two research chapters, I focus on a region in western Africa, where the west African monsoon and mineral dust from the Sahara play significant roles in modulating the energy budget. I do this for two different spatial scales and two different kinds of model, depending on the type of data available. In the third research chapter I focus on the tropical ocean and evaluate observational evidence for a hypothesis which has been developed using climate models, rather than direct evaluation of the output itself.

I begin by examining the radiation budget at the surface and TOA at a particular point in the Sahel, using daily observations from a year-long measurement campaign in Niamey, Niger, in conjunction with satellite data. I compare these to output from a weather forecasting model. My aim is to quantify the influence of air temperature, water vapour, aerosol and cloud properties (in particular how much liquid and ice water there is in clouds) to the different components of the energy budget, both in the observations and the model, and try to link discrepancies

between the two. In comparison to the observations, the model has too much shortwave radiation reaching the surface, and too little reflected back to space, which I attribute to a lack of ice in the modelled clouds, and a poor representation of aerosol in the model. I also link aerosol representation to differences between longwave radiation in the observations and the model.

In Chapter 4, I widen the scope of the study to a wider west African region over 15 years, and use observational data from satellites and surface data to evaluate output from a set of 43 general circulation models (GCMs). Unlike the model evaluated in Chapter 3, these models do not assimilate observational data for their simulations, and are not designed to exactly replicate the atmosphere at a particular place or time, but rather the general patterns of behaviour. I find that the west African monsoon, as modelled by the GCMs, is a large source of difference between the models and the observations. I link this model differences to their representation of sea surface temperatures. I also find evidence that, in the case of cloud-free skies, surface radiation has different sensitivities to water vapour and aerosol in the GCMs compared to a reference data set. In particular, GCMs are generally too sensitive to changes in water vapour, and not sensitive enough to changes in aerosol.

In Chapter 5, I use satellite observations of TOA radiation as well as atmospheric temperature and humidity profiles, to understand the effects of warming in contrasting regions of the tropical ocean, relative to the warming of the tropical ocean as a whole. By subsetting the regions into those where the air is either ascending and descending, I examine how a relative warming in sea surface temperature affects the temperature and humidity of the atmosphere, and the height and quantity of cloud. I compare my findings to a hypothesis based on climate models, and find evidence supporting a decrease in low cloud if regions of descent warm relative to the rest of the tropical ocean, which is associated with a reduction in shortwave radiation to space. If ascending regions warm relatively,

however, I find that an increase in high cloud, and an associated decrease in longwave radiation to space, is the dominant effect, which is not described by the hypothesis.

Acknowledgements

Firstly, I would like to thank the Natural Environment Research Council and the E3 Doctoral Training Partnership for funding my PhD and for giving me this opportunity.

I also owe many thanks to Paul and Helen for their supervision, encouragement and support over the course of my PhD. Thanks to Paul for always making time for me, keeping me motivated and repeatedly questioning my 'big picture'. Special thanks also to Helen, who ended up being far more involved that she was perhaps expecting! Her helpful conversations, attention to detail and thoughtful questions kept me on track and enthused about the science.

My time in the Crew Attic would not have been nearly as enjoyable had it not been for the many friends I made there. The hiking and pub trips, coffee room conversation, cake and general good cheer made it a wonderful place to work - despite the temperature extremes! Bay buddies, past and present, have been particularly lovely and supportive. Of the many friends I've made, I'd like to specifically thank Claudia, Pippa, Jack, Andy, Doug, Kathleen, Jacob, Geoff and Robyn for their friendship.

I also don't think I would have managed to finish this thesis without my family and friends. Catriona, Tom, Ebby and Luke have been there from the start, have always been willing listeners when I needed a moan, and generally have been the

best friends I could ask for. My parents, too, have supported me through thick and thin with lots of helpful advice, and in recent months, precious childcare. I don't think I could have both a finished thesis and a baby without my wonderful Mum.

To Alasdair and Ellie. I can't thank Alasdair enough for his belief in me, his constant encouragement and willingness to sit through presentations which he didn't really understand. His unwavering support means the world. Finally, to Ellie, who brings so much joy. Maybe one day you'll read this.

Contents

List of Tables

List of Figures

Chapter 1

Introduction

1.1 Motivation and scientific questions

Solar radiation provides the energy which drives the Earth's climate system. The majority is absorbed by the Earth and atmosphere, but approximately a third of this energy is reflected back into space. The Earth's surface and atmosphere also emit radiation, though at longer wavelengths. At the top-of-the-atmosphere (TOA) there are three radiation components: incoming solar (often referred to as total solar irradiance/TSI), outgoing reflected solar (or reflected shortwave radiation/RSR), and thermal outgoing (or outgoing longwave radiation/OLR). Collectively, these components constitute the TOA radiation budget.

The TOA radiation budget is the culmination of countless processes and feedbacks associated within and between the atmosphere, ocean and the Earth's surface. Variability in OLR and RSR is therefore dependent on a complex network of other factors. As the Earth's radiation budget is a fundamental measure of the climate system, it is vital that climate models are able to reproduce observed behaviour and variability in order to have confidence in future climate projections. In this

thesis, the scientific questions I address are focused on two aspects: 1) interpreting observed TOA radiation variability with respect to atmospheric processes and 2) inferring modelled processes which cause observation - model differences in TOA and surface radiation fluxes. To do this, I use a combination of observational data from surface measurement stations and satellite instruments, and model output from reanalysis and general circulation models (GCMs). This thesis contains two approaches to combining observational data and model output. In the first two research chapters I evaluate model performance against observational data, while in the third research chapter I start with a concept and mechanism recently developed by others using climate models, and assess the observational evidence to support it.

The main scientific questions addressed in this thesis are:

1. **How well can TOA and surface broadband radiation fluxes be modelled over western Africa, and how are biases linked to atmospheric processes?**

   (a) Using output from two different types of model, a numerical weather prediction model (NWP) and from GCMs, what are the differences in TOA and surface fluxes as compared to observations?

   (b) To what extent can differences be linked to differences in atmospheric characteristics or processes, in particular those linked to cloud, water vapour and aerosol?

   (c) What is the influence of water vapour and atmospheric aerosol on model and observed clear-sky surface fluxes?

2. **Is there observational evidence for a model-based hypothesis linking sea surface temperature warming patterns to changes in low cloud?**

(a) How do atmospheric temperature and humidity profiles change with relative sea surface temperature (SST) warming in the tropical ocean, depending on whether the region is one of strong convection or strong subsidence?

(b) How do cloud fraction and TOA radiation fluxes change under these scenarios?

(c) Does this fit with the hypothesis of recent model-based studies (Zhou et al., 2016; Ceppi and Gregory, 2017; Andrews and Webb, 2018)?

Broadly speaking, I address the first of these questions in Chapters 3 and 4, and the second in Chapter 5. To address these questions, I examine three different domains of very different spatial scales: point observations (Niamey, Niger, Chapter 3); a land region (a region in western Africa, defined in Fig. 4.1, Chapter 4, which I refer to as 'west Africa'); and a larger, ocean region (tropical ocean, defined as all ocean between 30°S–30°N, Chapter 5). I study these particular regions for a number of reasons. I focus on west Africa and Niamey due to the strong influence of aerosols and the west African monsoon, which play an important role in the radiation budget. I study Niamey in particular due to the availability of surface observations in 2006–2007. Additionally, west Africa as a region is particularly vulnerable to changes in climate, making it important that we have confidence in climate model predictions over the region. I focus on the tropical ocean as it has been hypothesised as playing a key role in the sensitivity of the climate system to changes in atmospheric CO_2.

My analysis is at two different temporal resolutions: daily means over the course of a year (Chapter 3), and monthly means over ∼15 years (Chapters 4 and 5). Within the regions examined in the chapters, I also compare the behaviour between different areas or dynamical regimes to interpret key processes. In Chapter 4 I look at contrasting regions within west Africa (coastal region, Sahara

and the Sahel), and in Chapter 5 I subset the tropical ocean into areas of strong ascent and descent. Due to the wide range of observational data I use, as well as reanalysis, NWP and GCM output, a key consideration throughout this thesis is to what extent a derived product can be considered 'observational', what the associated uncertainty is, and how it can be used as a reference for model evaluation.

In this chapter, I begin with a very brief introduction to the Earth's radiation budget in section 1.2, including two key instruments from which I use data and the current best estimates of global annual mean values at the surface and the TOA. I then discuss factors which affect radiation variability in section 1.3, and how and why the Earth's radiation budget is modelled in section 1.4. In section 1.5 I describe Niamey, west Africa and the tropical oceans in more detail and give a brief description of how my work fits into the context of the wider research in these regions.

1.2 The Earth's radiation budget

All bodies with a temperature above absolute zero emit in the electromagnetic spectrum, and the frequency at which this radiation peaks depends on the temperature, T (in K), of the body according to Wien's law:

$$\lambda_{peak} = \frac{b}{T}, \tag{1.1}$$

where λ_{peak} is the peak wavelength and $b \approx 2989$ μK is a constant of proportionality. While the Earth's blackbody radiation temperature is $\sim$255K, and therefore peaks in the infrared at around 11μm, the sun radiates at a far hotter temperature of $\sim$6000K, and therefore the peak of the solar spectrum is $\sim$0.48 μm. While

the Sun can be approximated as a blackbody, the Earth's atmosphere significantly modulates longwave emission to space, principally through absorption and emission of radiation.

How much incident solar radiation is reflected back to space, and how much outgoing longwave radiation is emitted to space, depends on a complex system of factors such as atmospheric composition, including greenhouse gases and the presence of aerosols, surface characteristics and cloud presence and type. The measurement by satellite instruments of radiation reflected and emitted from the Earth-atmosphere system is therefore fundamental to our knowledge of atmospheric, cloud and surface properties and processes as well as providing a vital component of our long-term monitoring of climate.

1.2.1 Measuring broadband radiation fluxes from space

The studies contained in this thesis are largely based on analysis of broadband OLR and RSR. These are measured by satellite instruments, and therefore the earliest available measurements date from the the beginning of the satellite era. Figure 1.1, taken from Brindley (2016), shows the dates of key satellites measuring broadband radiation flux. The technological improvements in the 1960s revolutionised our understanding of the Earth's radiation budget by providing, for the first time, a global picture of measurement (L'Ecuyer, 2017). The first radiation budget mission using multiple instruments was the Earth Radiation Budget Experiment (ERBE, Barkstrom, 1984), launched in 1984. This, and subsequent missions, have allowed further study and refinement of the Earth's radiation budget, its components, partitioning and variability.

More recently (Fig. 1.1), three key satellite instruments have provided us with OLR and RSR measurements, two of which I use in this thesis: the Geostationary

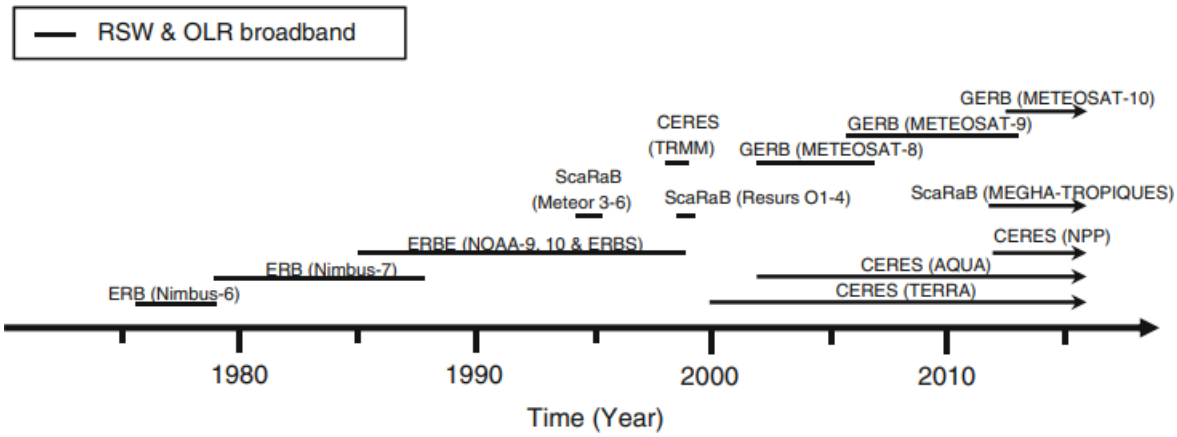

Figure 1.1: Past and current (arrows) broadband instruments, with the satellite on which they flew in parentheses. Figure taken from Brindley (2016)

Earth Radiation Balance (GERB, Harries et al., 2005) instruments on Meteosat 8–11 and the National Aeronautics and Space Administration (NASA) instruments Clouds and Earth's Radiant Energy System (CERES, Loeb et al., 2001), on the Aqua, Terra, Suomi National Polar-orbiting Partnership (NPP) and NOAA-20 platforms. As it is in geostationary orbit, GERB provides high time resolution data, with coverage over Europe and Africa. Products derived from GERB and also the high spatial resolution Spinning Enhanced Visible and Infrared Imager (SEVIRI) have been widely used for studies requiring this high resolution, for example studies of Saharan aerosol (e.g. Slingo et al., 2006; Milton et al., 2008). Through combining CERES measurements with geostationary satellites, cloud data from the Moderate Resolution Imaging Spectrometer (MODIS) and meteorological data, there are a range of CERES products available, suitable for different applications. This includes the global 1° x 1° gridded, Energy Balanced and Filled product (EBAF) (Loeb et al., 2018), which has been the basis for a large number of climate studies, especially those seeking to evaluate general circulation model (GCM) behaviour (e.g. Li et al., 2013; Dolinar et al., 2015). Chapter 2 contains a more detailed explanation of the data I use in this thesis,

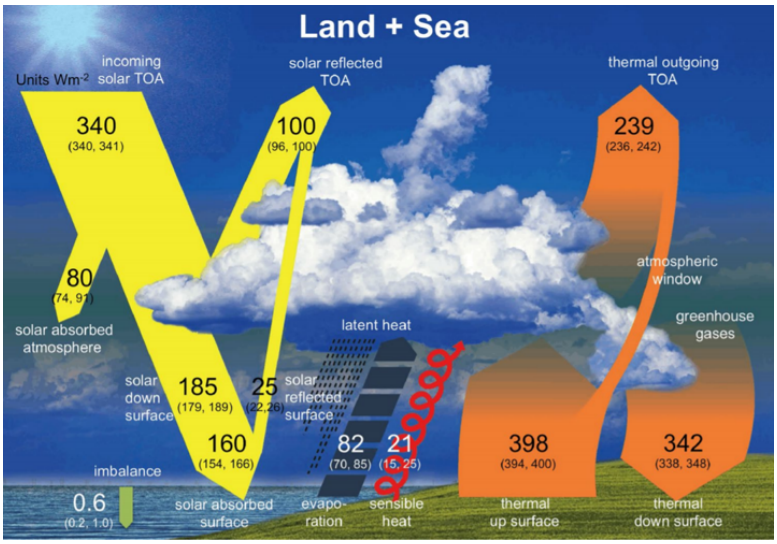

Figure 1.2: Schematic outlining the best estimates of global annual means (numbers), with associated uncertainty ranges (parentheses), of the main components of the Earth's radiation budget over land and ocean, as determined by observational data and CMIP5 models. Figure taken from Wild et al. (2015).

including radiation data from satellite instruments and in situ measurements and their relative advantages.

1.2.2 Global annual mean estimates of the Earth's energy budget

There are eight components which are often considered in energy budget studies, based on measurements of upwelling and downwelling radiation or turbulent heat fluxes at the surface, solar radiation incident at the TOA and radiation leaving the atmosphere at the TOA. Figure 1.2 shows a simplified schematic outlining these components of the surface and TOA radiation budgets, along with their best global annual mean estimates, as determined by Wild et al. (2015) and presented in the International Panel Climate Change (IPCC) Fifth Assessment Report (AR5) (Hartmann et al., 2013).

In the shortwave, the TSI measures incident solar energy, with variation across the globe a function of latitude. The annual mean in TSI is estimated to be 340 [340, 341] Wm^{-2}, with the upper and lower bounds of the uncertainty range given in square parentheses. Approximately a quarter of this shortwave radiation (75 [70, 78] Wm^{-2}) is reflected from clouds and aerosols in the Earth's atmosphere, with about 80 [74, 91]Wm^{-2} absorbed by the atmosphere. Just over half (185 [179, 189] Wm^{-2}) of the shortwave radiation reaches the Earths surface, giving another component of the radiation budget, surface downwelling shortwave radiation (DSR). The the majority of the incoming solar radiation (160 [154, 166] W^{-2}) is absorbed by the surface, and a small proportion (25 [22, 26] Wm^{-2}) is reflected, giving surface upwelling shortwave radiation (USR). This component, combined by radiation reflected by clouds and aerosols, give the total RSR at the TOA with a global annual mean of 100 [96, 100] Wm^{-2}.

The Earth itself emits longwave radiation, with the annual global mean estimated to be 398 [394, 400] Wm^{-2} in upwelling longwave radiation (ULR). Though some of this radiation passes through the window region (a portion of the the infrared spectrum where there is little atmospheric absorption), much of this is absorbed or scattered by the atmosphere, through clouds, aerosols and greenhouse gases. These, too, emit in the longwave both upwards and downwards. Therefore there is a global annual mean of 342 [338, 348] Wm^{-2} downwelling shortwave radiation (DSR) at the surface. The longwave radiation from the atmosphere, combined with the surface radiation transmitted through the atmospheric window, leads to a global annual mean of OLR of 239 [236, 242] Wm^{-2} at the TOA. Finally, the Earth's surface cools by the exchange of turbulent heat fluxes with the atmosphere, with the partitioning between sensible (SHF, 21 [15, 25]Wm^{-2}) and latent heating (LHF, 82 [70, 85]Wm^{-2}) dependent on the surface conditions, particularly soil moisture.

1.2.3 Forcings, feedbacks and climate sensitivity

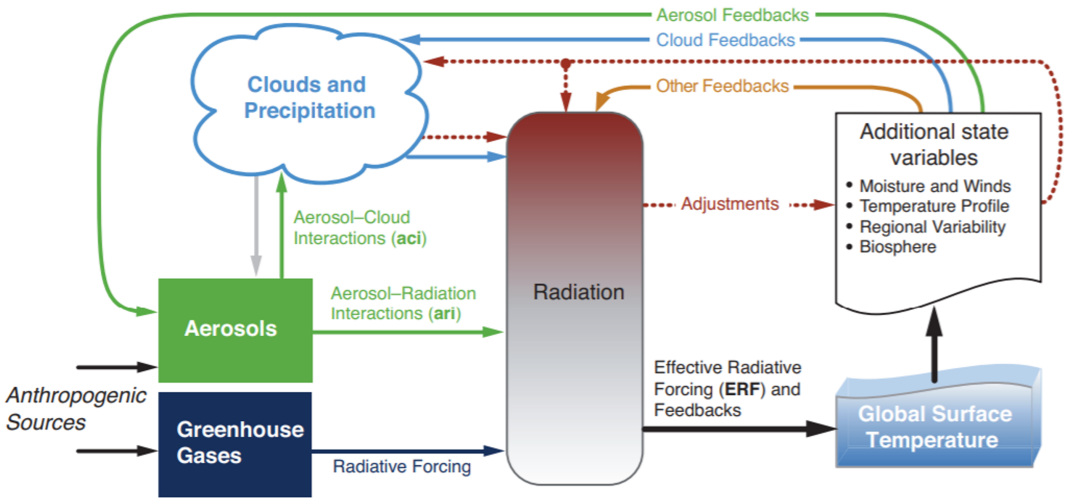

Figure 1.3: Illustration of forcings and feedbacks in the climate system, taken from Figure 7. 1 in Boucher et al. (2013). Straight lines indicate forcings, curved lines are feedbacks, and dashed lines rapid adjustments.

A simple model of the Earth-atmosphere system is one of radiative balance at the TOA between absorbed solar radiation and OLR. In this framework, any external changes to this balance are termed forcings, ΔF; these can be anthropogenic, such as the release of greenhouse gases from the burning of fossil fuels, or natural, such as changes to the solar cycle or volcanic eruptions. Any forcing changes the energy balance within the Earth-atmosphere system, creates a heat flow (ΔQ) and ultimately leads to a change in surface temperature (ΔT) as the system re-equilibriates by adjusting the OLR at the TOA. In this simple model,

$$\Delta Q = \Delta F - \lambda \Delta T, \tag{1.2}$$

where λ is the feedback parameter (Gregory et al., 2004; Knutti and Hegerl, 2008). As the system returns to a new equilibrium state, ΔQ tends to zero and then:

$$\lambda = \frac{\Delta F}{\Delta T}. \tag{1.3}$$

λ can be decomposed into feedbacks from different processes on the Earth's surface and in the atmosphere, for example feedbacks from temperature, water vapour, surface albedo and clouds, as well as land surface properties such as vegetation changes. Interactions between different aspects of the climate system, however, mean that the resulting network of forcings and feedbacks is complex. Figure 1.3, taken from the IPCC AR5 Chapter 7 (Boucher et al., 2013), is a schematic outlining some key forcings and feedbacks. Forcings such as those from aerosols and greenhouse gases, are shown with straight lines interacting directly with radiation, clouds and precipitation, which influence global surface temperatures. Rapid adjustments, which are changes in response to radiative forcing and not surface temperature, are shown with dashed arrows, and curved arrows indicate feedback loops within the system (Boucher et al., 2013).

The concept of forcings and feedbacks give a useful framework for discussing the relative impacts of perturbations to the Earth-atmosphere system, and leads directly to a metric which is key to Chapter 5, that of climate sensitivity. A common measure on the sensitivity of a GCM to forcing from CO_2 emissions is to instantaneously double the CO_2 ($\Delta F_{2\times}$), run the model to equilibrium and calculate the change in global annual mean surface temperature ($\Delta T_{2\times}$). The global climate feedback in this case, where Q in equation 1.2 tends to 0, is therefore:

$$\lambda_{2x} = \frac{\Delta F_{2\times}}{\Delta T_{2\times}}. \tag{1.4}$$

ΔT_{2x} is known as equilibrium climate sensitivity (ECS). The range of ECS values from the Coupled Model Intercomparison Project Phase 5 (CMIP5) gives the range to be $\sim$1.5-4.5K, with little recent improvement (Knutti and Hegerl, 2008; Andrews et al., 2012; Knutti et al., 2017). Indeed, initial indications from analysis of CMIP6 models suggest the revised range is wider than in CMIP5 (Zelinka et al., 2020). Uncertainties in feedbacks, particularly from those from clouds, contribute

to the spread in ECS (Bony and Dufresne, 2005; Soden and Held, 2006; Colman and McAvaney, 2011; Boucher et al., 2013; Vial et al., 2013).

1.3 Factors affecting radiation variability

While Fig. 1.2 shows global averages of radiation fluxes, there is much variability within this due to physical drivers that operate at vastly different spatial and temporal scales. The most predictable of these are variations in incident solar radiation on the Earth's surface arising from its dependence on the geometry of the Earth and its orbit. In particular, there are diurnal and seasonal cycles in all of the components of the Earth's radiation budget outlined section 1.2.2 as a consequence of surface insolation varying with time and latitude (L'Ecuyer, 2017). Solar cycles also induce cyclic variability in incident solar radiation over longer time scales, though variations are small at $\sim$0.17 Wm^{-2} (Gray et al., 2010). How much solar insolation is absorbed by the surface may itself have a seasonal cycle depending on the region. The Sahel, for example, has a significant seasonal cycle in surface albedo linked with the seasonal growth of vegetation. However, in other regions I examine in this thesis surface albedo remains largely constant throughout the year, for example in the Sahara or over the tropical oceans.

In addition to inducing cyclic variability in radiation budget components, unequal solar heating between the equator and the poles is a fundamental driver of large scale circulation over various timescales. Superimposed on these variations are the effects of physical properties of the atmosphere and surface, for example those from the presence and type of clouds or aerosols, the composition of the atmosphere, or surface characteristics such as albedo (Loeb et al., 2007). In this section I discuss major modes of variability in cloud, aerosol and water vapour.

1.3.1 Clouds

Clouds have a profound effect on the radiation budget of the Earth. Typically forming when warm, moist air rises and cools sufficiently to condense, their impact is determined by their range in characteristics and abundance (Chen et al., 2000) and complicated by their high spatial and temporal variability. In general, the net effect of clouds is to cool the Earth: broadly, the cooling effect in the shortwave from reflection of solar radiation outweighs the warming effect of clouds absorbing longwave radiation and re-emitting at lower temperatures (Stephens, 2005; Allan, 2011). Cloud radiative forcing (CRF), using the definitions of Miller et al. (2012) is the the difference between all-sky (superscript AS) and clear-sky (superscript CS) radiation flux in either the longwave (subscript LW),

$$\mathrm{CRF}_{\mathrm{LW}}^{\mathrm{TOA}} = \mathrm{OLR}^{\mathrm{AS}} - \mathrm{OLR}^{\mathrm{CS}} \tag{1.5}$$

or the shortwave (subscript SW)

$$\mathrm{CRF}_{\mathrm{SW}}^{\mathrm{TOA}} = \mathrm{RSR}^{\mathrm{AS}} - \mathrm{RSR}^{\mathrm{CS}}. \tag{1.6}$$

CRF is frequently used to determine the impact of clouds on the radiation budget: the mean global annual longwave CRF is estimated to be $\sim$-30 Wm^{-2}, and the shortwave CRF to be $\sim$50 Wm^{-2} (Boucher et al., 2013).

While the precise interaction of clouds with radiation depends on their microphysics, satellite-derived bulk properties of clouds are central to our understanding of radiative impact. Cloud type are often defined through cloud height and optical thickness (e.g., definitions from International Satellite Cloud Climatology Project or that from Hartmann et al. (1992)). Other important quantities in defining clouds include cloud fraction, cloud base pressure and temperature and liquid and ice water path (the mass of water/ice integrated over an atmospheric

column). As the emission temperature of a cloud is intrinsically linked to its altitude, this is a particularly important aspect of cloud-radiation studies (Hartmann et al., 1992). Furthermore, the radiative impact of clouds depends on whether they contain liquid water, ice, or a mixture of phases. Globally, for single phase clouds, liquid water clouds have the largest annual mean cloud radiative effect in the shortwave (-14.6 Wm^{-2}), and ice clouds, largely over the tropics, have the largest global mean cloud radiative effect in the longwave (9.3 Wm^{-2}) (Table 3, Matus and L'Ecuyer, 2017). However, mixed phase clouds, and especially multilayered clouds containing distinct layers of liquid and ice, have significant impacts on radiation budget and are expected to increase their spatial coverage with atmospheric warming (L'Ecuyer et al., 2019).

Cloud development is driven by changes in, for example, surface and atmospheric temperatures, moisture availability, topography and atmospheric dynamics, and therefore display strong modes of variability across space and time. Some of this variability is linked to the diurnal and annual cycles in solar radiation. Diurnal cycles in incident solar radiation drive changes in surface temperature, sensible heat flux and subsequently in cloud development. The differences in the peak of these cycles determine the diurnal variations of OLR and RSR. For example, in the longwave, the peak of emitted thermal radiation from the surface lags that of solar radiation as the surface warms. Convective cloud development peaks later in the day still (Taylor, 2012; Comer et al., 2007; Gristey et al., 2018), affecting the longwave cloud radiative forcing. Annual cycles in solar radiation also induce seasonal variability in clouds (e.g., Mlynczak et al., 2011) and there are also longer-term variations, linked to, for example, large-scale atmospheric oscillations, such as the El Niño Southern Oscillation (ENSO) (e.g., Cess et al., 2001).

Despite these modes of variability, cloud development can be highly dependent on local meteorological and topographical factors, leading also to high frequency

variations in space and time. This complexity in properties and feedbacks of clouds results in the need for simplifications and parameterisations in climate models (see section 1.4). Clouds are therefore responsible for much of the spread in ECS and a large source of uncertainty in the projections of current GCMs (Bony and Dufresne, 2005; Boucher et al., 2013; Vial et al., 2013).

1.3.2 Aerosols

Aerosols are liquid or solid particulates suspended in air, and can be either directly emitted (primary aerosols), or formed through chemical reactions (secondary aerosols). They occur from both natural sources, such as deserts, fires, ocean spray and volcanoes, and anthropogenic sources, such as the burning of fossil fuels or other industrial processes (Boucher et al., 2013). Aerosols directly affect the radiation budget by absorbing or scattering shortwave and longwave radiation.

Aerosols also have indirect effects through their interactions with clouds: the presence of aerosols reduce cloud droplet effective radius for the same amount of liquid water, thereby increasing cloud albedo (Twomey, 1974) and inhibiting precipitation and thus increasing cloud liquid water and further increasing albedo (Albrecht, 1989). Aerosol-cloud interactions are complex and are therefore one of the largest sources of uncertainty in radiative forcing (Boucher et al., 2013). While the influence of anthropogenic aerosols on some cloud properties is relatively well constrained, such as on liquid cloud droplet number concentration, other impacts, such as on cloud water content and cloud forcing, are less clear due to compounding influences from meteorological factors (Gryspeerdt et al., 2016; Bellouin et al., 2020). Finally, aerosols can also have an effect on the surface albedo, for example by settling on snow or ice and thus reducing the reflectively of the surface in the shortwave (e.g. Qian et al., 2015).

The effect of aerosols on radiation subsequently depends on a range of factors including their type, composition, mixing state, the presence of and type of cloud, and their vertical distribution. In the IPCC AR5 Chapter 7, global aerosol radiative forcing was estimated to be 0.45 (0.95 to +0.05) Wm^{-2} (Boucher et al., 2013), though more recently this range has been revised -2.0 to 0.4 Wm^{-2} (Bellouin et al., 2020).

In this thesis my examination of aerosol is limited to those relevant for the west African region. In this region, key aerosols are mineral dust originating from the Sahara (Slingo et al., 2006; McFarlane et al., 2009) and those from the burning of biomass (Johnson et al., 2008). The key radiative effects of mineral dust are to reduce the shortwave radiation reaching the surface through scattering and to absorb longwave radiation, and the key effect of black carbon from biomass burning is the absorption of shortwave radiation (Milton et al., 2008; Boucher et al., 2013). Concentrations of these aerosols have high frequency variability, with increases due to dust storms or fires (Slingo et al., 2006). Instances of these events, however, arise in specific seasons due to seasonal changes and large-scale dynamics such as the west African monsoon, and lead to a distinct seasonal cycle in aerosol optical depth. Therefore, aerosol variability is directly linked to radiative flux variability, both at the surface (e.g. Milton et al., 2008) and the TOA (e.g. Brindley, 2007).

1.3.3 Water vapour

Water vapour is the most important greenhouse gas, due to its relative transparency to shortwave radiation and its strong absorption of longwave radiation (Held and Soden, 2000). In this thesis, I use three variables which quantify atmospheric water vapour: 1) specific humidity, which gives the concentration of water vapour molecules in an air parcel with units of g kg^{-1}; 2) total column

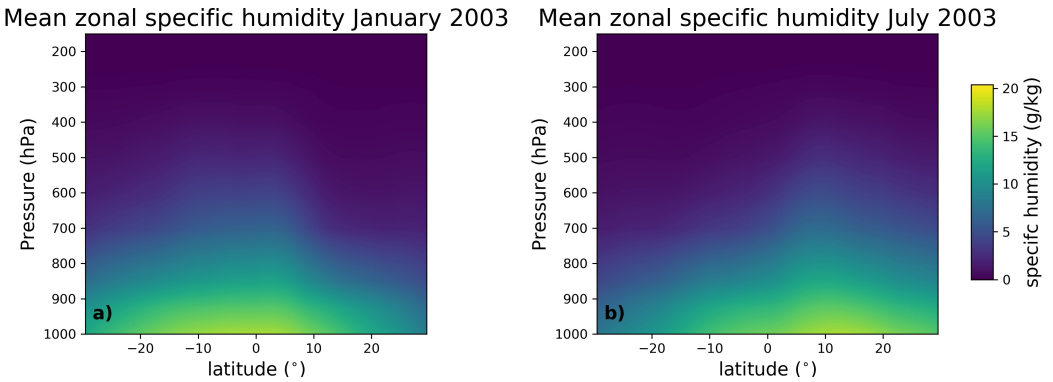

Figure 1.4: Zonal mean of specific humidity in a) January and b) July 2003, from the Atmospheric Infrared Sounder (AIRS) on *Aqua*.

water vapour (TCWV) which is specific humidity integrated over an atmospheric column and given in units of height if the vapour were condensed and spread evenly across the column; 3) and relative humidity, which gives the proportion of water vapour held by an air parcel with respect to if it were saturated, given as a percentage. Relative humidity is therefore temperature dependent and governed by the Clausius-Clapeyron equation. This relation links the saturation vapour pressure, e_s, of an air parcel to its temperature, T:

$$\frac{1}{e_s}\frac{de_s}{dT} = \frac{L_v}{R_v T^2}, \tag{1.7}$$

where L_v and R_v are the latent heat of vapourisation and gas constant, respectively. For the temperature range at the Earth's surface, this corresponds to an increase of TCWV of approximately $7\%\mathrm{K}^{-1}$ (O'Gorman and Muller, 2010).

As water vapour absorbs in the longwave and contributes to the greenhouse effect, an increase in atmospheric water vapour at a fixed temperature causes more surface emission to be absorbed, resulting in an increase in atmospheric temperature and a reduction in OLR. Due to the Clausius-Clapeyron relation, warming increases the potential of an air parcel to hold vapour, thus further increasing warming: a positive feedback (Allan et al., 1999; Held and Soden,

2000). However, this effect depends on other atmospheric conditions, including temperature profiles and the presence of cloud.

The distribution and transport of water vapour in the atmosphere is a key aspect in its modulation of the Earth's radiation budget, and interannual, seasonal and higher frequency variability in water vapour is a significant factor in determining variability in OLR and RSR. Solar heating causes evaporation of ocean water in the deep tropics, which is lofted vertically in the atmosphere where it is transported poleward, cools and subsides as part of Hadley circulation. Figure 1.4 gives the zonal mean specific humidity of the tropics in January and June 2003, and shows how the vast majority of water vapour is in the lowest levels of the troposphere. Near the equator, this water vapour extends upwards to ∼500 hPa, but polewards of this there exist very dry regions above 700 hPa. The difference between January and July demonstrates the seasonal shift north- and southwards with the inter-tropical convergence zone (ITCZ), and the seasonal cycle in water vapour is therefore closely linked with large scale dynamics. The formation of clouds is also closely linked with the availability of water vapour, with associated radiative effects (Fasullo and Trenberth, 2012).

In summary, all of the above factors, amongst others, exert influence over TOA and surface radiation flux magnitude and variability. However, these are not independent drivers, and instead form part of an interlinked web of forcing and feedback, with many superimposed modes of variability. Disentangling these effects is challenging and requires simultaneous evaluation and consideration of different processes.

1.4 Modelling the Earth's radiation budget

It is vital that we are able to have confidence in model projections, not only for forecasting models for short-term weather but particularly for projections of future climate change. In order to have this confidence we must evaluate models against observations to demonstrate that models are able to reproduce the behaviour of our past and current climate. As described above, the Earth's TOA radiation budget, a fundamental variable of the Earth-atmosphere system, is determined by the evolution and interaction of many different processes and feedback, and this presents a challenge for climate models. In sections 1.4.1 and 1.4.2 I discuss climate models and their evaluation more generally, with section 1.4.3 focusing on the modelling of the Earth's radiation budget and challenges within this area.

1.4.1 Model construction and uncertainty

The building blocks of climate models are the conservation of mass, energy and momentum as well as the gas law (Washington and Parkinson, 2005). These are then simplified to represent large-scale atmospheric dynamics and approximated into discrete grid boxes and timesteps (Randall et al., 2007). Depending on the type of model, observational data may be used either as initial or boundary conditions for a model simulation, or regularly assimilated into the model. Similarly dependent on the purpose of the model, the model will then output variables at specified spatial and time intervals.

Many of the important processes are of a sub-grid scale to that used by most GCMs, requiring the use of parameterisations and assumptions. Parameterisations are the replacement of a process which is too small to be explicitly resolved on the model grid size with a simplified property of the grid, for example assigning a grid box a value for cloud fraction. They can also be used for more effective use

of computing resources. These can then be 'tuned' by adjusting the value of the parameterisation to optimise the model output to observations. Randall et al. (2007) lists two constraints on tuning. First, the value of the parameters must be within the observational range, and secondly, the tuned parameter cannot then be used for evaluation.

A fundamental aspect of climate models is their uncertainty. All models are inherently uncertain due to their construction on incomplete information and representation of a natural system (Maslin and Austin, 2012). Model uncertainty can stem from a wide variety of sources. As Knutti et al. (2010) discuss, uncertainty can arise from: model boundary or initial conditions and paramaterisations; theoretical understanding of physical processes; description of a process in a model; missing processes; and uncertainty in future scenarios determined by political decisions. In this way, models merely give a prediction of probable events rather than a realistic representation of the Earth system. However, increasing the complexity of climate models, and encompassing more detail in physical processes, does not necessarily lead to a reduction in uncertainty (Maslin and Austin, 2012). Care must be taken, therefore, to evaluate models within this probabilistic context, taking into account that validation will only ever be partial (Oreskes et al., 1994).

1.4.2 Why do we need climate models and how can they be evaluated?

Despite this uncertainty, climate models make up an integral part of how we understand the past, current and future climate. One of the most high-profile uses of model output is the use of weather forecasting models to understand likely short-term, localised weather. Such models are in constant global use in decision making, with users ranging from governments to individuals. Similarly, climate

projections from GCMs can be used to inform policy ranging from industrial emissions to land use, and have played an instrumental role in intergovernmental agreements through simulations of different scenarios. Aside from giving some insight to likely outcomes of policy decisions, climate models offer other advantages which complement study of observations. For example, they allow for experiments and hypothesis testing of impossible situations which may be useful for other aspects of climate science (see, for example climate sensitivity in section 1.2.3). Additionally, despite recent advances in observational coverage from satellite instruments, there are many aspects of the climate which cannot be studied without climate model output. Examples of this include vertical velocity at 500hPa at 1° x 1°, as I use in Chapter 5, which is not yet observationally possible on a global scale.

The range of uses of climate model output requires many different approaches to their evaluation. Choices for which aspect of a model is being evaluated are crucial: for example, the outcome of a model evaluation may differ on the variable selected or the spatial and temporal scale at which it is evaluated. Gleckler et al. (2008) argue that the application is important in model evaluation, and that it is difficult to construct a 'one size fits all' metric for assessing models.

One method to mitigate against the inherent uncertainty of models and inter-model differences is to evaluate several climate models against observations, for example by calculating a multi-model mean, or to analyse model spread. This approach does not entirely remove the issue of individual model evaluation, raising as it does the question of model weighting or ranking within analyses, but the basic approach is that confidence in a particular model behaviour increases if it is seen in a number of independent models. Taking a multi-model approach can reduce both the effect of internal model variability on evaluation and the impact of extreme events (Gleckler et al., 2008). It is this 'stabilising' effect, however, that leads Bellprat and Doblas-Reyes (2016) to argue that an over-reliance on

multi-model means results in those extreme events being poorly predicted. A multi-model approach may also result in error cancellation: for example if one model overestimates a particular variable, this may be offset in a multi-model mean by underestimation in another model. This error cancellation can be seen either as mitigating against model differences (the argument that taking a mean across a larger number of independent models reduces uncertainty), or as masking model problems. In their wider discussion on the challenges in using multi-model ensembles for climate projections, Knutti et al. (2010) highlight that models are similar enough to correlate in their biases, and therefore argue that the assumption of model independence leads to overconfidence when using a multi-model approach.

While there are numerous difficulties in the evaluation of models, their utility in understanding the present and past climate, and particularly their projections for future climates, are unarguably central to climate studies. However, analysis of model output needs to be performed within the context of the challenges listed above. The central question of any model evaluation should therefore be to ask what is hoped to be gained from the evaluation. As Knutti et al. (2010) state: "we should not expect perfect accuracy from models, but we can be satisfied with models that are adequate for a particular purpose".

1.4.3 The Earth's radiation budget in climate models

Climate models use radiative transfer principles to simulate surface and TOA broadband radiation. Radiative transfer simulates the propagation of longwave and shortwave radiation through layers of the atmosphere, taking atmospheric conditions (e.g. trace gases, clouds, aerosols, temperature and humidity) into account. Specifically, their aim is to simulate the effects of absorption, transmission and scattering of radiation by the atmosphere. The most accurate way to

simulate radiance in the atmosphere is through line-by-line simulations, which account for the line parameters of each spectral line associated with each atmospheric gas considered in a given simulation to calculate radiances at very high spectral resolution. This can then be spectrally integrated across the region of interest - in the case of Earth radiation budget studies, the longwave and shortwave part of the spectrum. This is computationally expensive, and climate models therefore use a band transmission radiation code, where the calculation is done over a band of wavelengths rather than a line (Harrison et al., 1994). These take atmospheric conditions into account and are calibrated against line-by-line calculations, though there are often significant discrepancies (Collins et al., 2006; Oreopoulos and Mlawer, 2010). In particular, though pristine, clear-sky conditions are generally accepted to be well simulated by modern climate models, the introduction of aerosols and clouds complicate radiative transfer (Hartmann, 1994). It is therefore important that GCM radiation fields are evaluated against complex, real-world conditions (Oreopoulos and Mlawer, 2010).

1.4.4 Modelling challenges addressed in this thesis

There are many studies evaluating the ability of GCMs to reproduce the characteristics of the Earth's radiation budget. While NWP models are not intended for global Earth radiation budget studies, they share many characteristics, and therefore difficulties, with GCMs. Broadly speaking, in comparison to satellite observations, GCMs included in CMIP5 overestimate the solar radiation reaching the surface, underestimate the solar radiation reflected back to space at the TOA and tend to overestimate OLR (Li et al., 2013; Dolinar et al., 2015). The causes of these biases are complex, and in this thesis I focus on a few key themes. In particular, I examine modelled surface and TOA radiation fluxes with respect to aerosols, water vapour and clouds.

As discussed in section 1.3, clouds have a profound effect on radiation. Their complexity requires assumptions and parameterisations in their representation, and therefore they remain one of the largest sources of uncertainty in climate models (Stephens, 2005; Flato et al., 2013). Marine stratocumulus clouds in particular have been linked to differences in model climate sensitivity (Bony and Dufresne, 2005; Vial et al., 2013). Dolinar et al. (2015) evaluate the global mean radiative effects of clouds in CMIP5 with respect to satellite observations. They find that cloud fraction tends to be underestimated by the CMIP5 models, and that the net cooling effect of clouds tends to be overestimated. In the tropics, while the regional mean cloud radiative effect agree with observations reasonably well, this is due to compensating errors between regions of strong convection and subsidence (Wang and Su, 2013). Decadal tropical changes in radiation budget which are not well captured by GCMs have also been linked to clouds (Wielicki et al., 2002). The representation of clouds is addressed in all three of the research chapters of this thesis: in Chapter 3 I focus on the the liquid and ice water content in a NWP model; in Chapter 4, the cloud radiative effects in CMIP5 models; and in Chapter 5 I evaluate the effect of changes in sea surface temperature to low cloud and TOA radiation fluxes.

GCMs often use relative humidity as a parameterisation for cloud processes (Fasullo and Trenberth, 2012), with the representation of water vapour and clouds in models intrinsically linked. Aside from the direct connection with clouds, water vapour also impacts radiation through the water vapour feedback, as discussed in section 1.3. In general, most GCMs have a dry bias with respect to satellite observations in the tropical lower troposphere, and a moist bias in the upper troposphere (Pierce et al., 2006), though observational uncertainty is large (Tian et al., 2013). I consider radiation fluxes with respect to modelled water vapour, either as total column integrations or profiles, in all three of Chapters 3, 4 and 5.

Finally, aerosols are another major source of uncertainty in climate modelling

(Myhre et al., 2013). As with clouds, many assumptions are required to include aerosols in climate models. Examples of simplifications or parameterisations include the type of aerosols represented; size distributions; microphysical processes such as deposition; and interactions with clouds (see e.g. Glassmeier et al. (2017) for a more comprehensive list). One aspect of aerosol representation in GCMs is whether they use an aerosol climatology or an interactive or semi-interactive aerosol scheme (Taylor et al., 2012; Flato et al., 2013), whereby aerosol is linked to other physical processes e.g. the creation of dust aerosol by wind. Generally, GCMs underestimate the global aerosol optical depth, with CMIP5 models underestimating aerosol optical depth at 550nm by approximately 20% over significant proportions of global land surface (Flato et al., 2013). I examine the impact of model representation of aerosol on radiation fluxes in Chapters 3 and 4.

1.5 Regions examined and context of work

In each of the chapters, my work is focused on a specific geographic region, all within the tropics (30°S - 30°N). Two are land regions in west Africa: the first is the single point of Niamey, Niger, and the second a wider region (5–30°N, 15°W–20°E), illustrated in Chapter 4, Fig. 4.1, which I refer to as 'west Africa'. In Chapter 5, my focus is on the tropical ocean. While I describe the regions in more detail in the introductions to the individual chapters, in this section I provide a brief overview of the regions, including previous radiation budget studies and open scientific questions.

1.5.1 Niamey

Niamey (13°29'N, 2°11'E) is located in the Sahel, a semi-arid region south of the Sahara. It is a region with strong seasonal contrasts between the wet season (approximately April to October) and the dry season, determined by the west African monsoon (WAM). The WAM is associated with increased cloudiness, humidity and precipitation (Slingo et al., 2008), as well as significant changes in surface characteristics: dry and dusty in the dry season, the wet season brings a increase in vegetation which reduces albedo (McFarlane et al., 2009). The deep convective clouds associated with the WAM and the presence of aerosols, largely mineral dust but also from the burning of biomass, make Niamey an interesting case study for the radiative effects of these factors.

As well as this, the Sahel is a region which has experienced severe drought in the last decades (Zeng, 2003), with longer dry spells projected in the future (Sylla et al., 2016). It is therefore important that we are able to demonstrate climate models' ability to simulate the present day observed radiation budget at the TOA and surface, in order to have confidence in future projections of this vulnerable region.

A surface measurement campaign in Niamey during 2006–2007, detailed in Chapter 2, provides high frequency measurements of a range of variables related to the radiation budget. This data has been extensively used in previous research, though the wealth of data available gives plenty of scope for further work. While there are studies which examine the radiation fluxes and divergences with respect to aerosol and water vapour variables, notably Slingo et al. (2009), and studies which aim to quantify their relative effects through construction of multivariate models (Miller et al., 2009), these have not been systematically combined for each component of the radiation budget. Additionally, while the data has been used in model evaluation studies, (e.g. Milton et al., 2008; Agustí-Panareda et al., 2010),

there has been limited work quantifying the relative effects of discrepancies in atmospheric variables on the radiative fluxes.

1.5.2 West Africa

The wider west African region encompasses contrasting sub-regions. In addition to the Sahel, it contains the Sahara, an arid region which is generally dry and dusty with a high albedo, and where the radiation budget is significantly modulated by clouds, dust and water vapour (Marsham et al., 2016). The climate of the south west coastal region of western Africa is significantly different, with far more vegetation and a greater influence from the WAM. The annual progression of the monsoon northwards over the coastal region results in a 'little dry season' in the coastal region, before the monsoon retreat passes overhead again as it retreats (Adejuwon and Odekunle, 2006). The coastal region, a major population centre, has complex interactions between clouds, dynamics and aerosols from both natural and anthropogenic sources, and has therefore been the subject of a coordinated research project, the Dynamics-Aerosol-Chemistry-Cloud Interactions in West Africa (DACCIWA) project (Knippertz et al., 2015a,b; Hill et al., 2016).

While there have been studies evaluating GCMs in these regions (e.g. Miller et al., 2012; Roehrig et al., 2013), including studies using a range of observational data (Hill et al., 2016), my work in this thesis focuses on establishing an observational reference range for the mean annual cycle in TOA and surface radiation fluxes and using this to evaluate GCM behaviour in the contrasting sub-regions. Further to this, I also contrast the sensitivity of radiation fluxes in GCMs with aerosols/water vapour to one of the references (EBAF/SYN1deg).

1.5.3 Tropical ocean

The tropical oceans are an important driver of atmospheric circulation. The unequal heating of the Earth, with stronger heating at the equator, coupled with the Earth's rotation, leads to global circulation patterns characterised by the ascension, latitudinal transport, and subsidence of air (Ahrens, 2007). In the tropics, solar heating at the equator leads to strong convection over the warm ocean. Air is then transported polewards aloft, to subside in cooler, subsidence regions. These subsidence regions are associated with strong lower-tropospheric stability, often with a temperature inversion at the top of the boundary layer, and extensive marine stratocumulus (Wood and Bretherton, 2006).

Through feedbacks associated with evolving SST warming patterns, especially those associated with low clouds, the tropical ocean is believed to play a key role in the sensitivity of the climate system (see section 1.2.3). An important factor is whether relative warming occurs in either convecting or subsiding regions of the tropics (Andrews et al., 2015; Zhou et al., 2016, 2017; Andrews and Webb, 2018). However, the majority of these studies are based on climate model experiments, and study of observations has thus far been limited to qualitative comparisons (Ceppi and Gregory, 2017). Therefore, the question to what extent the specific mechanism involved can be observed remains open and is the subject of my study.

1.6 Thesis layout

In summary, in this thesis I interpret TOA and surface radiation fluxes with respect to atmospheric processes using a mixture of both observations and models. Through examining different spatial and temporal scales and using different methodologies I a) examine to what extent different processes influence and

modulate radiation fluxes and b) infer or attribute observation - model differences to modelled processes or model sensitivity to processes.

As the range of observational data and model output used in this thesis is key to my thesis, Chapter 2 contains an overview of the data used. The themes of my thesis, as outlined in section 1.1, are addressed in three research chapters. Each research chapter is in the format of a research article, and contains an overview of specific relevant literature for the chapter, a description of the region examined and details of the data used, as well as the methodology, results and conclusions of the chapter.

Finally, Chapter 6 draws together the conclusions of the separate research chapters with a critical discussion of the methodology and results of this thesis.

Chapter 2

Observational data and model output used

In this thesis, I use a number of different data products to explore the variability and co-variability between properties of the atmosphere and top-of-the-atmosphere (TOA) and surface broadband radiation fluxes. The range of data used, and the differences in their measurement technique, processing or retrieval is a central part of this thesis and therefore merits some discussion. In this chapter, I introduce and give some background to the data used in Chapters 3, 4 and 5.

For these studies, I investigate the relationships between the following variables: TOA and surface broadband radiation flux; atmospheric properties such as atmospheric temperature and humidity profiles and total column water vapour; cloud proprieties such as cloud fraction and ice- and liquid water path; surface characteristics such as albedo and greenness indices; and aerosol properties such as aerosol optical depth. There are three main sources of observational data available for such variables, those from surface measurement stations, from surface

instruments and sonde ascents, and satellite derived variables. These sources have different advantages. Surface stations provide measurements for a specific place and time, and although sites are carefully chosen to be as representative as possible of the wider region, they provide point measurements. Their number is necessarily limited, leading to poor spatial coverage, and this coverage is often particularly poor in areas of low population, or outside of North America and Europe. Satellite data, on the other hand, provides large spatial coverage which is not dependent on local factors such as accessibility. However, data are typically area-averaged, over sometimes large grid sizes: for example, 1° latitude is approximately 110 km at the equator. Furthermore, depending on the variable, satellite-derived data often require a number of assumptions and processing, for example about atmospheric and cloud properties, and use of radiative transfer models. For polar orbits, satellite overpass times mean that assumptions are also required to fill gaps between observations, in order to obtain data products such as daily and monthly means. While variables obtained from instruments on geostationary satellites do not suffer from this issue, the spatial region sampled is necessarily limited. Instrument downtime can affect both surface and satellite data. Moreover, some variables are simply very difficult to measure. In these cases, reanalyses, the optimal merging of model and observational data via data assimilation using a fixed underlying model (see section 2.4.1), can be useful. Often used in the place of observations, they are nonetheless model-based.

In this Chapter, I begin by describing data products I use which are 'purely observational', namely those measured in-situ from surface measurements stations. I then move on to discuss satellite-retrieved measurements, starting with TOA broadband radiation fluxes. Next, I discuss satellite products which require more processing, for example, for surface radiation fluxes, followed by the model output I use from reanalysis and general circulation models.

2.1 Surface observations

The 'gold standard' for surface observations are in-situ measurements made at surface measurement stations, for which there are a number of observing networks and archives of surface radiation and other relevant variables.

For surface radiation, two networks in particular provide continuous, long-term datasets of downwelling shortwave and longwave radiation. The Baseline Surface Radiation Network (BSRN, Ohmura et al., 1998) has 63 sites worldwide, with some stations recording since the early 1990s at high (up to 1 minute) temporal frequency. Similarly, the Atmospheric Radiation Measurement (ARM) program, as well as running three permanent sites, have three mobile units which are used for temporary measurement campaigns in different locations. As well as radiation measurements, a range of co-incident measurements are made of surface and atmospheric properties, providing extensive data for a particular location over a limited time period. These surface radiation data, as well as those from other institutions such as national meteorological agencies, are collected in the Global Energy Balance Archive (GEBA, Wild et al., 2017). GEBA is a database of approximately 2500 sites, recording monthly means of surface radiation, with the earliest records from 1919.

An extensive network also exists for the measurement of aerosol optical depth (AOD), the Aerosol Robotic Network (AERONET, Holben et al., 1998) which provides data for a diverse range of aerosol regimes. AERONET also provides column water vapour estimates. These are accepted to have a dry bias with respect to the more accurate Global Positioning Satellite (GPS) retrievals (Pérez-Ramírez et al., 2014), though GPS humidity data is not yet widely enough available for the analysis here.

In this thesis, I use surface measurement data from several measurement sites. In

Chapter 3, I make extensive use of the ARM Mobile Facility (AMF) data from Niamey, Niger, in 2006–2007, including surface shortwave and longwave radiation, 2 m air temperature, turbulent heat fluxes and humidity and temperature vertical profiles from sonde ascents. I also use co-incident AOD data from the AERONET site at Niamey. In Chapter 4, I use surface radiation data from the BSRN sites Tamanrasset, Algeria (22.8°N, 5.5°W) and Ilorin, Nigeria (8.5°N, 4.6°W). These are also AERONET sites, therefore I also use AOD and TCWV data from these sites, as well as from two other AERONET sites Banizoumbou, Niger (12.2°N, 1.4°W) and Ouagadougou, Burkina Faso (13.5°N, 2.7°W). These sites are all shown in Chapter 4, Fig. 4.1.

2.2 Satellite observations

Satellite-retrieved products are classified by processing level. Briefly, these are:

- **Level 0:** raw, unprocessed instrument data
- **Level 1A/1B:** ancillary information added, data processed to sensor units
- **Level 2:** data processed to geophysical variable
- **Level 3:** data spatially processed onto a uniform grid, temporally processed (e.g. to monthly mean)
- **Level 4:** data is further processed, for example with model input, or in conjunction with data from other sources

The majority of the data I use are level 3 and level 4 data products, which have had extensive quality control, spatial and temporal averaging. I use data from three main satellite instruments: the Geostationary Earth Radiation Budget (GERB)

and the Spinning Enhanced Visible and Infrared Imager (SEVIRI) instruments; The Clouds and the Earth's Radiant Energy System (CERES) instruments and the Atmospheric Infrared Sounder (AIRS).

2.2.1 The Geostationary Earth Radiation Budget and Spinning Enhanced Visible and Infrared Imager instruments

The GERB instruments are broadband radiometers, in operation on the Meteosat 8–11 satellites. These are in geostationary orbit: an orbit above the Earth's equator, at the speed of the Earth's rotation, allowing them to continuously monitor a particular location of the Earth's surface. The GERB instruments are in orbit above approximately 0°N, 0°W, with the exception of GERB2 which is above 3.5°W. GERB provides data 2005–2014, with three different instruments (1st January 2005 – 8th January 2007; 9th January 2007–22nd January 2013; 23rd January 2013–31st December 2014). For the GERB instruments, shortwave radiation is defined as radiation between 0.32-4μm, and longwave radiation as 4-100μm. GERB's 256 pixels are arranged into a linear array in the North-South direction, parallel to the axis of rotation of the platform. A full scan is completed in approximately 3 minutes, over an effective grid of 256 (N-S) x 282 (E-W) pixels. Alternate scans measure either 'total' radiation at all wavelengths or radiation which is passed through a quartz filter which effectively blocks longwave radiation. It takes approximately 6 minutes to scan both bands of total and SW radiances, and does so at a spatial resolution of approximately 50 km at nadir (Harries et al., 2005). Longwave radiation is calculated through subtraction of shortwave from total.

The primary instrument on the Meteosat 8-11 satellites is SEVIRI, a narrowband

instrument used extensively in NWP and is also used as auxiliary instrument for the GERB data processing through scene identification and resolution enhancement (Dewitte et al., 2008). SEVIRI consists of 12 narrowband channels: 11 of these channels take images of the full disk, approximately every 15 minutes, by taking 1250 scan lines with three detectors, while the 12th, a high resolution visible (HRV) broadband channel (0.4-1.1μm), measures with nine detectors every 12 minutes (Schmetz et al., 2002).

The broadband radiances from GERB/SEVIRI are first unfiltered to account for the spectral response of the instrument, then converted to radiation fluxes using scene-dependent angular dependency models, before being processed into higher level data products (Dewitte et al., 2008). I use two data products from both GERB and SEVIRI: in Chapter 3 I use the GERB-like High Resolution (HR) product, and in Chapter 4 I use the GERB/SEVIRI TOA radiation product from the Climate Monitoring Satellite Application Facility (CMSAF).

GERB-like HR

The GERB-like High Resolution (GERB-like HR) product uses observations from SEVIRI to estimate broadband fluxes at the resolution of a spatial resolution of 3 x 3 SEVIRI pixels. GERB-like HR has a temporal resolution of 15 minutes and a spatial resolution of 10km at nadir (Dewitte et al., 2008). The GERB-like HR product has the advantage of being available throughout the year including when the GERB instrument avoids direct solar illumination during the night at the spring and autumn equinoxes through scheduled shutdowns. GERB-like HR is also used in the production of other GERB/SEVIRI products, such as the CMSAF detailed below. Their role in the processing scheme is shown in red in Fig. 2.1, adapted from Clerbaux (2016).

CMSAF GERB/SEVIRI TOA radiation products

The other GERB/SEVIRI derived products used in this thesis are the level 3 monthly mean fields of OLR and RSR from the CMSAF TOA Radiation GERB/SEVIRI Data Record (Clerbaux et al., 2017). This product combines GERB level 2 measurements with SEVIRI level 1.5 measurements, as shown in Fig. 2.1, to estimate the OLR and RSR at the TOA. The CMSAF CLoud property dAtAset using SEVIRI, Edition 2 (CLAAS-2) cloud mask, also derivied from SEVIRI (Benas et al., 2017) also allows for estimation of clear-sky fluxes (Fig. 2.1). These estimates are then used to calculate the monthly means, which are then regridded onto a latitude-longitude grid.

2.2.2 The Clouds and Earth's Radiant Energy System top-of-the-atmosphere radiation products

CERES provides an extensively used suite of data products for studying the radiation balance at the TOA and surface. The purpose of CERES instruments is to provide stable, long-term data for studying the Earth's radiation balance, particularly the radiative effect of clouds (Wielicki et al., 1996). To obtain both high quality spatial and angular sampling, one of the CERES instruments is in cross-track mode, scanning perpendicular relative to the path of the satellite, and another can be in rotating azimuth scanning mode, scanning at a range of angles to the satellite's path. This provides a range of viewing angles for better understanding of the angular distribution of the radiation field (Su et al., 2015). Current CERES instruments are on the sun synchronous Aqua, Terra, Suomi National Polar-Oribiting Partnership (SNOP) and NOAA-20 satellites, and together they provide data from March 2000 to the present day. The sun-synchronous orbit allows sampling of the same local time each day as the satellites

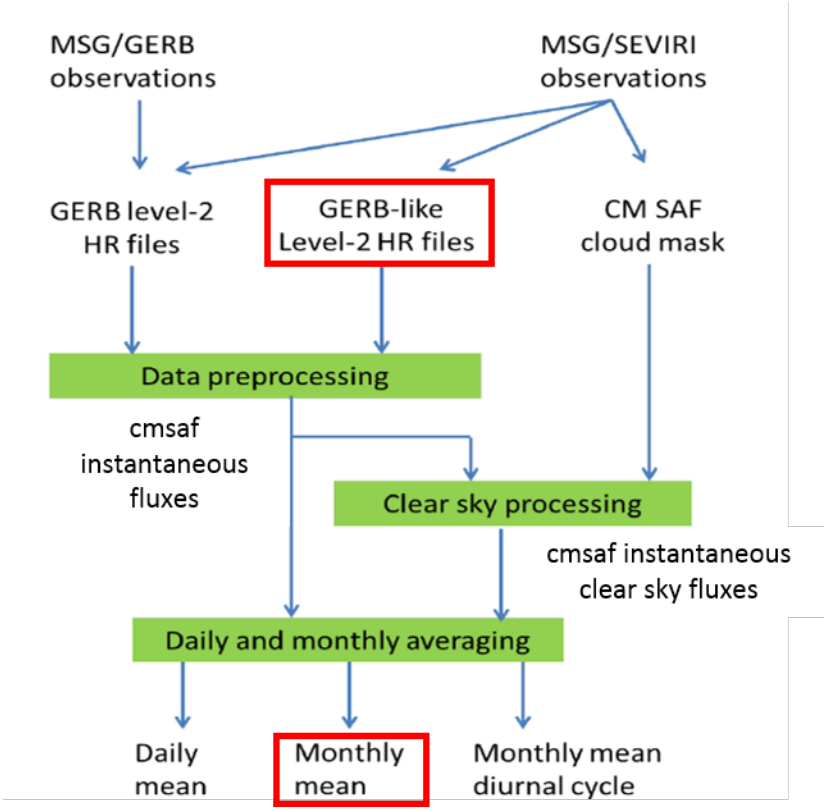

Figure 2.1: Schematic showing the main processing steps to estimate TOA broadband radiation from GERB/SEVIRI. Indicated in red are the GERB-like HR product used in Chapter 3 and monthly mean product in Chapter 4. Adapted from Clerbaux (2016).

pass overhead. There are three channels: shortwave, defined as 0.3–5 μm; total, defined as 0.3–100μm; and window region, defined as 8–12 μm (Smith et al., 2014). As with GERB/SEVIRI, the longwave is obtained by subtracting the shortwave from the total channel. For CERES, the TOA is assumed to be at an altitude of 20km, and the resolution is 20km at nadir (Loeb et al., 2018).

Similar to the GERB/SEVIRI processing steps, the CERES measurements are first unfiltered (Loeb et al., 2001). Next, the Moderate Resolution Imaging Spectrometer (MODIS), a multispectral imager also on Aqua and Terra, provides scene identification (Minnis et al., 2011) allowing for selection of angular distribution

model to obtain the instantaneous flux from CERES unfiltered radiances (Loeb et al., 2003; Loeb and Manalo-Smith, 2005; Su et al., 2015). From this, spatial and temporal averaging leads to the level 3 products. I use a number of these level 3 TOA observational products, namely the single scanner footprint at 1° (SSF1deg) product in Chapter 5 and the synoptic product at 1° (SYN1deg) in Chapter 4. I also use the level 4 Energy Balanced and Filled (EBAF) product in Chapter 4. Figure 2.2 and the following sections outline how these products are obtained and how they relate to one another.

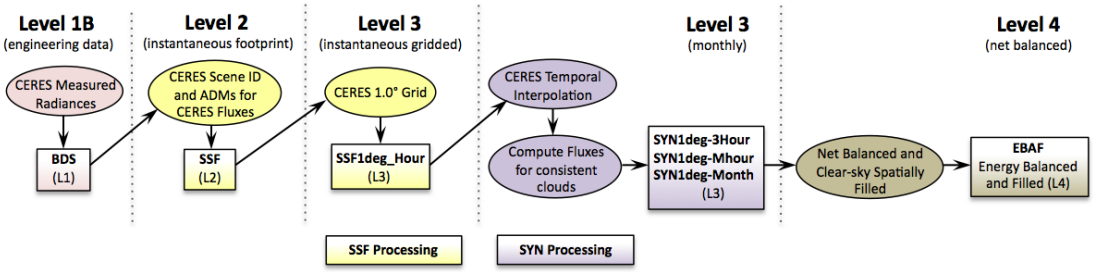

Figure 2.2: Flowchart showing derivation of CERES products and how the products used here are related to one another. Taken from https://ceres.larc.nasa.gov/products.php?product=EBAF-TOA, last accessed February 2020

SSF1deg

The CERES SSF1deg product is available for Aqua and Terra. To obtain the monthly mean on a 1° x 1° grid, the CERES instantaneous fluxes are averaged both spatially and temporally. First, instantaneous fluxes are averaged onto an equal area grid. As the satellites are sun-synchronous and pass overhead each geographical location only twice every 24h, the radiative diurnal cycle for each location must be estimated in order for the temporal averaging to be representative. This interpolation is done in 1 hour increments. For SSF1deg, the CERES-only method is employed for the temporal averaging. This method

assumes scene invariance between satellite overpass times (10:30 local time for Aqua, 13:30 for Terra): for shortwave radiation a diurnal model is fitted to each grid point, dependent on scene and sun-angle (Doelling et al., 2013; Loeb et al., 2018); for longwave radiation a half-sine curve is fitted over land grid points, and linear interpolation used over ocean (Young et al., 1998). These 1 hour time series are used to calculate monthly means and are output to a 1° x 1° grid (Doelling et al., 2013). As the SSF1deg product is single satellite, I use Aqua SSF1deg in conjunction with other data on the Aqua platform, namely AIRS (see section 2.2.3), in Chapter 5.

SYN1deg

While the SSF1deg processing assumes that the scene does not change between measurements, SYN1deg uses observations from five geostationary imagers to explicitly take changes in cloud and radiation into account, known as the CERES-geostationary method (Doelling et al., 2013). These supplementary observations are at 3 hour frequency for SYN1deg edition 2.8, and 1 hour frequency for SYN1deg edition 4. As these are narrowband imagers, steps are taken to convert to broadband and to minimise artefacts from this conversion (see Doelling et al. (2013, 2016) for more detail). As the geostationary imagers are less able to identify clear-sky scenes than MODIS, this method is not used for the clear-sky SYN1deg product instead the CERES-only method is used for clear-sky SYN1deg (Loeb et al., 2018).

EBAF

While the global means of incoming shortwave and outgoing longwave and shortwave radiation at the TOA are approximately 340Wm^{-2}, there exists a small

imbalance, estimated to be 0.51 Wm^{-2} (Loeb et al., 2012; Trenberth et al., 2014; Schuckmann et al., 2016). This imbalance is considerably smaller than current instrument uncertainty range: CERES SYN1deg and SSF1deg products, for example, have a net imbalance of $4.3Wm^{-2}$ (Loeb et al., 2018). This uncertainty poses problems not just for use of CERES data for studies of global mean radiation budget, but also climate model evaluation. To address this, the Energy Balanced and Filled, Edition 4, product, constrains the TOA fluxes to ocean heat content (Loeb et al., 2009). In this way, the EBAF product is 'balanced' to explicitly take ocean heat storage into account. Missing data points in SYN1deg are also 'filled' in EBAF. SYN1deg uses only scenes which are completely cloud free (less than 0.1% cloud cover) for the clear-sky products, leading to many missing data points. These partially clear scenes are estimated in EBAF using MODIS measurements to produce a TOA clear-sky climatology (Loeb et al., 2009) . This results in an energy balanced, complete gridded data product, suitable for comparison with climate model output. I use EBAF in Chapter 4.

2.2.3 The Atmospheric Infrared Sounder and Advanced Microwave Sounding Unit instruments

The Atmospheric Infrared Sounder (AIRS) on Aqua is designed to sound the humidity and temperature of the atmosphere. It has 2378 channels, between 3.7–15.4μm (Aumann et al., 2003). Launched in 2002, it is still in operation, the specific product used in Chapter 5 of this thesis also uses measurements from the Advanced Microwave Sounding Unit (AMSU, also on Aqua), which provides data from 2002–2016. The key scientific aim of AIRS/AMSU is to provide temperature and humidity profiles of the atmosphere of a comparable accuracy to radiosondes for numerical weather prediction (Chahine et al., 2006). I use the following

Level 2, version 6 data: temperature, specific humidity and relative humidity atmospheric profiles, surface skin temperature and TOA OLR.

A key aspect of the AIRS/AMSU data is that it is 'cloud cleared', as opposed to clear-sky. Cloud clearing uses characteristics of adjacent scenes to infer clear-sky values. To do this, there are two key assumptions made: that, for a given cloud type (optical properties and height), the only control on radiation is cloud fraction (i.e. that the radiative properties of a cloud is fixed for cloud type); and that the temperature and humidity profiles are the same in a cloudy and a clear-sky portion of a scene (Susskind et al., 2003).

2.3 Satellite-inferred surface products

While some of the products described above are directly based on measurements made by satellite instruments, the following surface products require more involved calculation with estimates of atmospheric properties from satellite retrievals and reanalysis.

2.3.1 Energy Balanced And Filled surface radiation products and SYN1deg atmospheric properties

One such product which I use is the EBAF Surface product (Kato et al., 2013). EBAF Surface uses a radiative transfer model in conjunction with satellite retrievals of surface and atmospheric properties, constrained by CERES observations of TOA irradiance, to estimate surface irradiance. The inputs to EBAF Surface are from the SYN1deg cloud, surface, water vapour and aerosol properties, with CERES EBAF TOA irradiance used as a constraint (Kato et al.,

2013; Rutan et al., 2015). The non-radiative SYN1deg fields are obtained from different sources. Aerosol optical depth, for example, is derived from MODIS images and a chemistry transport model, the Multi-scale Atmospheric Transport and Chemistry (MATCH) model (Collins et al., 2001). Water vapour and temperature profiles in SYN1deg are model derived, from the Goddard Earth Observing System (GEOS) Data Assimilation System (for more detail, see Kato et al. (2013)). Therefore, EBAF-Surface, EBAF-TOA and the SYN1deg auxiliary variables used in their computation, are all consistent with each other. Using surface observations, EBAF-Surface shortwave product are estimated to have an annual global mean uncertainty of 3 and 4 Wm^{-2} for upwelling and downwelling fluxes, respectively, with the corresponding longwave uncertainties 3 and 6 Wm^{-2} (Kato et al., 2018).

In Chapter 4, I use these data products in conjunction with one another to make inferences about the impact of atmospheric properties on the radiative fields. While providing self-consistent, area-averaged products over a regular grid, appropriate for comparison with GCM output, a limitation of EBAF-Surface products are that they are not direct observations and therefore require careful use and validation with observations.

2.3.2 Climate Monitoring Satellites Application Facility's Surface Solar Radiation Data Set - Heliosat

In Chapter 4, I also use a downwelling shortwave radiation from the Surface Solar Radiation Data Set - Heliosat (SARAH) Ed. 2 (Pfeifroth et al., 2017) from CMSAF. In particular, I use the monthly mean of incoming solar radiation, derived from SEVIRI from 2005–2014 inclusive. SARAH has been extensively validated against European ground stations (see, for example, Pfeifroth et al., 2018).

2.4 Models

2.4.1 Reanalysis (ERA-Interim)

Reanalysis is a type of model output which is often used as pseudo-observational. It is produced by systematically running high-resolution, short-timestep models which assimilate observations every 6-12 hours, over long periods of time. The models used are often similar to forecasting models, therefore reanalysis can be thought of as 'historic' forecasts: what the forecast would have been had there been the most up-to-date models, given contemporary observations. Reanalyses provide homogeneous, long-term, high spatial resolution, vertically resolved data sets. They are often used in place of observations, especially when there are few or no true observations available, or when datasets which are consistent with each other are required. A set of reanalyses extensively used in weather and climate research are from the European Centre for Medium-Range Weather Forecasts (ECMWF). ECMWF's Re-Analysis (ERA) -Interim provides atmospheric, ocean and land surface process output from 1979–present day. ERA-Interim is based on cycle 31r2 of the Integrated Forecasting System (IFS), which has a horizontal resolution of approximately 80km, over 60 vertical levels. It assimilates data every 12 hours, with computed variables output every 3 or 6 hours (Berrisford et al., 2011; Dee et al., 2011). In Chapter 3, I use a newer cycle of ECMWF's IFS, cycle 43r1, testing it against in-situ observations from the ARM Mobile Facility (see section 2.1). In Chapters 4 and 5, I use output from ERA-Interim itself.

2.4.2 General circulation models

General circulation models (GCMs) differ from reanalysis through purpose and design. While reanalysis forecasts the state of the atmosphere at short timesteps

at high resolution, with regular observations assimilated, GCMs aim to recreate the large-scale variability and behaviour of the climate system, and can be either unforced or forced with, for example, observed SSTs. 'Coupled' models include many different systems and their links: generally this refers to ocean and atmospheric models, but some models also contain other aspects, such as terrestrial carbon cycling (Flato et al., 2013). GCMs are used for many aspects of climate research, for example for simulating future climate scenarios.

Given the large number of GCMs developed by modelling groups all over the world, there have been significant efforts to obtain consistent experimental outputs to allow model intercomparisons. In particular, the Coupled Model Intercomparison Project (CMIP, Meehl et al., 2005), has co-ordinated large modelling efforts in conjunction of the IPCC reports. The fifth phase, CMIP5, is made up of a range of experiments, including those of the past climate (both paleo-climate and the recent past), the future climate under various warming scenarios, and of idealised experiments (Taylor et al., 2012). In Chapter 4, I use outputs from both coupled and atmosphere only (AMIP) experiments (Gates, 1992). These AMIP runs are forced using observed SSTs, sea ice and radiative forcings from 1850–2005.

To summarise, in this thesis I use data from a variety of sources which have different advantages, applications and purpose of design with the aim of interpreting radiation flux variability at the TOA and surface. By combining both observations and model output I hope to gain insight into the physical mechanisms driving radiative flux variability and our ability to model these links.

Chapter 3

Characterising energy budget variability at a Sahelian site: a test of NWP model behaviour

Abstract

We use daily observations of surface and top-of-the-atmosphere (TOA) broadband radiation fluxes determined from the Atmospheric Radiation Measurement program Mobile Facility, and GERB/SEVIRI, and a range of meteorological variables, at a site (13°29 N, 2°11 E) in the Sahel during 2006 to test the ability of the ECMWF Integrated Forecasting System cycle 43r1 to describe energy budget variability. The model has daily average bias of -12Wm^{-2} and 18Wm^{-2} for outgoing longwave and reflected shortwave TOA radiation fluxes, respectively. At the surface the daily average bias is 12(13)Wm^{-2} for the downwelling (upwelling) longwave radiation flux, and -21(-13)Wm^{-2} for the shortwave downwelling (upwelling) radiation flux. Using multivariate linear models of observation minus

model differences, we attribute radiation flux discrepancies to physical processes, and link surface and TOA fluxes. We find that model biases in surface radiation fluxes are mainly due to a low bias in ice-water path (IWP), poor description of surface albedo, and model-observation differences in surface temperature. We also attribute observed discrepancies in the radiation fluxes, particularly during the dry season, to the misrepresentation of aerosol fields in the model from use of a climatology instead of a dynamic approach. At the TOA, the low IWP impacts the amount of reflected shortwave radiation while biases in outgoing longwave radiation are additionally coupled to discrepancies in the surface upwelling longwave flux and atmospheric humidity.

Author contributions: This chapter has been published in *Atmospheric Chemistry and Physics* in 2017 (DOI: acp-17-15095-2017). I performed the analysis and wrote the article with contributions and editing from Paul Palmer and Helen Brindley. Robin Hogan provided the ECMWF model output and R.L. Miller provided helpful advice on the appropriate use of multivariate linear models. There were additional amendments made at the suggestion of two anonymous reviewers and the editor.

3.1 Introduction

The balance at the top-of-the-atmosphere (TOA) between solar and thermal radiation fluxes determines the energy budget of the climate system. As described in more detail in Chapter 1, modelling the TOA radiation budget remains challenging due to the complexity of interactions between solar and thermal radiation with atmospheric and surface processes. Here, we use surface and TOA radiation flux measurements to test model skill of the Integrated Forecasting System (IFS) Cycle 43r1 from the European Centre for Medium-Range Weather Forecasts (ECMWF), a subsequent cycle to Cycle 31r2 on which the reanalysis ERA-Interim is based.

To test 43r1, we use a combination of TOA broadband radiation fluxes determined from the Geostationary Earth Radiation Budget (GERB) and Spinning Enhanced Visible and Infrared Imager (SEVIRI) instruments (Schmetz et al., 2002; Harries et al., 2005), and surface radiation and meteorological measurements taken by the Atmospheric Radiation Measurement (ARM) Mobile Facility (AMF) deployment in Niamey, Niger during 2006 (Miller and Slingo, 2007). Data collected during this campaign consists of not only high frequency surface radiation measurements, but also coincident measurements of atmospheric variables relevant to the study of radiation transfer, including aerosol optical depth, atmospheric humidity, 2 m air temperature and data from sonde ascents. Using the model helps us to link observed radiation flux variations at the surface to TOA radiation fluxes, and to quantify the influence of radiative and non-radiative variables on model error.

The combination of data available from the AMF and GERB/SEVIRI provide a valuable insight into radiative processes in a region where surface measurements are scarce. In particular, the high temporal frequency of the data allows us to look in detail at the relationships and dependencies between key variables. It is worth noting that although this study is necessarily limited to the one measurement

site at Niamey, this location was chosen carefully in order to sample the range of climatic conditions typically experienced across the wider Sahelian region (Miller and Slingo, 2007).

In the next section, we describe the study site at Niamey, Niger and the associated key components of radiative transfer. We present the data and methods in section 3.2. In section 3.3 we present our analysis of individual components of the radiation flux, including an analysis of the model error. We provide conclusions in section 3.4.

Niamey, Niger (13°29 N, 2°11 E) was selected for the first AMF deployment because the characteristic climatology of the location exhibits strong variability that substantially affects the corresponding behaviour of the TOA and surface radiative fluxes. Regional dust storms and biomass burning plumes significantly impact the energy budget (Slingo et al., 2006; McFarlane et al., 2007), with dry season aerosol loading composed of varying proportions of mineral dust and biomass burning aerosol from agricultural fires (Johnson et al., 2008). Additionally, the annual progression of the Intertropical Front (ITF) drives the West African monsoon (WAM) and imposes a strong seasonal cycle on radiation fluxes due to the onset of the wet season from approximately April–October (Slingo et al., 2008).

The AMF deployment over Niamey, described in more detail in Chapter 2, was from late 2005 to early 2007. It included measurements of a range of meteorological, thermodynamic, and radiative variables. The deployment was designed to coincide with the availability of TOA broadband radiation fluxes from GERB. Data from AMF and GERB could then be reconciled to identify problems in radiative transfer schemes and numerical weather prediction, (Miller and Slingo, 2007).

3.1.1 Overview of Radiation and Meteorological Environment

Figure 3.1 is used to present the key features of radiative transfer of the Earth-Atmosphere system, with the following section outlining key aspects of this in Niamey. We refer the reader elsewhere for further, in depth detail (e.g., Slingo et al., 2008, 2009).

The incident solar radiation (TSI) enters the top of the atmosphere. A fraction of the TSI is transmitted through the atmosphere, reaching the surface as 'direct' solar radiation (1d). When water vapour (1a), cloud (1b) or aerosol (1c) is present, a significant fraction of the incident solar beam will be absorbed or scattered. Some of the scattered radiation will be scattered down to the surface as 'diffuse' solar radiation (2a, 2b, 2c). The combination of the diffuse and direct downward radiation combine to form the total downwelling solar, or shortwave, radiation at the surface (DSR, 2). A fraction of this downwelling solar radiation will be reflected, determined by the surface albedo, as upwelling shortwave radiation (USR, 3). The fraction of the USR that is transmitted up through the atmosphere, combined with the solar radiation scattered upwards by atmospheric molecules, clouds and aerosol and escaping to space (4a, 4b), represents the reflected solar radiation at the TOA (RSR, 4).

Longwave radiation fluxes also depend on the meteorological conditions. Resulting thermal emissions from the surface (upwelling longwave radiation/ULR, 5) can be absorbed or scattered by atmospheric molecules (predominantly water vapour (5a), but also other well-mixed greenhouse gases and ozone), clouds (5b) and dust aerosol (5c) depending on the season. Subsequent emission of radiation from these absorbers contributes to the downwelling longwave radiation at the surface (DLR, 6a, 6b, 6c) and outgoing longwave radiation (OLR, 7a, 7b, 7c) at

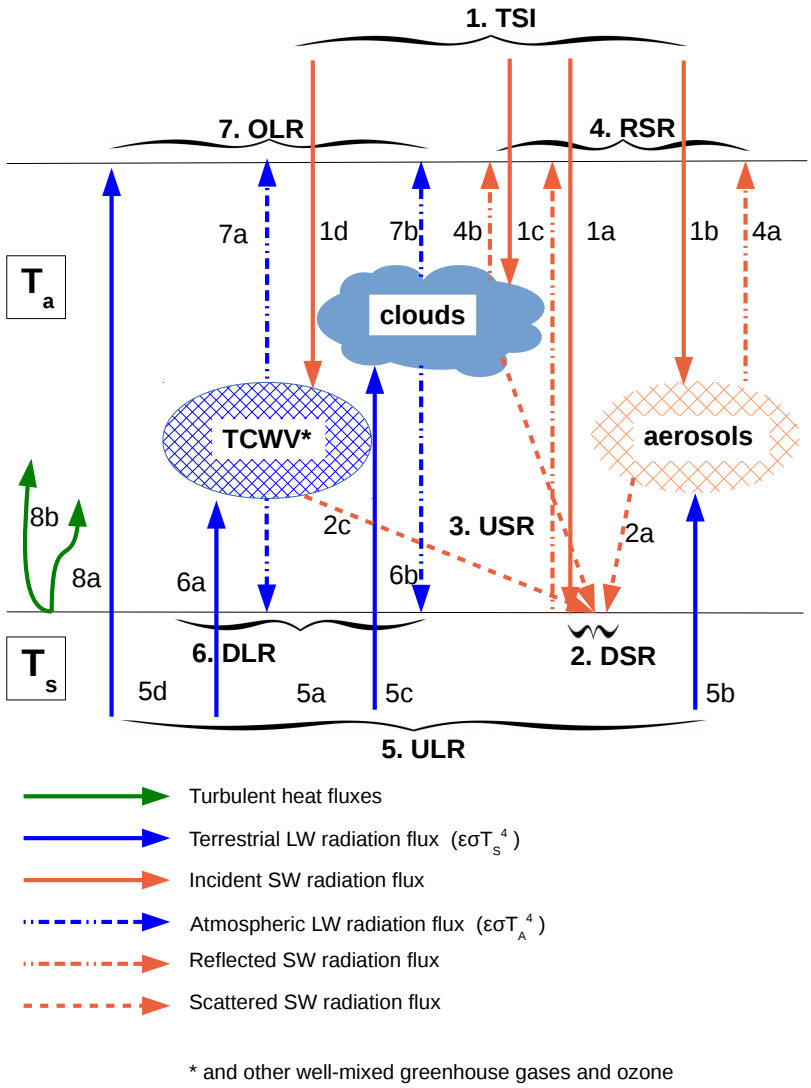

Figure 3.1: Simplified schematic of major processes controlling broadband radiation fluxes. Red arrows indicate shortwave radiation fluxes, blue arrows longwave radiation fluxes. For detailed description of arrows, please see text in section 3.1.1

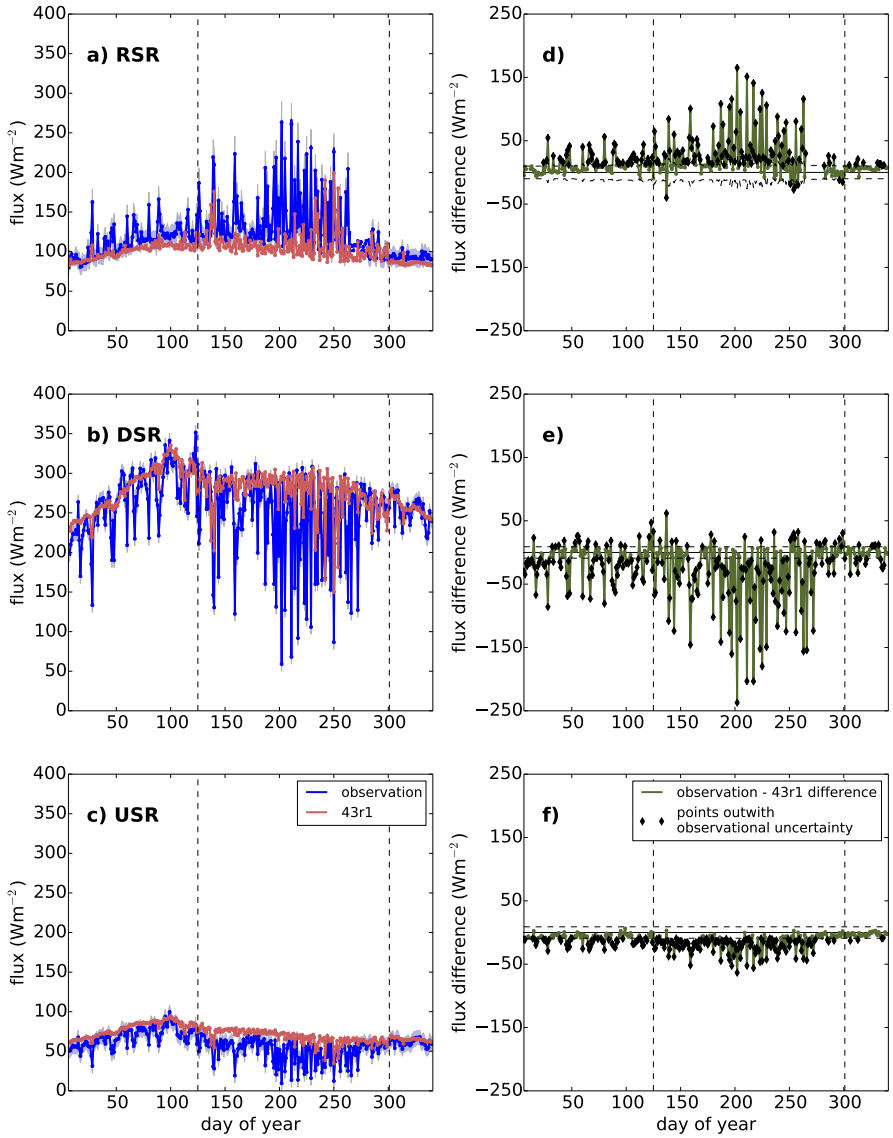

Figure 3.2: Daily means of observed (blue, from AMF and GERB) and 43r1 (red) shortwave radiation fluxes at Niamey during 2006. Lines become dashed when values are from interpolation (see Sec. 3.2). Plots show observed and 43r1 (a) TOA reflected shortwave; (b) surface downwelling shortwave; (c) surface upwelling shortwave radiation fluxes; and the observation - 43r1 difference of these same fluxes in (d)-(f) respectively. Black diamonds on plots (d)-(f) indicate model values outside of the observational uncertainty range (horizontal dashed lines). Vertical dashed lines indicate the beginning and end of the wet season.

the TOA. The OLR also includes the fraction of radiation emitted by the surface that is transmitted through the atmosphere and escapes directly to space (5d). The surface also cools by sensible heat flux (SHF, 8a), or, depending on soil moisture content, latent heat flux (LHF, 8b).

There is a distinct dry and wet seasons in Niamey, determined by the position of the surface ITF, the boundary between the moist air coming from the southwest from the tropical Atlantic, and the warmer, dry air coming from the northeast from the Sahara (Hasternath and Lamb, 1977; Lélé and Lamb, 2010). During 2006 the 'first' dry season ran from day 1–125, the wet season from day 126–300 and the 'second' dry season from day 301–365, as determined by a sustained dew point temperature of at least 15°C (Slingo et al., 2009). Wet and dry seasons alternate, with the dry season running from approximately October–April, though we here use 'first' and 'second' to differentiate between the dry season which occurs within 2006 but before the wet season, and that which occurs after.

Figure 3.2b shows that during the first dry season, given clear conditions, there is a steady increase in surface DSR as the year progresses. Dry conditions typically lead to a relatively constant surface albedo such that USR, and to an extent RSR (Fig. 3.2c and a) also increase with time. Figure 3.3 implies that the increasing DSR results in surface warming which in turn leads to enhanced ULR. The presence of clouds, water vapour and aerosols lead to deviations from this trend. Aerosols from dust storms, blown in from the Sahara, decrease DSR (McFarlane et al., 2009), enhance DLR (Miller et al., 2009) and increase RSR. Periodic increases in cloudiness and total column water vapour (TCWV) lead to increased absorption of both long- and shortwave radiation. This results in decreases in DSR, increases in RSR and increases in DLR due to atmospheric warming.

After the northwards passing of the ITF over Niamey in April, Niamey enters

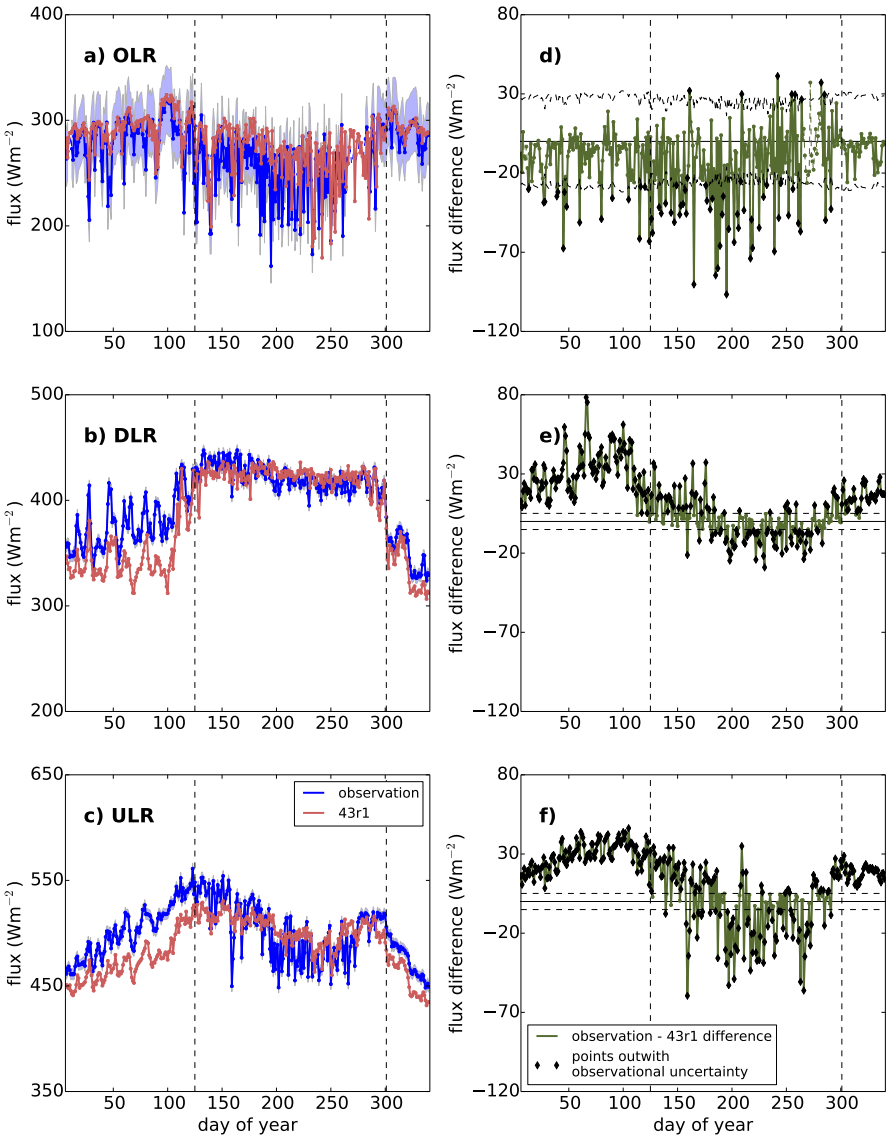

Figure 3.3: As Figure 3.2 but for longwave fluxes. Plots show observed and 43r1 (a) TOA outgoing longwave; (b) surface downwelling longwave; (c) surface upwelling longwave radiation fluxes; and the observation - 43r1 difference of these same fluxes in (d)-(f) respectively.

the wet season. The further northward the ITF migrates, the greater the vertical extent of the moist air mass above Niamey. TCWV therefore peaks when the ITF is at its most northerly, leading to a period with deep convective clouds and increased precipitation (Lélé and Lamb, 2010). Greater cloud cover leads to enhanced SW reflection back to space and atmospheric SW radiative heating which reduce the DSR (Figure 3.2a and b). Clouds and increased TCWV also absorb in the LW, reducing OLR and enhancing DLR (Fig. 3.3). Decreases in DSR reduces the shortwave radiative heating of the surface, therefore decreasing ULR. Increases in precipitation, and therefore higher soil moisture, affects the partition between radiative, sensible and latent heating.

3.1.2 Overview of Previous Studies

There are a number of studies that have evaluated radiative processes in West Africa as represented by various models, which point to the difficulties in simulating the processes which control radiative transfer in the Sahel. Miller et al. (2012) examine the impact of hydrological variables on broadband atmospheric column divergence in Niamey using both the data from the AMF/GERB and output from four Global Climate Models (GCMs). They show that the reasonably well modelled net broadband divergence across the atmosphere is the product of error cancellation of longwave and shortwave divergences. GCMs such as these are not intended to exactly replicate the exact state of the atmosphere but rather capture long-term spatial and temporal patterns. Operational forecasts and reanalyses, however, assimilate observational data regularly and aim to simulate the atmosphere as closely as possible. As Walsh et al. (2009) discuss, high temporal frequency observations at specific points are ideal for comparison to reanalyses: not only do observational constraints make the projections as realistic as possible, but reanalyses often share aspects with GCMs which means evaluating

them can simultaneously improve our understanding of underlying models used to make climate predictions.

There has also been some comparison of operational forecasts to data from the AMF and GERB at Niamey during 2006. Agustí-Panareda et al. (2010), in their wider comparison of West African data to ECMWF's operational forecast, briefly look at how well surface broadband fluxes are modelled in Niamey. They note that there are periods in the dry season where the observed DSR decreases which are not present in the model and attribute this primarily to the use of a constant climatology for aerosol loading and missing cloudy conditions. ERA-I has also been evaluated by other studies in West Africa (Marsham et al., 2016), who find that TCWV is well captured by the model and that its role in controlling TOA net flux is more important than that of dust.

3.2 Data and Methods

3.2.1 Data and Their Uncertainties

We use GERB-like High Resolution TOA broadband radiation fluxes, hereinafter referred to as GERB fluxes, with a temporal resolution of 15 minutes and a spatial resolution of 10 km at nadir (Dewitte et al., 2008). This product uses SEVIRI measurements, passed through the GERB processing algorithms, to derive broadband fluxes throughout the year.

Table 3.1 summarizes the surface radiative and non-radiative variables that we use from the AMF during 2006. Direct, diffuse and total shortwave fluxes were measured using a normal incidence pyroheliometer, and shaded and unshaded

Table 3.1: Radiative and non-radiative data used from the AMF, with dates for which the data stream is available for in 2006. Uncertainties are given as an average for the time average indicated. Data are available from the ARM archive: http://www.archive.arm.gov.

Variable	**Datastream**	**Description**	**Freq.**	**Period**	**Uncertainty**
Shortwave radiation flux (Wm^{-2})	qcrad1-longM1.s2	Up and downwelling, at surface	1 min avg	01-01 – 12-31	9 Wm^{-2}
Longwave radiation flux (Wm^{-2})	qcrad1-longM1.s2	Up and downwelling, at surface	1 min avg	01-01 – 12-31	5 Wm^{-2}
Temperature (°C)	nimmet-M1.b1	Temperature, air, at 2m height	1 min avg	01-01 – 12-08	1%
TCWV (cm)	nimsonde-wnpnM1.b1	Temperature, at altitude ; dew point, Pressure, atmospheric, at altitude	6 hour	01-06 – 12-31	0.5 °C 1hPa
Turbulent Fluxes (Wm^{-2})	nim30qc-ecorM1.s1	Latent, sensible	30 min avg	01-01 – 12-31	6%

pyranometers respectively, while longwave fluxes were measured using shaded and unshaded pyrgeometers. These were complemented with inferences of turbulent heat fluxes (THF) from an eddy correlation system. From the ARM-standard meteorological instruments we use 2 m air temperature. The temperature and pressure measurements at altitude, required for TCWV estimates, come from Vaisala RS-92 radiosonde ascents. We also use relative humidity (RH) profiles from the sonde ascents to extract upper tropospheric humidity (UTH), defined, following Brindley (2007), as the average RH between 500-200hPa. Finally, we use aerosol optical depth (AOD) at 500nm from the multiple-frequency rotating shadow band radiometer (MFRSR), corrected for forward scattering (Harrison et al., 1994; Michalsky et al., 2001). In addition to these surface based measurements, we use ice water path (IWP) and liquid water path (LWP) daily averages derived from SEVIRI provided by the Climate Monitoring Satellite Application Facility (CMSAF).

When comparing AMF and GERB data we consider two sources of error associated with: 1) the determination of the quantities being measured by an instrument, and 2) relating an intrinsically point AMF measurement with a GERB flux measurement that is representative over a much larger spatial scale (Settle et al., 2008). Slingo et al. (2009) estimate uncertainties in GERB fluxes to be approximately 5 Wm^{-2} and 10 Wm^{-2} for the short- and longwave respectively. However, Ansell et al. (2014) argue that this underestimates the uncertainty, and estimate the instantaneous flux uncertainty to be 10% for both long- and shortwave fluxes. In this study we use whichever of these is larger on a particular day, along with the AMF uncertainties of 5 Wm^{-2} and 9 Wm^{-2} for surface long and shortwave fluxes following Slingo et al. (2009). Uncertainties in other AMF variables are given in Table 3.1, while those in IWP and LWP are provided by CMSAF and have an annual mean of 0.021 and 0.015 kgm^{-2}, respectively.

For ease of comparison, all data are processed into daily means. Figs. 3.2, 3.3,

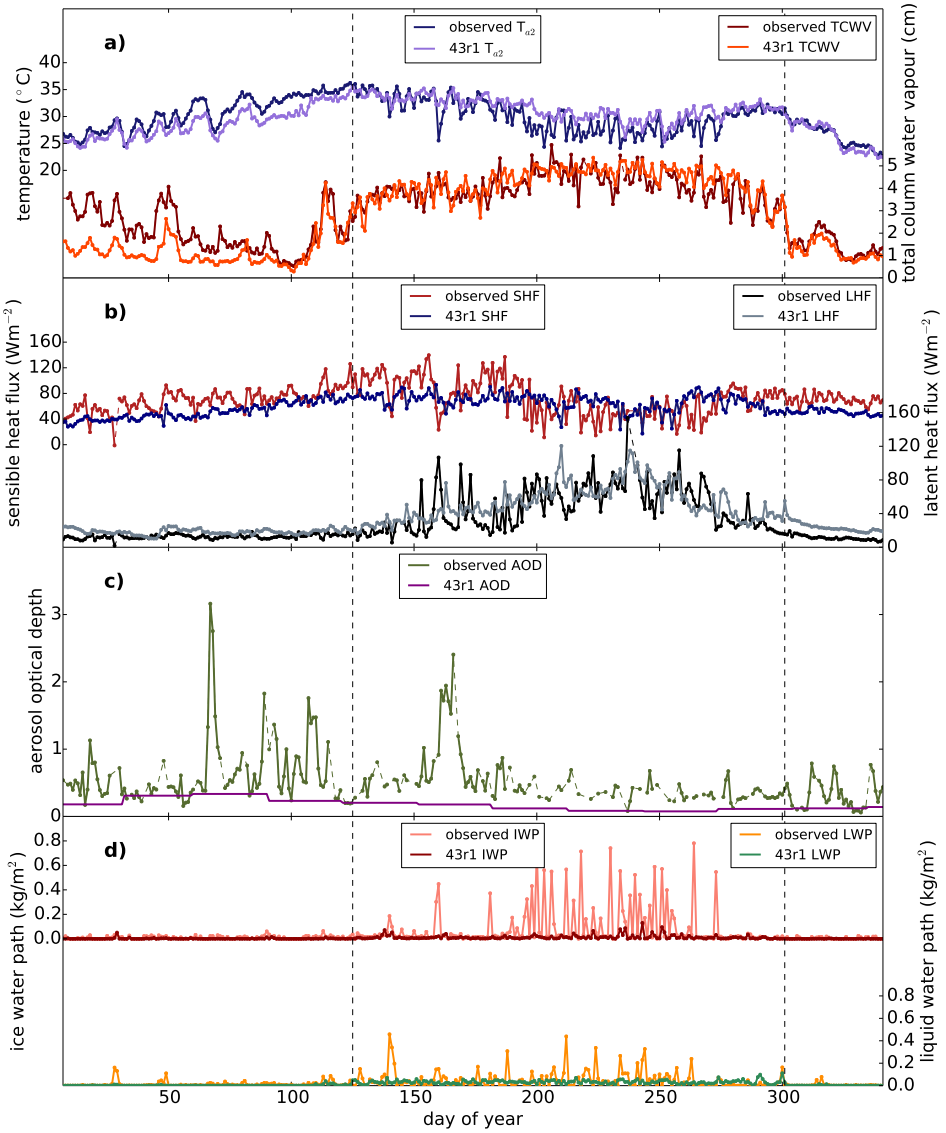

Figure 3.4: Observed and 43r1 non-radiative fluxes for Niamey during 2006. Plot (a) shows temperature and TCWV; plot (b) sensible and latent heat fluxes; plot (c) aerosol optical depth; and plot (d) ice water path and liquid water path. Dashed sections indicate imputed data, and dashed vertical lines indicate the beginning and end of the wet season.

and 3.4 show daily means of shortwave and longwave fluxes, and non-radiative variables, respectively. For our analysis, as described below, we use continuous data sets that are regularly spaced in time. We use the period 7th January – 8th December, determined by the availability of sonde and air temperature data, and impute missing values. Missing values from the AMF data are imputed using a linear interpolation. We also use a linear interpolation for missing GERB data points for gaps of one data point long, otherwise we use a climatology from 2005-2014. In the majority of cases this corresponds to a 9-year mean.

3.2.2 Model and Data Analysis

We compare the daily means of the radiation and meteorological variables to corresponding model output from IFS Cycle 43r1 (Fig. 3.4). We use the Tco399 resolution of IFS Cycle 43r1, with a global horizontal resolution of approximately 29 km and 137 vertical levels. The radiation scheme is called every hour, with approximate updates every model timestep (15 minutes) using the approach of Hogan and Bozzo (2015). Both Cycle 43r1 and ERA-I use a climatological aerosol distribution (Dee et al., 2011), derived from Tegen et al. (1997).

To evaluate the daily mean model radiative and non-radiative variables, we use the square of Pearson's correlation coefficient r^2, which we assume is statistically significant only if the p-value <0.001, and the root mean square error (RMSE). We also use the average daily model bias, which we define as

$$\text{bias} = \frac{\sum_i^n (x_i^O - x_i^M)}{n}, \tag{3.1}$$

where x_i is the variable in question on day i, n denotes the number of days, and the superscripts O and M denote observation and model, respectively.

We use multivariate models to link observed and model variables. To build the multivariate linear models for a particular variable, we identify potential predictor variables based on the schematic in Fig. 3.1 to give a physical rationale for selection. There are two requirements for the predictor variable to be included in the linear model to avoid overfitting: first, the predictor variables must have a statistically significant correlation with the dependent variable which also tests whether the linear approximation is appropriate; second, the predictor variables must be independent of each other. To achieve this, we first perform a least-squares regression of the predictor variable on the dependent variable, and then between the selected predictor variables to ensure mutual independence.

We select predictor variables according to the criteria above in order to build linear models of the observed and 43r1 fluxes. This has two purposes: not only does this highlight the relative importance of different predictor variables in both the observations and 43r1, but it also indicates generally how well a linear multivariate model is able to capture the variability. Finally, we build models of the differences between observed and 43r1 variables: we define the observed-43r1 value to be the 'discrepancy'. The uncertainties in the linear models are derived from the measurement uncertainties, propagated with the uncertainty from the linear model. We evaluate model performance by assessing the variation in the discrepancy which is explained by the linear model using the r^2-value.

3.3 Results

3.3.1 Model Radiative and Non-radiative Variables

We begin with a comparison of observations to both 43r1 and ERA-I radiation fluxes at the surface and the TOA for long- and shortwave flux observations

(Appendix A). ERA-I has a coarser spatial resolution, with a horizontal grid of approximately 80km, and 60 vertical levels Berrisford et al. (2011). ERA-I is also based on an IFS Cycle 31r2, which was operational a decade earlier than 43r1. Numerous improvements to the physics and the dynamics of the model have been made in the intervening period, such as changes to the convection scheme leading to a much better capturing of the diurnal cycle of tropical convection (Bechtold et al., 2014). From Appendix A we see that although there are some distinct changes between the two cycles of the model, most notably in ULR and to a lesser extent DLR, the behaviour of the two versions of the model tends to be more similar to each other than to the matched observations. Due to this similarity, we continue with comparisons of observations to 43r1 only, but note that our general conclusions are applicable to ERA-I output. We explore reasons for the observation-model discrepancies in section 3.3.2.

Radiative Variables

For the shortwave fluxes, the model has a negative bias for RSR (Fig. 3.2a,d) and a positive model bias at the surface , with annual average biases of -21 Wm^{-2} in DSR (Fig. 3.2b,e), and -13 Wm^{-2} in USR (Fig. 3.2c,f). For all shortwave fluxes, the observations show large, day-to-day variations during the second part of the wet season (approximately days 200–300) which are not reproduced by the model.

For OLR, the model has a positive bias throughout the year (Fig. 3.3a,d). However, the majority of the model points lie within the uncertainty bounds of the observations. In the wet season, when large day-to-day variability is seen in the observations but not in the model, differences can exceed the observational uncertainty. Here the average daily bias is -13Wm^{-2} (Table 3.2). In contrast, at the surface there are larger biases in dry season longwave fluxes than in the wet season, with modelled DLR and ULR consistently underestimated (Fig.

Table 3.2: Statistics from observation-43r1 comparison of radiative variables for the whole year (days 7–341), 1st dry season (days 7–125), wet season (days 126–301) and 2nd dry season (days 302–341): Pearson's r^2 value (bold if significant to p $\leq$ 0.001), the root-mean-square-error, and the bias, all defined in Section 3.2.

Variable	**Statistic**	**Whole year**	**First dry season**	**Wet season**	**Second dry season**
OLR	$\mathbf{r^2}$	**0.51**	**0.54**	**0.40**	**0.56**
	RMSE ($\mathbf{Wm^{-2}}$)	24	20	29	10
	bias ($\mathbf{Wm^{-2}}$)	-12	-12	-13	-5
DLR	$\mathbf{r^2}$	**0.83**	**0.76**	**0.68**	**0.90**
	RMSE ($\mathbf{Wm^{-2}}$)	23	33	12	18
	bias ($\mathbf{Wm^{-2}}$)	13	29	0	16
ULR	$\mathbf{r^2}$	**0.45**	**0.89**	**0.35**	**0.94**
	RMSE ($\mathbf{Wm^{-2}}$)	24	30	20	18
	bias ($\mathbf{Wm^{-2}}$)	12	28	-1	17
RSR	$\mathbf{r^2}$	**0.31**	**0.51**	**0.21**	0.01
	RMSE ($\mathbf{Wm^{-2}}$)	32	19	42	10
	bias ($\mathbf{Wm^{-2}}$)	18	13	24	8
DSR	$\mathbf{r^2}$	**0.23**	**0.60**	0.09	0.27
	RMSE ($\mathbf{Wm^{-2}}$)	47	28	60	13
	bias ($\mathbf{Wm^{-2}}$)	-21	-13	-30	-3
USR	$\mathbf{r^2}$	**0.43**	**0.64**	**0.14**	0.33
	RMSE ($\mathbf{Wm^{-2}}$)	17	12	21	5
	bias ($\mathbf{Wm^{-2}}$)	-13	-10	-16	-3

3.3b,c,e,f). The correlation coefficients for both the dry seasons are high (r^2 = 0.89 and 0.76 for ULR and DLR in the first dry season) suggesting that although the model has a significant negative bias, it captures the dry season variability of the surface longwave fluxes well. Wet season average bias in DLR and ULR is small at 0 and 1 Wm^{-2}, respectively, though this is due to cancellation of the model underestimation of DLR and ULR in the first part of the wet season (days 126–200) with the overestimation in the second part of the wet season (days 200–300). All radiative variables show more variability in the observations than the model, reflecting the larger range of competing influences in comparison to the idealised and less chaotic model.

Non-radiative Variables

Figure 3.4 presents observed and modelled 2 m air temperature, TCWV, LHF, SHF, aerosol optical depth (AOD) and IWP and LWP, with mean statistics shown in Table 3.3. Air temperature at 2 m, T_{a2}, is lower than, but closely coupled to, surface or skin temperature (Slingo et al., 2009) for which observations are not available at the study site. We find that observed and model T_{a2} (Fig. 3.4a) follows a very similar pattern to ULR (Fig. 3.3b), as expected. In particular, we find the model generally underestimates observations during the dry season, but with a high correlation coefficient (r^2 = 0.89). During the wet season, as with ULR, the model values of T_{a2} display less of the observed day-to-day variability. The seasonal cycle in TCWV is similar to that in 43r1 (r^2 = 0.80 for the whole year) but is much less variable than the observations during the wet season.

Figure 3.4b shows modelled and observed THF. The model describes 66% of observed LHF variation over the year, with 43% of observed variation described in the wet season but only 10% of observed variation described in the dry season. In contrast, the model captures only 13% of the annual variation of SHF with the

Table 3.3: Statistics from observation-ERA-I comparison of non-radiative variables for the whole year (days 7–341), 1st dry season (days 7–125), wet season (days 126–301) and 2nd dry season (days 302–341): Pearson's r^2 value (bold if significant to p≤0.001), the root-mean-square-error, and the bias, all defined in Section 3.2.

Variable	**Statistic**	**Whole year**	**First dry season**	**Wet season**	**Second dry season**
Temperature	$\mathbf{r^2}$	**0.60**	**0.89**	**0.56**	**0.92**
	RMSE (°C)	2.1	2.1	2.2	0.9
	bias (°C)	0.0	1.8	-1.3	0.3
TCWV	$\mathbf{r^2}$	**0.80**	**0.52**	**0.74**	**0.94**
	RMSE (cm)	0.8	1.0	0.5	0.3
	bias(cm)	0.2	0.8	-0.2	0.3
Latent heat	$\mathbf{r^2}$	**0.66**	**0.10**	**0.43**	0.36
flux	**RMSE ($\mathbf{Wm^{-2}}$)**	17	7	22	11
	bias ($\mathbf{Wm^{-2}}$)	-6	-6	-6	-11
Sensible heat	$\mathbf{r^2}$	**0.13**	**0.52**	0.06	0.13
flux	**RMSE ($\mathbf{Wm^{-2}}$)**	25	23	28	22
	bias ($\mathbf{Wm^{-2}}$)	11	18	5	20
Ice water	$\mathbf{r^2}$	**0.13**	**0.39**	0.07	0.00
path	**RMSE ($\mathbf{kgm^{-2}}$)**	0.13	0.02	0.18	0.01
	bias ($\mathbf{kgm^{-2}}$)	0.05	0.01	0.08	0.01
Liquid water	$\mathbf{r^2}$	**0.08**	**0.12**	0.01	0.08
path	**RMSE ($\mathbf{kgm^{-2}}$)**	0.06	0.03	0.08	0.02
	bias ($\mathbf{kgm^{-2}}$)	0.01	0.01	0.02	0.01

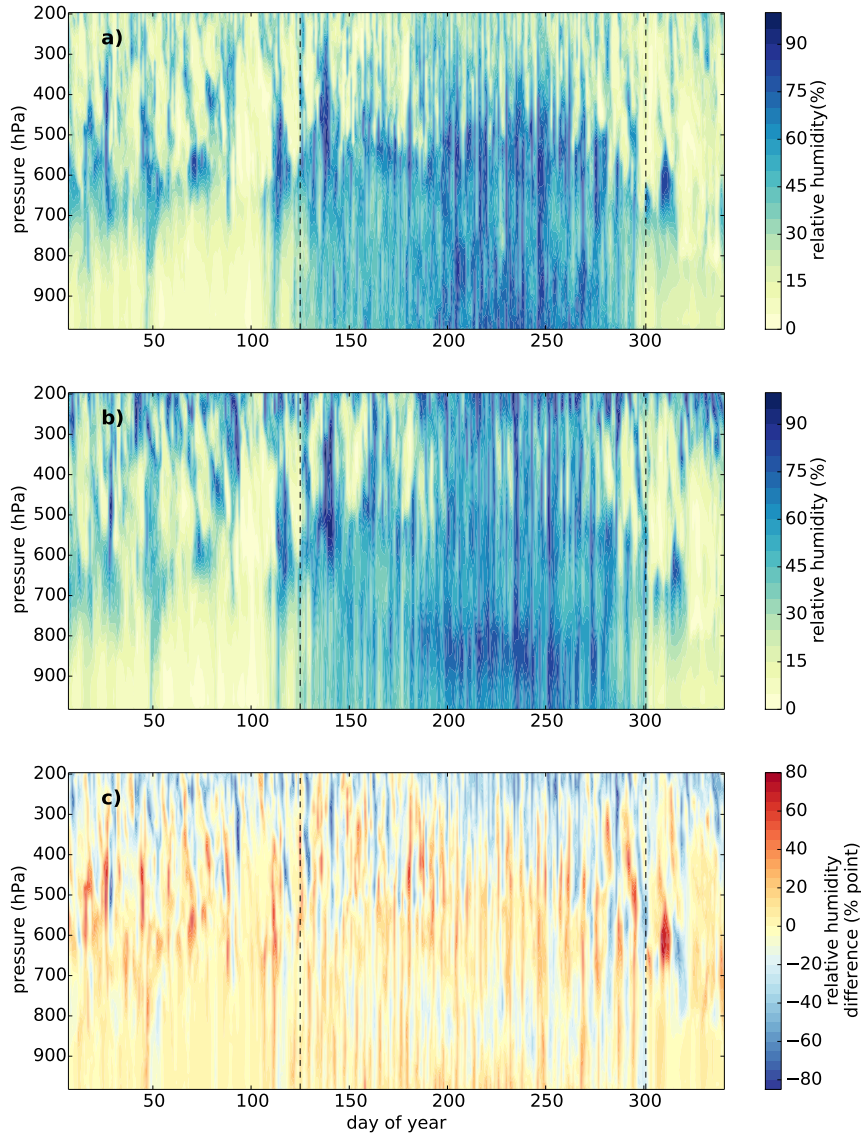

Figure 3.5: (a) observed and (b) 43r1 daily mean of relative humidity profiles from 1000-200hPa above Niamey during 2006. Plot (c) is observation - model relative humidity discrepancy .

52% of the observed variation in the first dry season but only 6% of the observed variation described during the wet season.

For 500 nm AOD from the AMF (Fig. 3.4c), we find large values (>3) during the dry seasons and much less variability in the wet season. The model uses an aerosol climatology (Dee et al., 2011), which bears little resemblance to the observations, and consistently underestimates the AOD throughout the year.

The correlations between the model and observations for IWP and LWP, though significant at the $p \leq 0.001$ level, capture only 13% and 8% of the observed variability, respectively (Fig. 3.4d). The model IWP and LWP have a consistent low bias with respect to the observations (Fig. 3.4), particularly during the wet season. Although there are significant correlations during the dry season ($r^2 = 0.39$ and 0.08, respectively) there are no significant correlations during the wet season when there are large variations in the observations.

Figure 3.5 shows that the model reproduces the observed large-scale seasonal pattern of relative humidity (RH) of a very dry lower troposphere (700-1000hPa) during the dry season, with large variations and high RH throughout the troposphere during the wet season. The model has some consistent differences to the observations with a generally negative bias between 500–700 hPa and a positive bias between 200–400 hPa (Fig. 3.5c).

3.3.2 Surface: radiative flux discrepancies

Differences in up- and downwelling fluxes lead to differences in the surface energy budget (Fig. 3.6a), defined as the difference between the downwelling energy flux (net downward shortwave (DSR-USR) + DLR) and upwelling energy flux (ULR + SHF +LHF), using the convention that downwelling fluxes are positive. We

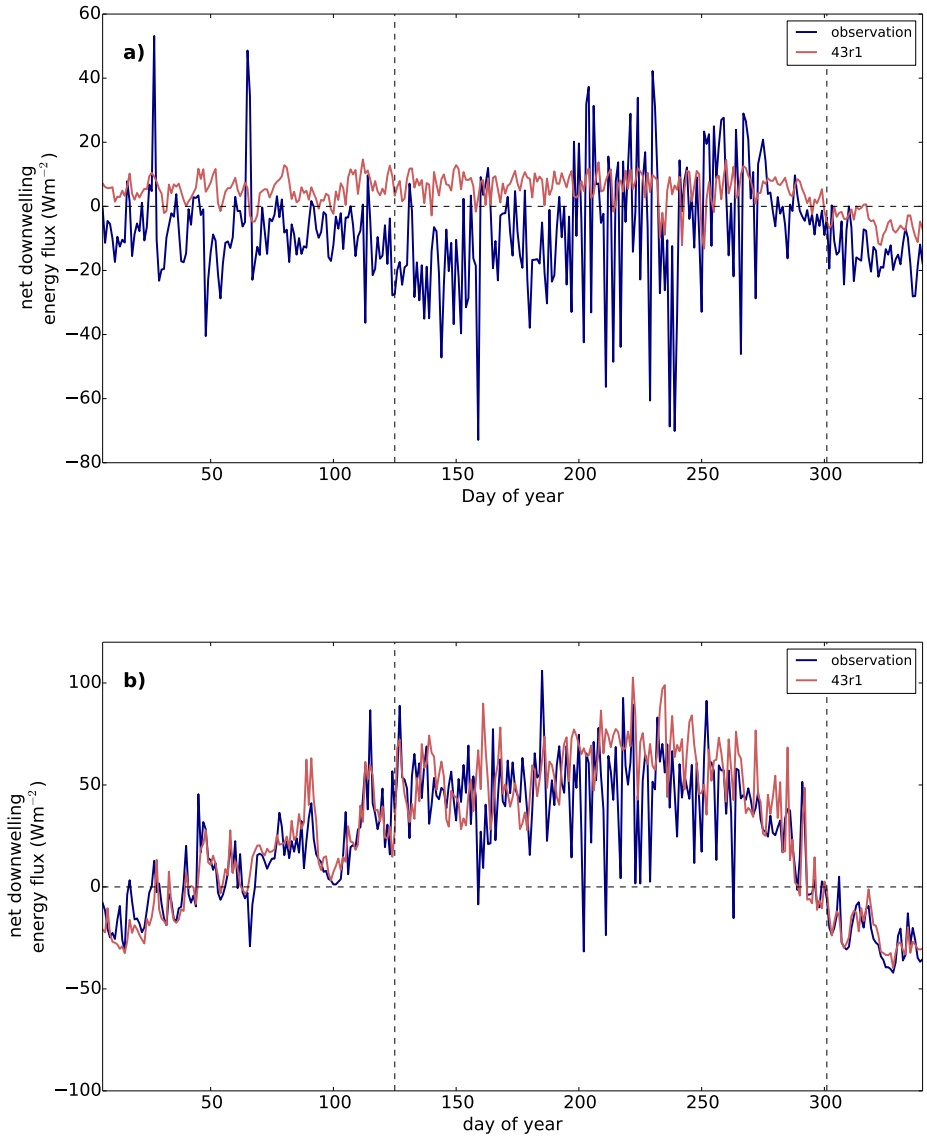

Figure 3.6: Surface and TOA energy budget at Niamey during 2006. Plot (a) shows the net energy flux at the surface (downwelling long-and shortwave surface radiation fluxes minus upwelling long- and shortwave radiation surface fluxes and turbulent heat fluxes) for observations (blue) and 43r1 (red). Plot (b) is the net flux at the TOA (total solar irradiance minus reflected shortwave and outgoing longwave radiation), also for observations and 43r1. Positive values for both indicate more downwelling than upwelling energy flux. Dashed vertical lines indicate beginning and end of the wet season.

find that there is a generally positive downwelling flux in the model, in contrast to the observed negative downwelling flux, arising from the overestimation in net downwelling shortwave radiation.

In the rest of this section we take each of the surface fluxes in turn, and examine the relationship between observed and model fluxes with respect to other variables, before using a multivariate model to interpret the observation-model discrepancy. Equations for all discrepancy linear models can be found in Appendix B. Similar to the discussion in section 3.2 on relating point measurements with area-averages from satellite products, difficulties arise from comparison between point measurements and area-averaged model output. Again, this is somewhat mitigated by the selection of a surface site which is representative of the wider region (Miller and Slingo, 2007), the use of daily means and conservative uncertainty estimates.

Surface downwelling shortwave radiation

We remove the effect of the changing TOA total solar irradiance (TSI) over the course of the year to emphasize the effect of the meteorological controls, though simply refer to this (DSR minus TSI) as DSR for the purposes of this section. We expect that the primary controls on the DSR reaching the surface will be scattering and absorption from aerosols, water vapour and clouds (Fig. 3.1). Therefore, we examine the DSR in both the observations and from 43r1 with relevant variables: AOD, LWP, IWP and TCWV. Table 3.4 presents statistics corresponding to surface shortwave fluxes.

As expected, the observational wet season variability in DSR is more closely correlated to variables related to clouds (TCWV, IWP and LWP), while AOD is more closely correlated to dry season variability. By combining IWP, TCWV and

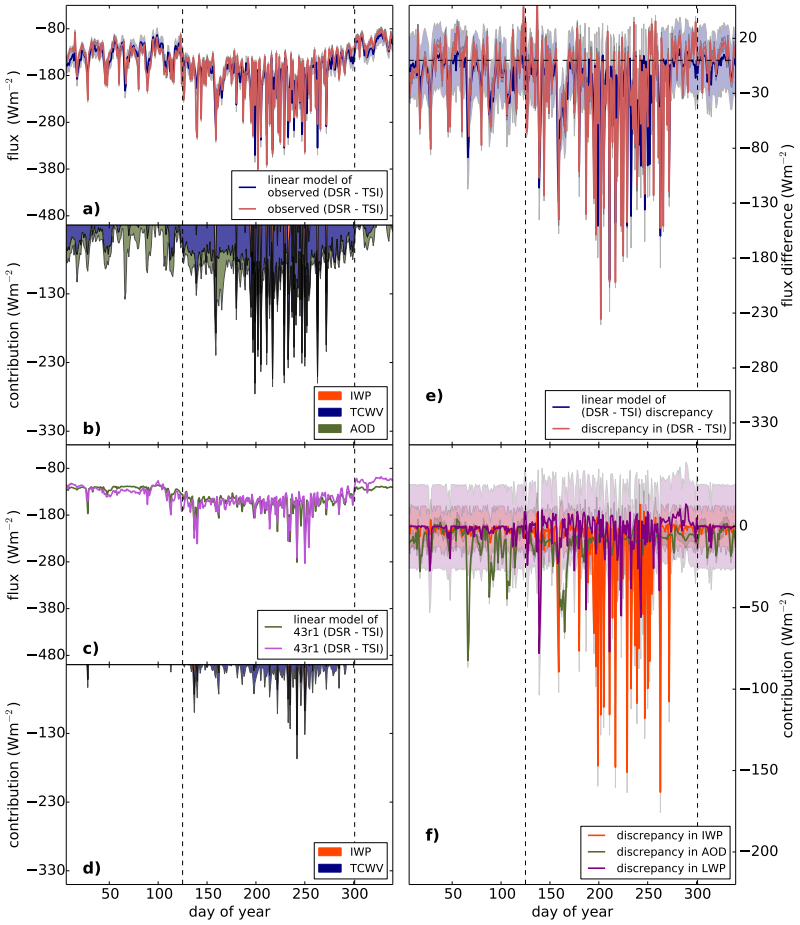

Figure 3.7: Downwelling shortwave radiation minus total solar irradiance (DSR - TSI), in observations and 43r1. Plot (a) shows DSR (blue) and the linear model (red) of (DSR - TSI) built from a linear combination of IWP (orange), TCWV (blue) and AOD (green) shown in plot (b). Plot (c) shows the 43r1 (DSR - TSI) (pink) and the linear model of 43r1 (DSR - TSI) (green) made up of IWP (orange) and TCWV (dark blue) in plot (d). Plot (e) shows the observation - 43r1 discrepancy in red, with a linear model (blue) of this discrepancy built from discrepancies in IWP (green), aerosol optical depth (orange), and LWP (purple) in plot (f). Negative contributions in plots (b), (d) and (f) indicate that an increase in that variable corresponds to a decrease in (DSR - TSI). Dashed lines indicate beginning and end of wet season.

Table 3.4: Shortwave surface fluxes: r^2 values from correlations between observed and 43r1 USR and DSR, and their discrepancy, to other variables for the whole year (days 7–341), 1st dry season (days 7–125), wet season (days 126–301) and 2nd dry season (days 302–341): Statistically significant (to $p \leq 0.001$) values are in bold. Italics indicate which variables were used in the linear model.

Radiative flux		**Variable**	**Whole year**	**1st dry season**	**Wet season**	**2nd dry season**
DSR	Observations	*AOD*	0.03	**0.19**	0.02	**0.67**
		TCWV	**0.38**	0.11	**0.31**	**0.46**
		IWP	**0.51**	**0.47**	**0.53**	0.10
		LWP	**0.28**	**0.31**	**0.22**	0.23
		Lin. mod.	**0.70**	**0.43**	**0.66**	**0.77**
	43r1	AOD	0.06	0.00	0.00	0.01
		TCWV	**0.51**	**0.64**	**0.32**	**0.75**
		IWP	**0.61**	**0.22**	**0.66**	0.08
		LWP	**0.38**	**0.63**	**0.13**	**0.58**
		Lin. mod.	**0.73**	**0.64**	**0.69**	**0.71**
	Discrepancy	*AOD*	0.04	**0.27**	0.02	**0.54**
		TCWV	0.00	0.01	0.02	0.09
		IWP	**0.51**	**0.33**	**0.54**	0.13
		LWP	**0.14**	**0.15**	**0.14**	0.17
		Lin. mod.	**0.56**	**0.41**	**0.56**	**0.63**
USR	Observations	DSR	**0.77**	**0.87**	**0.85**	**0.89**
	43r1	DSR	**0.70**	**0.96**	**0.75**	**0.90**
	Discrepancy	*DSR*	**0.82**	**0.74**	**0.85**	**0.92**
		Albedo	**0.48**	**0.22**	**0.46**	**0.53**
		Lin. mod.	**0.97**	**0.99**	**0.98**	**0.99**

AOD we generate a linear model (similar to that used by Miller et al. (2009)) which explains 70% of the observed variability in DSR over the whole year (Fig. 3.7a). Figure 3.7b shows the contributions to the linear model, where negative values indicate that an increase in that variable corresponds to a decrease in DSR. The exact role of water vapour in reducing DSR, whether directly through absorption or through cloudiness, is not clear. However, the correlation between TCWV and the cloud variables IWP and LWP are statistically insignificant, and Fig. 3.7 indicates that the influence of TCWV and IWP on the linear model of DSR are very different, suggesting that direct absorption may play a role. We repeat this process with the corresponding model variables and find that TCWV and LWP have a higher correlation coefficient with DSR than in the observations, especially in the dry season which is most likely due to the poor representation of AOD variability. We generate a linear model using IWP and TCWV, a combination which gives high correlation coefficients throughout the year (Fig. 3.7c,d).

We perform linear regressions on the observation minus model discrepancies in AOD, TCWV, IWP and LWP with the discrepancy in DSR. The discrepancy in IWP has a statistically significant correlation with that in DSR over the whole year, but particularly in the wet season ($r^2 = 0.54$). The correlation between the discrepancy in DSR and that in LWP is lower but still significant, while the discrepancy in TCWV has no significant correlation. The discrepancy in AOD has a significant correlation during the dry seasons ($r^2 = 0.27$ and 0.54, respectively). We combine the highest correlating discrepancies, IWP, AOD and LWP, in a linear model (Fig. 3.7e) which captures 56% of the variability in the observation minus model discrepancy in DSR over the year. Figure 3.7f shows that during the dry season the contribution to the linear model from AOD is largest, while during the wet season IWP largely determines the variability in the DSR discrepancy. From this we infer that model negative bias in cloud IWP explains a significant proportion of the overestimation of insolation reaching the surface.

This is particularly prevalent during the wet season, with day-to-day variations in AOD accounting for dry season overestimation of DSR at the surface.

Surface upwelling shortwave radiation

We consider the two factors which we would expect to produce an error in the model USR: discrepancy in DSR and the incorrect characterization of surface albedo. To estimate the surface albedo in the model and the observations, we take the ratio of USR to DSR or the proportion of DSR which is reflected upwards (inferred surface albedo, α). Figure 3.8b shows that the model generally has a positive bias in α, ranging from 0.22–0.29, contrasting with observations, where α varies between 0.14–0.29. The seasonal contrast is due to the semi-arid nature of the region: dry conditions during the dry seasons lead to a high albedo, but during the wet season green vegetation and higher soil moisture reduces the surface albedo. This is consistent with monthly values of the Normalized Difference Vegetation Index (NDVI, Fig. 3.8b) from NASA MODIS, which peaks during August/September, approximately corresponding to when there is a minimum in surface albedo. Care must be taken when comparing these values because we compare a model grid-average value with point measurements of DSR and USR, which is only valid if the point measurements are representative of the larger geographical area. This point is discussed further in section 3.4.

To quantify the impact of the model bias in α on USR, we calculate the model USR that is consistent with using observed α values. Figure 3.8a shows that this adjusted USR is much closer in magnitude and variability to the observed USR than the original model USR ($r^2 = 0.70$), suggesting a major source of error for the model USR originates from the poor characterization of the surface albedo over this study site.

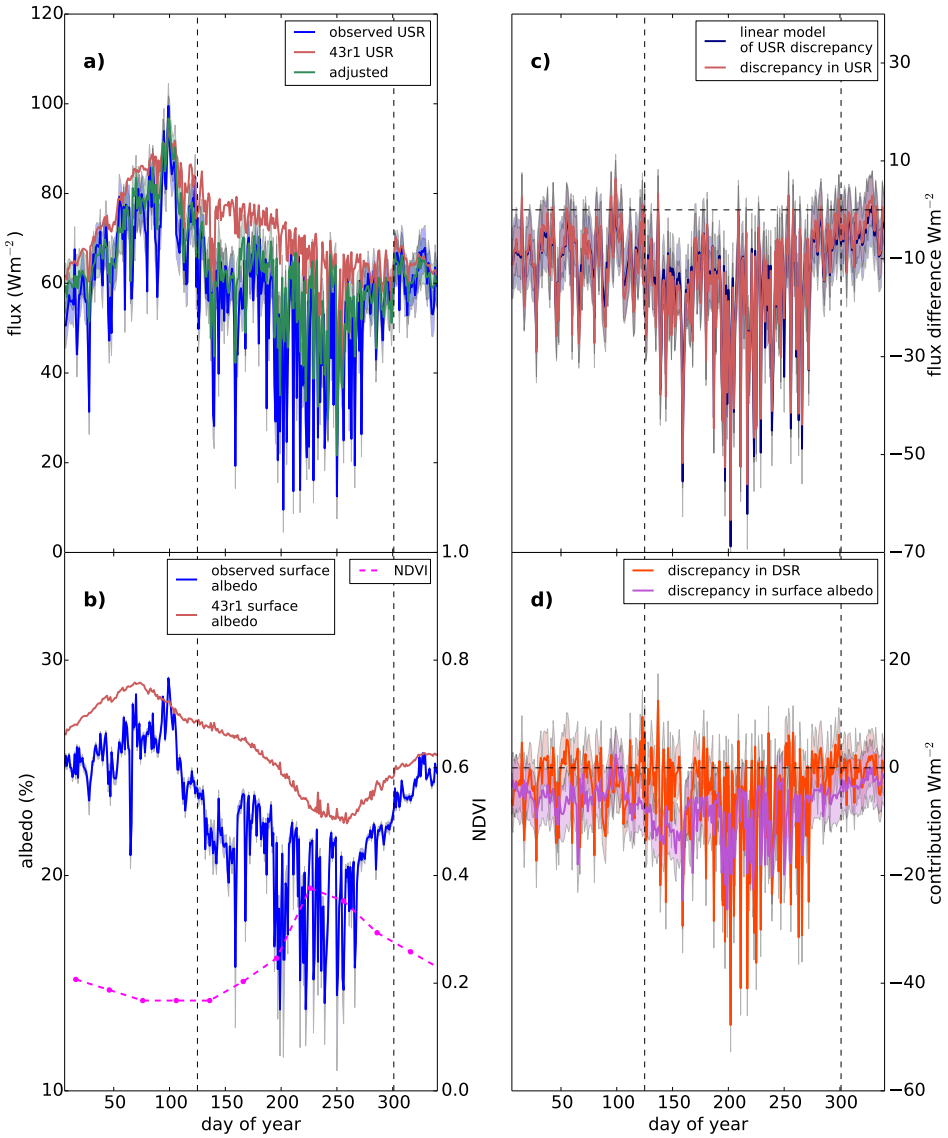

Figure 3.8: Plot (a) shows observed USR (blue), 43r1 USR (red) and 'adjusted' USR (calculated from 43r1 DSR and observed surface albedo, green). Plot (b) shows inferred surface albedo as calculated by the ratio USR/DSR from the observations (blue) and 43r1 (red), as well as NDVI (see text). Plot (c) shows USR discrepancy (red) and linear model (blue) of USR discrepancy with contributions in plot (d) from discrepancy in surface albedo (pink) and DSR discrepancy (orange). Dashed lines indicate beginning and end of wet season.

To determine whether the model bias in DSR or α has more of an impact on model USR, we build a linear model of the USR observation minus model discrepancy. We use the discrepancy in α and in DSR as the predictor variables (Table 3.4) as both are highly correlated with the discrepancy in USR (r^2 = 0.48, 0.82 respectively), but have a relatively low correlation with each other (r^2 = 0.13). Table 3.4 and Fig. 3.8c show that the linear model performs extremely well (r^2=0.97) over the whole year. Figure 3.8d shows that the larger contribution comes from the discrepancy in α, although the discrepancy in DSR is responsible for the large variations during the wet season. This suggests that increased surface reflectivity and overestimated DSR in the model combine to produce an overestimation in USR.

Surface downwelling longwave radiation

Following Miller et al. (2009), we use observed T_{a2}, TCWV and AOD to build a linear model that accounts for 88% of the observed variability in DLR (Table 3.5, Fig. 3.9a). A similar linear model but without AOD explains 99% of the 43r1 variability in DLR (Fig. 3.9c). Considering the full year, the linear model for 43r1 gives greater weight to the contribution from TCWV with respect to T_{a2} than the observational linear model (compare Fig. 3.9b to Fig. 3.9d), a feature which is dominated by wet season behaviour.

The discrepancy in TCWV is found to have little correlation with the observation model discrepancy in DLR, and is therefore not used further. This lack of correlation could be due to the relatively high correlation between observed and modelled TCWV (r^{-2} = 0.8, Table 3.3), resulting in other variables contributing more to the discrepancy in DLR. In contrast, the discrepancy in T_{a2} has a stronger correlation with DLR discrepancy in the wet season (r^2 = 0.46), while the discrepancy in AOD has a stronger correlation with DLR discrepancy in the

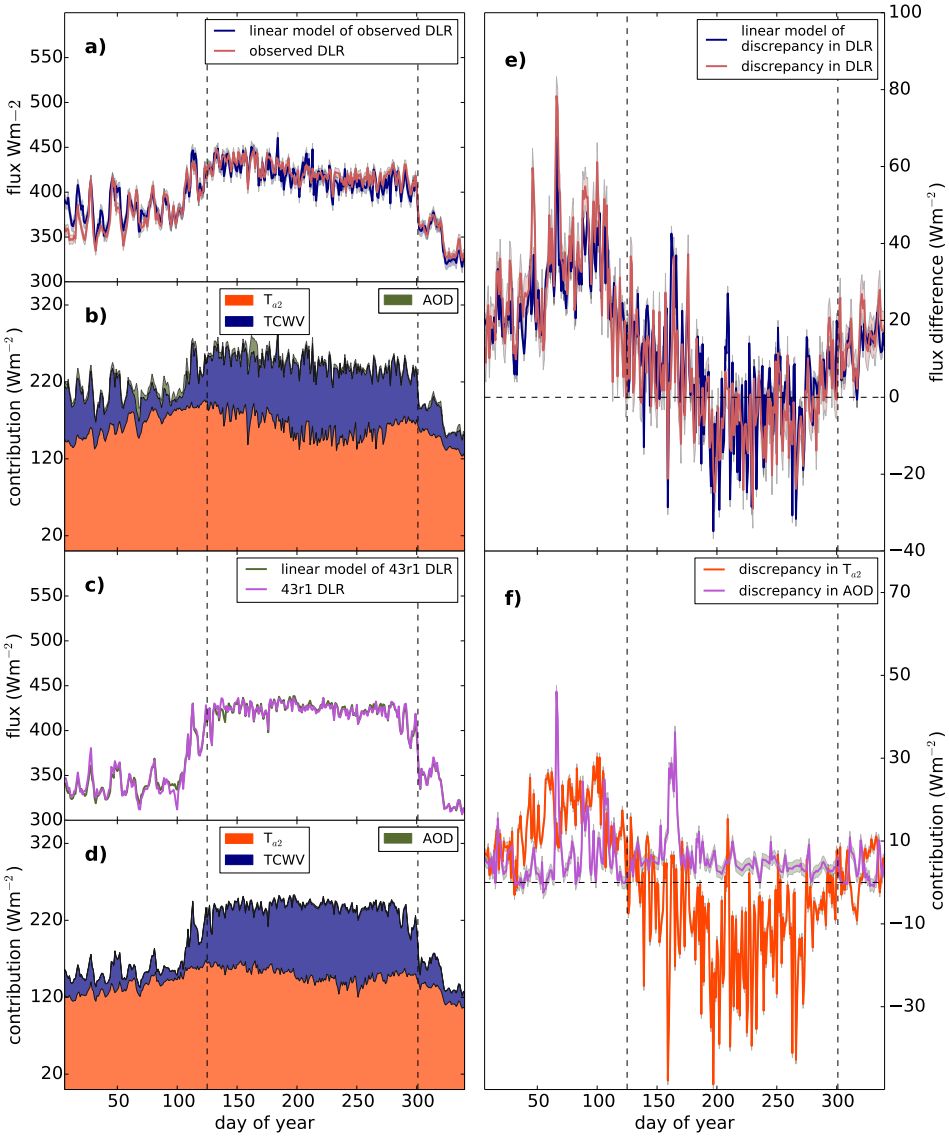

Figure 3.9: As Figure 3.7, but for downwelling longwave radiation, with observation/43r1 linear model contributions from TCWV (blue), 2 m air temperature (orange) and AOD (green) in plots (b) and (d) and discrepancy model contributions from 2m air temperature (orange) and AOD (pink) in plot (f).

Table 3.5: Downwelling longwave surface fluxes: r^2 values from correlations between observed and 43r1 DLR, and their discrepancy, to other variables for the whole year (days 7–341), 1st dry season (days 7–125), wet season (days 126–301) and 2nd dry season (days 302–341): Statistically significant (to $p \leq 0.001$) values are in bold. Italics indicate which variables were used in the linear model.

Radiative flux		**Variable**	**Whole year**	**1st dry season**	**Wet season**	**2nd dry season**
DLR	Observations	*TCWV*	**0.53**	0.13	**0.31**	**0.88**
		Temperature	**0.25**	**0.54**	**0.22**	**0.79**
		IWP	0.04	**0.26**	0.00	0.02
		LWP	**0.12**	**0.30**	0.04	0.26
		AOD	0.04	0.07	0.14	**0.36**
		ULR	**0.28**	**0.61**	**0.19**	**0.79**
		Lin. mod.	**0.88**	**0.82**	**0.81**	**0.96**
	43r1	*TCWV*	**0.91**	**0.89**	**0.74**	**0.97**
		temperature	**0.53**	**0.64**	**0.16**	**0.95**
		IWP	**0.18**	0.15	0.07	0.12
		LWP	**0.61**	**0.65**	**0.27**	0.44
		AOD	**0.31**	**0.14**	**0.16**	0.08
		ULR	**0.72**	**0.75**	**0.35**	**0.96**
		Lin. mod.	**0.99**	**0.97**	**0.98**	**0.99**
	Discrepancy	TCWV	**0.32**	0.00	**0.17**	0.01
		Temperature	**0.65**	**0.30**	**0.46**	0.15
		IWP	**0.12**	0.02	0.14	0.09
		LWP	**0.21**	**0.45**	0.07	0.18
		ULR	**0.60**	**0.25**	**0.48**	0.21
		AOD	**0.21**	**0.45**	0.07	0.18
		Lin. mod.	**0.75**	**0.67**	**0.52**	**0.51**

Radiative flux		**Variable**	**Whole year**	**1st dry season**	**Wet season**	**2nd dry season**
ULR	Observations	Temperature	**0.92**	**0.95**	**0.90**	**0.97**
		Net SW	**0.33**	**0.46**	**0.33**	0.04
		Net SW + DLR	**0.59**	**0.92**	**0.49**	**0.96**
	43r1	Temperature	**0.93**	**0.97**	**0.88**	**0.99**
		Net SW	**0.28**	**0.39**	0.11	0.10
		Net SW + DLR	**0.82**	**0.98**	**0.40**	**0.98**
	Discrepancy	Temperature	**0.87**	**0.73**	**0.80**	**0.73**
		Net SW	**0.33**	0.08	**0.47**	0.15
		Net SW + DLR	**0.70**	**0.51**	**0.64**	**0.66**

first dry season ($r^2 = 0.45$). We therefore build a linear model of the discrepancy in DLR with discrepancies from T_{a2} and AOD (Fig. 3.9e). These two variables collectively account for 75% of the DLR discrepancy variability over the whole year, with higher correlations in the dry season than the wet season ($r^2 = 0.67$ and 0.52, respectively). Figure 3.9f shows that the discrepancy in DLR is largely driven by the discrepancies in T_{a2}, with peaks in AOD contributing to isolated events.

Surface upwelling longwave radiation

ULR is determined by variations in skin temperature, T_s and emissivity, ϵ, through the Stefan Boltzmann law:

$$ULR = \epsilon\sigma T_s^4 + (1 - \epsilon)DLR, \tag{3.2}$$

where σ denotes Stefan-Boltzmann's constant (5.670×10^{-8} $\mathrm{Wm^{-2}\ K^{-4}}$) and the second term represents the longwave radiation absorbed by the surface. ULR

model error is therefore likely to arise due to errors in either ϵ or T_s. It is not possible to estimate ϵ from the observations, therefore we concentrate here on the directly emitted portion of ULR, given by the first term in equation 3.2, specifically the dependence on skin temperature. We bear in mind that the modelled emissivitiy and reflected portion of DLR from the surface may also be contributing to model error. We find that ULR and T_{a2} (our proxy for T_s) are highly correlated in both observations and 43r1 (Table 3.3.2), as expected. The observed minus model ULR discrepancy is also highly correlated to T_{a2}, suggesting that the errors in ULR are linked to those in T_s. Possible sources of error in T_s include errors in surface heating, ground heat storage and the partitioning between ULR and the turbulent (latent and sensible) heat fluxes. To explore the source of this temperature difference, we perform linear regressions of ULR first with absorbed shortwave radiation at the surface (net downward shortwave radiation flux, or DSR - USR), and then, with the addition of DLR, of total downward radiation flux (net downward shortwave radiation flux + DLR). The observed surface ULR is significantly correlated with observed net downward shortwave radiation flux through the year ($r^2 = 0.33$). We find that this correlation is improved when we linearly regress observed ULR with the total downward radiation flux ($r^2 = 0.59$), with the largest correlation during the dry season ($r^2 = 0.96$). We find a similar result using 43r1. The observation minus model discrepancy in ULR is highly correlated to the discrepancy in total downward radiation flux. Although it is difficult to fully disentangle the cause and effect relationship between the upwelling and downwelling longwave radiation fluxes, the suggestion through this analysis is that the dry season discrepancy in T_s arises through an underestimate in model DLR and is partially offset by an overestimate in net downward shortwave fluxes.

3.3.3 TOA radiative flux discrepancies

As with the surface budget, we examine the net radiation flux at the TOA (incoming solar - (OLR +RSR)) in both the model and observations (Fig. 3.6b). We find that despite large discrepancies in the RSR and OLR (Figs. 3.2 and 3.3) there is good agreement between the model and observed TOA budget, especially in the dry season. This is likely due to the RSR underestimate counteracting the OLR overestimate. The exception to this is the second part of the wet season, where the model does not capture the large variations seen in the observations. We now interpret OLR and RSR to establish which processes control observed and model variations, and their discrepancies.

TOA reflected shortwave radiation

We find that the shortwave component of the TOA budget has similar controls to DSR (Table 3.6) with significant correlations between observed RSR and cloud products (IWP and LWP, $r^2 = 0.56$ and 0.31, respectively). Control from IWP is strongest in the wet season, while the highest correlation with LWP and AOD is during the first dry season. Using LWP, IWP and AOD we build a linear model which explains 73% of the observed RSR variability over the course of the year, with the highest correlation during the wet season (Fig. 3.10a). IWP and LWP have the largest contribution during the wet season, with AOD contributing more in the dry seasons (Fig. 3.10b). Repeating the procedure with 43r1 shows very similar dependencies of 43r1 RSR on LWP and IWP, suggesting that the response to the cloud forcing is similar. Using the 43r1 IWP and LWP in a linear model, we can recreate 74% of the variability in 43r1 RSR (Fig. 3.10c).

Discrepancies in RSR and the predictor variables show that, as with DSR, the largest correlation with RSR discrepancy is that in IWP, followed by that in LWP

Table 3.6: TOA RSR fluxes: r^2 values from correlations between observed and 43r1 RSR , and their discrepancy, to other variables for the whole year (days 7–341), 1st dry season (days 7–125), wet season (days 126–301) and 2nd dry season (days 302–341): Statistically significant (to $p \leq 0.001$) values are in bold. Italics indicate which variables were used in the linear model.

Radiative flux		**Variable**	**Whole year**	**1st dry season**	**Wet season**	**2nd dry season**
RSR	Observations	*IWP*	**0.56**	**0.49**	**0.58**	0.24
		LWP	**0.31**	**0.37**	**0.24**	0.13
		AOD	0.01	**0.17**	0.01	0.29
		DSR	**0.62**	**0.21**	**0.83**	**0.67**
		Lin. mod.	**0.73**	**0.56**	**0.73**	0.43
	43r1	*IWP*	**0.70**	**0.33**	**0.69**	0.01
		LWP	**0.24**	**0.57**	0.07	0.37
		AOD	**0.11**	0.07	0.01	0.00
		DSR	**0.32**	0.10	**0.77**	0.35
		Lin. mod.	**0.74**	**0.51**	**0.71**	0.23
	Discrepancy	*IWP*	**0.43**	**0.20**	**0.44**	0.07
		LWP	**0.16**	**0.23**	**0.15**	0.12
		AOD	0.05	0.13	0.03	0.01
		DSR	**0.80**	**0.51**	**0.85**	0.39
		Lin. mod.	**0.55**	**0.33**	**0.55**	0.07

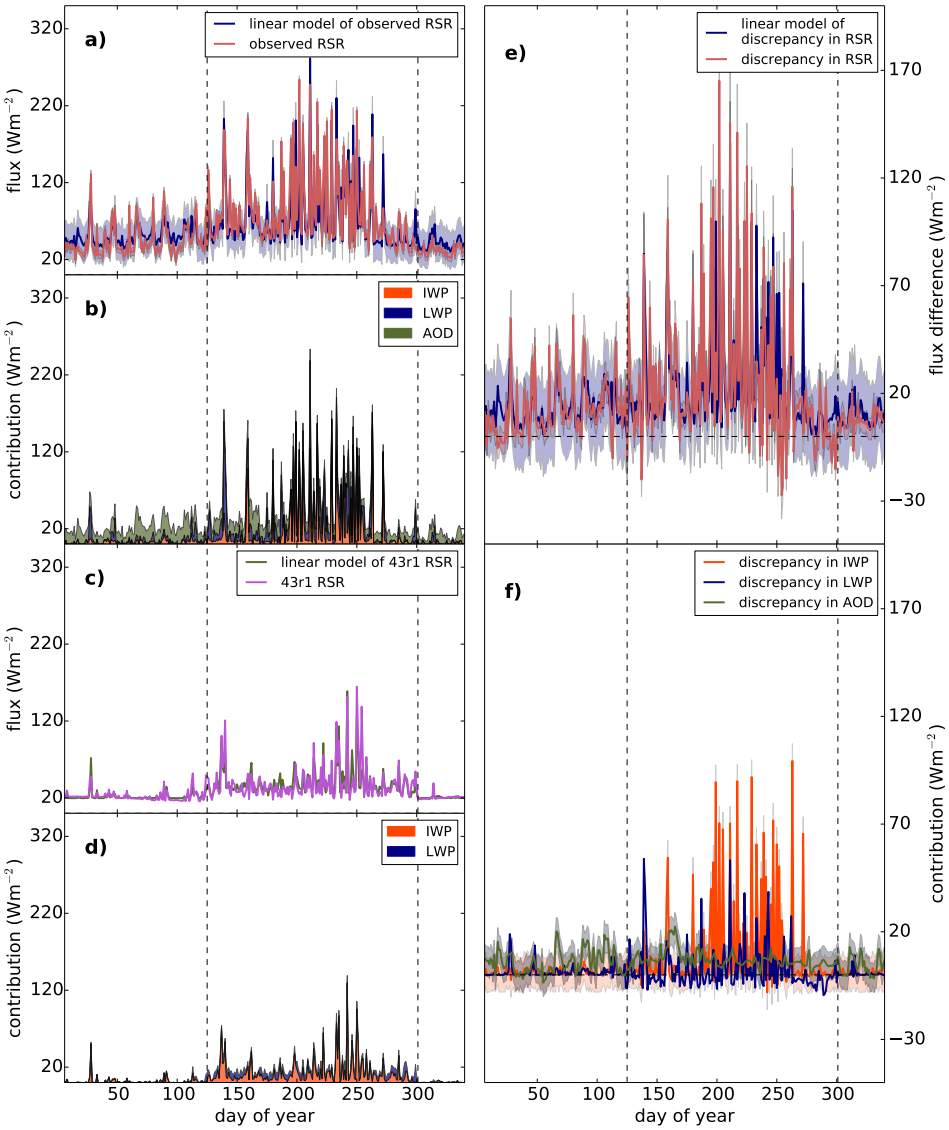

Figure 3.10: As Figure 3.7, but for reflected shortwave radiation at the TOA, with observation/43r1 linear model contributions from IWP (orange), LWP (blue) and (observations only) AOD (green) in plots (b) and (d) and discrepancy model contributions from IWP (orange), LWP (blue) and AOD (green) in plot (f).

(Table 3.6). This suggests that the underlying discrepancies in RSR have the same cause as those in DSR, namely the underestimation of IWP and LWP, especially in the wet season. Indeed, we see a very strong correlation between DSR and RSR both in the observations and 43r1 individually, as well as a high correlation between the observation-model discrepancy in DSR and RSR. By combining the discrepancies in IWP, LWP and AOD we build a linear model which explains 55% of the variability in the discrepancy of RSR over the course of the year (Table 3.6). Comparison of the discrepancy models for both RSR (Figs. 3.10e and f) and DSR (Figs. 3.7e and f) shows that the RSR discrepancy model is less dependent on AOD, but also includes a dependency on LWP.

TOA outgoing longwave radiation

We finish our examination of the radiation fluxes with the OLR. There is a significant correlation between observed OLR and TCWV, IWP and LWP, with the strongest correlation between IWP/LWP and OLR during the dry season, and TCWV having a similar correlation in both the first dry and wet season. Upper tropospheric humidity (UTH) has a statistically significant, albeit lower, correlation during the wet season ($r^2 = 0.13$). ULR, which we might expect to influence OLR under clear-sky conditions, does not have a significant correlation during the dry season, though it does during the wet season. By combining IWP, LWP and TCWV, we build a linear model which explains 60% of the observed variability throughout the year (Table 3.7, Fig. 3.11a). Much of the seasonal cycle in this linear model is driven by TCWV, while the day-to-day variability during the wet season comes from variations in IWP and LWP (Fig. 3.11b). Again, these contributions are shown as negatives in the contributions plot, as an increase in these variables leads to an decrease in OLR.

We see a similar pattern with 43r1, though LWP has a lower correlation with

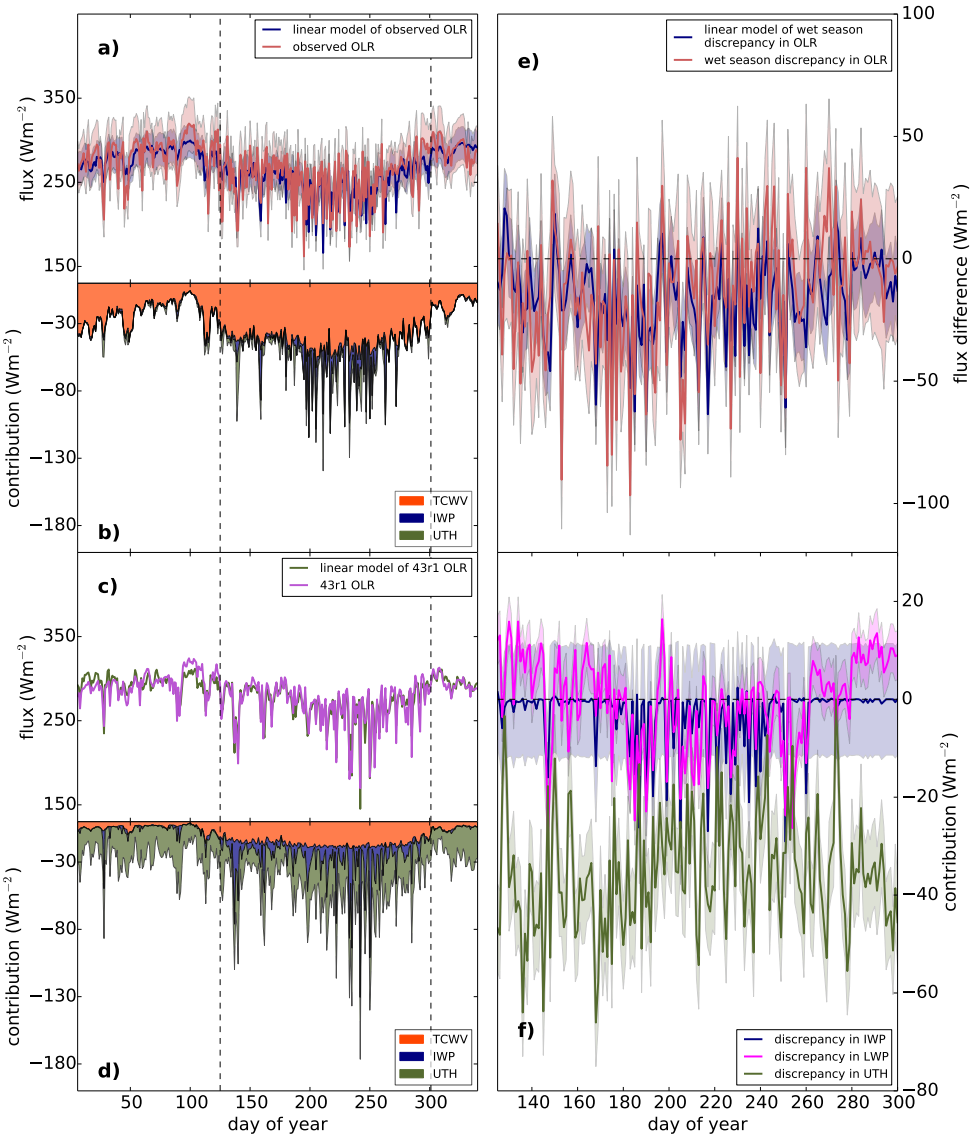

Figure 3.11: As Figure 3.7, but for outgoing longwave radiation at the TOA, with observation/43r1 linear model contributions from TCWV (orange), IWP (blue) and UTH (green) in plots (b) and (d) and discrepancy model contributions from IWP (blue) and UTH (green) and LWP (pink) in plot (f). Negative contributions in plots (b), (d) and (f) indicate that an increase in that variable correpsonds to a decrease in OLR.

OLR during the year ($r^2 = 0.20$), and no significant correlation in any individual seasons. Instead, IWP has a stronger correlation ($r^2 = 0.69$), and UTH has a higher correlation than the observations ($r^2 = 0.54$ rising to 0.87 during the wet season). The linear model from TCWV, IWP and UTH (Fig. 3.11c) captures most of the variability in 43r1 OLR ($r^2 = 0.85$), though TCWV contributes less to the linear model than in the observations (Fig. 3.11d).

As noted above, for the majority of the days examined, 43r1 OLR falls within the uncertainty bounds of the observations, with the exception of the wet season. We therefore restrict our discrepancy model to just this period. There is little correlation between the discrepancy in wet season IWP, ULR or UTH and the discrepancy in OLR, and no significant correlation with TCWV or LWP (Table 3.7). We therefore build a linear model of the discrepancy in wet season OLR using the discrepancy in IWP, ULR and UTH, producing a model with correlation coefficient of $r^2 = 0.36$ (Fig. 3.11). From the contributions to this model (Fig. 3.11), we see that the largest contribution to this model is from the discrepancy in UTH, with minor contributions from IWP and LWP, suggesting that model humidity profiles are the largest cause of OLR discrepancies.

3.4 Discussion and concluding remarks

The purpose of this study has been to characterise differences in TOA and surface radiation fluxes between ECMWF's IFS 43r1 and observations from GERB/SEVIRI; to link these discrepancies to differences in physical processes; and to examine links between surface and TOA flux discrepancies. We do this using some simple statistics and by extending the methods of multivariate linear models used by Miller et al. (2009).

We are able to link observation - model discrepancies in physical processes to

Table 3.7: TOA OLR fluxes: r^2 values from correlations between observed and 43r1 OLR , and their discrepancy, to other variables for the whole year (days 7–341), 1st dry season (days 7–125), wet season (days 126–301) and 2nd dry season (days 302–341): Statistically significant (to $p \leq 0.001$) values are in bold. Italics indicate which variables were used in the linear model.

Radiative flux		**Variable**	**Whole year**	**1st dry season**	**Wet season**	**2nd dry season**
OLR	Observations	*TCWV*	**0.43**	**0.33**	**0.35**	0.10
		IWP	**0.34**	**0.40**	**0.38**	0.39
		LWP	**0.23**	**0.34**	**0.17**	0.03
		ULR	**0.07**	0.01	**0.26**	0.00
		UTH	**0.13**	0.07	**0.14**	0.03
		Lin. mod.	**0.60**	**0.47**	**0.58**	0.13
	43r1	*TCWV*	**0.40**	**0.13**	**0.36**	0.13
		IWP	**0.69**	**0.39**	**0.72**	**0.52**
		LWP	**0.20**	0.07	0.04	0.03
		ULR	0.02	0.01	0.08	0.05
		UTH	**0.54**	**0.40**	**0.64**	0.23
		Lin. mod.	**0.85**	**0.60**	**0.87**	**0.43**
	Discrepancy	TCWV			0.03	
		IWP			**0.15**	
		LWP			0.02	
		ULR			**0.14**	
		UTH			**0.10**	
		Lin. mod.			**0.35**	

those in radiation fluxes. The most striking of these impacts arises from a lack of ice cloud in the model, manifested as an underestimate in the ice water path, which causes large wet season discrepancies in shortwave radiation. This lack of ice cloud leads to too much shortwave radiation reaching the surface, and not enough being reflected at the TOA.

This effect is exacerbated by the use of an aerosol loading climatology which typically underestimates the real amount of aerosol present in the atmosphere over Niamey and is the major source of the model overestimate of surface downwelling shortwave radiation (DSR) in the dry season. This agrees with an assessment of an earlier cycle of the IFS, 32r3, used for a re-analysis by Agustí-Panareda et al. (2010), though here we directly link the lack of cloud and aerosol loading to an overestimation of DSR. Marsham et al. (2016), in their study of controls of surface and TOA radiation budgets in a similar site in Algeria (Bordj-Badji Mokhtar at 21.4 °N 0.9 °E) also find that net shortwave radiation at the surface is controlled by a balance of clouds, AOD and TCWV, consistent with our results here. The positive bias in model DSR leads to an overestimation of net shortwave absorption by the surface and overestimation of upwelling shortwave radiation (USR). However, we find that for reflected shortwave radiation (RSR) at the TOA, the largest contribution to the observation - model discrepancy remains the underestimated cloud ice water path.

Turning to the longwave regime, we find that the model bias in ice water path also contributes to a positive model-observation bias in wet season OLR, though discrepancies in upper tropospheric humidity and upwelling longwave radiation (ULR) also play a role. While we have limited our analysis of ULR to the directly emitted portion, this analysis points to a significant role of underestimated skin temperature in the discrepancy in ULR. The origin of this discrepancy in skin temperature is difficult to identify: we find that the model generally shows a positive surface energy budget (where downwelling is the positive direction),

while the observations suggest the surface energy budget is generally negative. This would logically result in an enhanced skin temperature in the model and an overestimation of ULR. The higher correlation of ULR with a combination of net downward shortwave and downwelling longwave radiation (DLR) at the surface may indicate complex feedbacks. A cooler near-surface temperature profile in the model could lead to lower DLR which would in turn lead to lower longwave absorption at the surface and therefore a lower skin temperature. Clearly, separating the cause and effect of the underestimated skin temperature is difficult. However, this temperature discrepancy, regardless of origin, can be directly linked to the discrepancy in DLR, particularly in the wet season. Marked peaks in model observation DLR discrepancies result from significant aerosol events which are not captured in the model aerosol climatology.

There are limitations to the approach we have taken here. A significant caveat relates to the comparison of point measurements with area-averages. However, assuming a non-static atmosphere, the use of daily averages rather than instantaneous measurements from the surface (point site), satellite ($\sim$10 km resolution) and model ($\sim$29 km resolution) should, to some degree account for the mis-match in spatial scales given the higher native temporal resolution of the surface (1s) and satellite observations (15 minute). The qualitative agreement in the temporal variability in NDVI from MODIS ($\sim$110km) and the surface albedo derived from the ARM site gives confidence in the general representativeness of the site in terms of surface properties. We also use the upper bounds of instrumental uncertainty to avoid over-interpreting model-observation discrepancies which lie within the bounds of measurement error.

The method we have used here does rely heavily on the availability of high-frequency measurements of radiative and meteorological variables from surface sites, which are not widely available. However, we find that larger-scale satellite products, such as ice and liquid water path, have been integral to our analysis of

TOA fluxes in particular, suggesting this method could potentially be extended to larger spatial scales using suitably validated satellite products.

In summary we have shown in this study that the use of multivariate linear models can give us deeper insight into how physical processes in 43r1 impact the evolution of radiative fluxes at the surface and the TOA in Niamey as well as identifying where shortcomings exist in the current version of the model.

Appendices

A ERA-I - 43r1 comparison

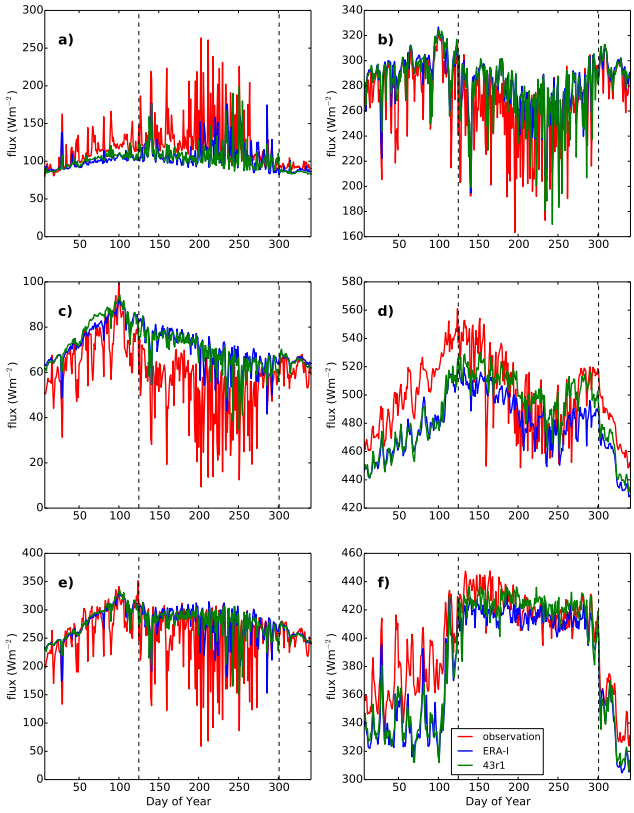

Figure A1: Comparison between observations (red), ERA-Interim (blue) and 43r1 (green) for (a) TOA reflected shortwave; (b) TOA outgoing longwave; (c) surface upwelling shortwave; (d) upwelling longwave; (e) downwelling shortwave; and (f) downwelling longwave radiation fluxes. Dashed lines indicate beginning and end of wet season.

B Linear model equations

The equations for the linear models used in section 3.3.2, where primes indicate observation - model discrepancies.

Surface downwelling shortwave radiation:

$$DSR' \text{ W m}^{-2} = (3 \pm 2) \text{ W m}^{-2} + (-209 \pm 12) \text{ W kg}^{-2} \times IWP' \text{ kg m}^{-2} + (-29 \pm 4) \text{ W m}^{-2} \times AOD' + (-181 \pm 25) \text{ W kg}^{-2} \times LWP' \text{ kg m}^{-2}, \quad (3.3)$$

Surface upwelling shortwave radiation:

$$USR' \text{ W m}^{-2} = (-1.5 \pm 1.8) \text{ W m}^{-2} + (0.201 \pm 0.003) \times DSR' \text{ W m}^{-2} + (229 \pm 5) \text{ W m}^{-2} \times \alpha'. \quad (3.4)$$

Surface downwelling longwave radiation:

$$DLR' \text{ W m}^{-2} = (7.2 \pm 0.7) \text{ W m}^{-2} + (7.3 \pm 0.2) \text{ W m}^{-2} \text{ K}^{-1} \times T' \text{ K} + (16.3 \pm 1.4) \text{ W m}^{-2} \times AOD' \quad (3.5)$$

TOA reflected shortwave radiation:

$$RSR' \text{ W m}^{-2} = (5 \pm 2) \text{ W m}^{-2} + (127 \pm 8) \text{ W kg}^{-2} \times IWP' \text{ kg m}^{-2} + (125 \pm 16) \text{ W kg}^{-2} \times LWP' \text{ kg m}^{-2} + (30 \pm 7) \text{ W m}^{-2} \times AOD' \quad (3.6)$$

TOA outgoing longwave radiation:

$$OLR' \text{ W m}^{-2} = (23 \pm 5) \text{ W kg}^{-2} + (-37 \pm 11) \text{ W kg}^{-2} \times IWP' \text{ kg m}^{-2} + (0.5 \pm 0.1) \times ULR' \text{ W kg}^{-2} + (-66 \pm 9) \text{ W kg}^{-2} \times UTH' \quad (3.7)$$

I acknowledge a number of organisations for provision of data. Data were obtained from the Atmospheric Radiation Measurement (ARM) climate research facility, a U.S. Department of Energy Office of Science User Facility sponsored by the Office of Biological and Environmental Research. Data were also obtained from CMSAF (Schulz et al., 2009), which are copyright (2017) EUMETSAT. GERB HR data were made available by the Royal Meteorological Institute of Belgium (RMIB). I obtained NDVI data from NASA Earth Observations. Additionally, I would like to thank Robin Hogan at ECMWF for the 43r1 output and help with interpreting it, and R.L. Miller for his helpful advice on the use of multivariate linear models.

Chapter 4

Probing the role of SST, aerosol and water vapour in driving observed and CMIP5 simulated radiative flux variability over west Africa

Abstract

We explore the ability of general circulation models that took part in the fifth phase of the Coupled Model Intercomparison Project (CMIP5) to recreate the observed seasonal variability in top-of-the-atmosphere (TOA) and surface radiation fluxes over west Africa. This provides an important test of the CMIP5 models' ability to describe the radiative energy partitioning, which is fundamental to our understanding of the current climate and its future changes, including the

west African monsoon. As a primary reference, we use 15 years of the monthly Clouds and the Earth's Radiant Energy System (CERES) Energy Balanced and Filled (EBAF) product, which we compare to other satellite products, reanalysis and surface station data. We find that the CMIP5 multi-model mean is generally within the range given by the reference products, though the range of model seasonal cycles is large. We use seasonal and regional contrasts in all-sky fluxes to discuss to what degree the west African monsoon and its representation in numerical models may affect the different radiation components studied here. We find that the models tend to simulate a monsoon which starts later, and does not progress as far north, as that in the observations. We compare coupled model output with atmosphere-only models with observed SSTs, finding that although there are some improvements when SSTs are prescribed, for example the capture of the 'little dry season' in the coastal region, there are still differences in the timing and extent of the monsoon when interpreted through radiation fluxes. Using clear-sky surface fluxes, we find that the models tend to have more downwelling shortwave radiation, and less downwelling longwave radiation, than in EBAF, consistent with past research. We find that models that are drier and have lower aerosol loading tend to have the largest differences. We find evidence that variations in aerosol have a larger effect in modulating downwelling shortwave radiation than water vapour in EBAF, while the opposite effect is seen in the majority of CMIP5 models.

Author contributions: A version of this chapter is under review in *Earth and Space Science*. I performed the analysis and wrote the article with contributions and editing from Martin Wild, Helen Brindley, Doris Folini and Paul Palmer.

4.1 Introduction

It is crucial that general circulation models (GCMs) are able to capture the observed variability in top-of-the-atmosphere (TOA) radiation balance in order to improve confidence in future climate projections. The Coupled Model Intercomparison Project, Phase 5 (CMIP5, Taylor et al., 2012, see chapter 2) provides a set of model simulations of both historical and future climates. These have been extensively compared to observations for model evaluation and to help understand inter-model spread due to uncertain feedbacks, such as those associated with clouds (Zhang et al., 2005; Stanfield et al., 2014; Dolinar et al., 2015; Trenberth et al., 2015). Globally, although CMIP5 mean biases of TOA fluxes are much reduced from CMIP3, an earlier phase of the intercomparison project, this is largely from error cancellation, and regional biases remain high, particularly in regions which are convectively active (Li et al., 2013).

Indeed, while much focus has been on the global mean radiation budget in CMIP5, the ability of GCMs to describe observed patterns in radiation variability at regional scales is equally important. For example, accurate estimates of changes to synoptic-scale weather systems and associated changes in temperature, atmospheric water vapour, aerosol loading and surface characteristics are needed on a regional scale in order for appropriate planning and mitigation. In order to understand how these systems may change, and the subsequent regional impact on the radiation budget, it is vital to understand to what extent they can be accurately modelled in historical simulations. The region focused on here, west Africa, described in more detail in sec. 4.2, is one such region, where the radiation budget is heavily determined by the progression of the west African monsoon (WAM, Sultan and Janicot, 2003), but also other competing factors such as the influence of aerosols from mineral dust and the burning of biomass.

Satellite data are typically recorded at appropriate spatial resolution, coverage

and time scales for GCM evaluation. One such product, the Clouds and Earth's Radiation Energy System (CERES, Wielicki et al., 1996) Energy Balanced and Filled (EBAF, Loeb et al., 2009) TOA and surface products has provided a key part of our understanding of radiation budgets, and has been used extensively (e.g., Li et al., 2013; Calisto et al., 2014; Dolinar et al., 2015). However, surface radiation fluxes and atmospheric absorption retrieved from satellite data are not an observational 'truth', and while there has been validation on a global scale (Rutan et al., 2015), significant observational uncertainties remain (Kato et al.).

Our aim here is twofold. The first is to understand to what extent the CMIP5 models are able to describe the regionally integrated seasonal variability in surface and TOA radiation fluxes over west Africa, using satellite products, reanalysis and surface measurement sites as references. Biases in the radiation fields are examined in relation to cloud radiative effects, water vapour and aerosol. Second, we attempt to interpret reference and model differences common to many CMIP5 models. In particular, we explore a) to what extent the misrepresentation of radiation biases associated with the WAM progression can be attributed to biases in coupled model sea-surface temperatures; and b) influences of aerosols and water vapour on both atmospheric clear-sky shortwave absorptivity and clear-sky downwelling radiation at the surface.

4.2 West African region

4.2.1 Characteristics

Radiative processes in the west African region are affected by the presence of, and interactions between, the WAM and a variety of aerosols including mineral dust, marine and biomass burning aerosols. The climate in the southern part

of this region is strongly driven by the WAM: during the dry season, northerly winds lead to high temperatures, low humidity and high aerosol loading from Saharan mineral dust, while the wet season is characterized by humid air from the Atlantic, high cloud coverage and precipitation (Slingo et al., 2008; Knippertz et al., 2015b).

However, within west Africa there are a number of distinct regimes, with different meteorology, aerosols and surface characteristics which influence the TOA radiation fluxes. Fig. 4.1a illustrates the extent of the three regions chosen here: the Sahel is defined as 10–20°N, 12°W–15°E, similar to that used by Zhou et al. (2007); the Sahara as 20–30°N, 10°W–20°E; the coastal region as 5–10°N, 8°E–8°W, as used by Knippertz et al. (2015a); and the wider west African region as 5–30°N, 15°W–20°E. The Sahara is arid and is characterised by a dry, dusty climate and high surface albedo. The Sahel is a semi-arid region: typically dry and dusty in the dry season, contrasting with higher humidity and precipitation in the wet season (see Chapter 3). A number of large and rapidly growing cities on the Guinea Coast produce increasing emissions of greenhouse gases and anthropogenic aerosols, in addition to the naturally occurring marine and biogenic aerosols (Knippertz et al., 2015a,b).

The migration of the WAM determines the seasonal cycle of the radiation fluxes across west Africa, and we illustrate its progression using OLR from CERES (Fig. 4.1), which decreases as cloud cover increases. The main part of the monsoon, characterised by deep convective cloud, high precipitation and typical OLR values of 180–220 Wm^{-2}, is over the ocean, and therefore south of the shown landmass, from December - February (Fig. 4.1a). By April it passes up over the coastal region (Fig. 4.1b), reaching its northernmost extent over the Sahel during July/August (Fig. 4.1c), before passing back over the coastal region as it retreats in the autumn (Fig. 4.1d). This results in the coastal region experiencing a ‘little

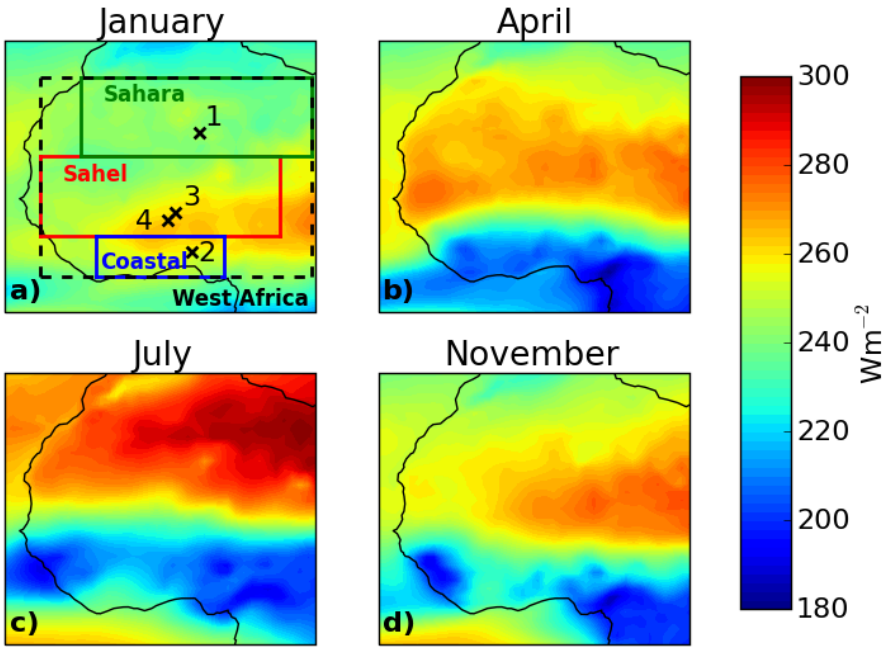

Figure 4.1: Monthly means of CERES OLR 2001–2015 inclusive for a) January, b) April, c) July and d) November, to illustrate mean monsoon migration. Study regions are marked on plot a) and are coastal region (blue), Sahel (red), Sahara (green) and wider west Africa (dashed black), as defined in sec. 4.2. Crosses mark position of surface measurement stations (1: Tamanrasset, 2: Ilorin, 3: Banizoumbou and 4: Ouagadougou), with locations given in sec. 4.3. Tamanrasset and Ilorin are part of both BSRN and AERONET, while Ouagadougou and Banizoumbou are part of AERONET only.

dry season', with a period of comparatively dry weather lasting a few weeks in late July–August (Omotosho, 1988; Adejuwon and Odekunle, 2006).

The increased cloud cover associated with the monsoon leads to an increase in the shortwave radiation reflected to space, thus increasing all-sky RSR and decreasing all-sky downwelling shortwave radiation (DSR) at the surface. This leads to a maximum in RSR and a minimum in DSR in August in the Sahel (Fig 4.2b and 4.2j) and the coastal region (Fig 4.2c and 4.2k). Conversely, as the clouds are cooler than the underlying surface, they have the effect of reducing OLR, with an annual decrease observed first in the coastal region, and then in the Sahel (Fig 4.2f-g). The increase in cloud cover also leads to an increase in all-sky downwelling longwave radiation (DLR) at the surface in the monsoon months (Fig 4.2n-o) from increased downwelling emission from clouds in addition to the increased emission from higher summer atmospheric temperatures. In this study, we use radiative fluxes, in particular OLR, as a proxy for monsoon position.

4.2.2 Previous modelling studies: common GCM problems

The physical mechanisms that link the WAM to the intertropical convergence zone (ITCZ) and sea surface temperatures (SSTs), and therefore have a strong influence on African rainfall (Vizy and Cook, 2002; Caniaux et al., 2011), have proven challenging for GCMs. For example, annual mean zonal SST gradients are reversed with respect to observational gradients in most CMIP5 models, with only small improvements from CMIP3 (Richter et al., 2014). Martin et al. (2014) find that spatial distribution biases of SSTs in CMIP5 lead to incorrect teleconnections between Atlantic multidecadal variability and Sahelian rainfall. These coupled-model SST biases influence WAM dynamics, leading to a southward shift in the ITCZ in comparison to the Atmospheric Model Inter-comparison project, AMIP,

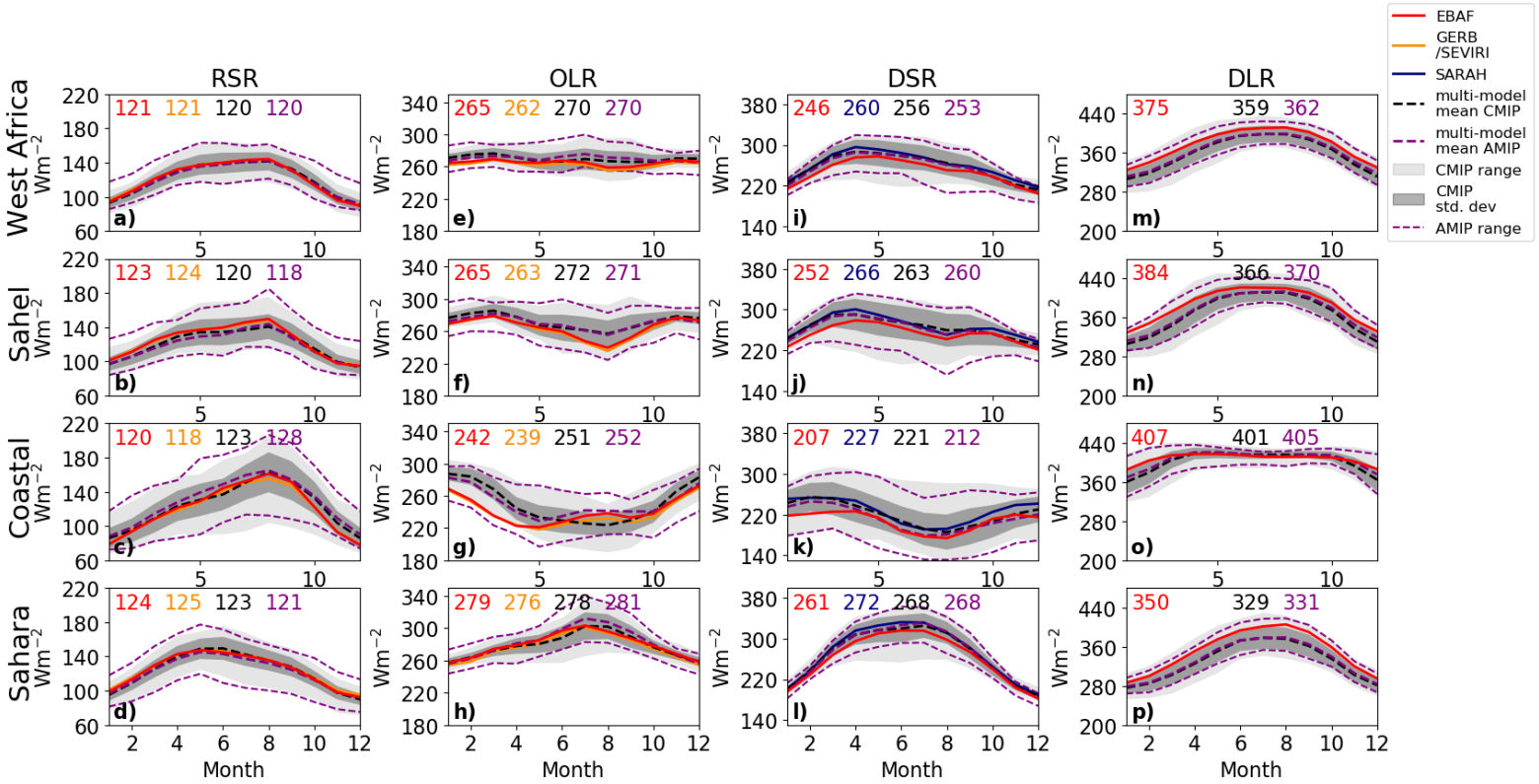

Figure 4.2: Climatology of monthly all-sky TOA and surface radiation fluxes: of reflected shortwave radiation (RSR), outgoing longwave radiation (OLR), downwelling shortwave radiation (DSR) and downwelling longwave radiation (DLR) in study regions (sec. 4.2) from EBAF (full years, 2001–2015 inclusive), GERB/SEVIRI (2005–2014), SARAH (2005–2014) and CMIP5 and AMIP models (1990–2004) (Table C1). Light shading marks range of CMIP models, dark shading marks one standard deviation. Thin dashed line marks range of AMIP models. Inset numbers indicate annual average of climatology, with colours corresponding to data sets as marked in legend.

the atmosphere-only, prescribed-SST modelling experiment of CMIP5 (Roehrig et al., 2013). Interannual variations in the monsoon, for example through Sahelian and coastal rainfall, are also linked to variability in SSTs (Tippett and Giannini, 2006). Difficulties with modelling the WAM do not originate with Atlantic SSTs alone, however. Using AMIP simulations, Hannak et al. (2017) find that too much shortwave radiation reaches the surface in the coastal region, a consequence of too little high cloud cover, with these clouds also being too high. Low cloud cover over the coastal region has a large effect on solar radiation (Knippertz et al., 2011). For a more detailed description of the atmospheric dynamics of the WAM, we refer the reader to Cook and Vizy (2006), and for a comprehensive overview of the WAM in CMIP5, to Roehrig et al. (2013).

Aerosols also have a significant impact on the radiation budget (Slingo et al., 2006; Milton et al., 2008; McFarlane et al., 2009; Ridley et al., 2014; Ansell et al., 2014; Banks et al., 2014) in the region, which can also lead to modelling biases. In particular, a number of studies have linked GCM overestimations of clear-sky shortwave fluxes at the surface to both water vapour and aerosol optical depth (Wild, 1999; Wild et al., 2006; Freidenreich and Ramaswamy, 2011), particularly in regions with high dust or biomass burning aerosol loadings.

4.3 Data and Methods

4.3.1 Reference products and CMIP5

We use a range of reference products to evaluate the CMIP5 models, the primary of which is CERES EBAF. Measurements from the CERES instruments form the basis of CERES SYN1deg edition 4 (Doelling et al., 2013; Rutan et al., 2015; Doelling et al., 2016), which provides global surface and TOA radiative

fluxes on a 1° x 1° grid. Closely linked is EBAF edition 4, which adjusts SYN1deg to be compatible with observed estimates of ocean heat storage on a decadal global mean scale (Loeb et al., 2009, 2012, 2018). We use monthly TOA radiation fluxes: incident solar radiation (ISR) and both all-sky and clear-sky RSR and OLR. We also use both all- and clear-sky DSR, ULR and DLR from EBAF Surface (Kato et al., 2013). From SYN1deg we use aerosol optical depth (AOD) at 500nm and total column water vapour (TCWV), both of which are used as inputs to compute radiation fluxes in SYN1deg (Rutan et al., 2015). Water vapour profiles are input from the Goddard Earth Observing System (GEOS) model version 4 and 5.2, while AOD comes from the Moderate Resolution Imaging Spectroradiometer (MODIS) and Multi-scale Atmospheric Transport and Chemistry (MATCH) model (Collins et al., 2001), a chemical transport model which assimilates MODIS data. At the time of this study, CERES data were available from March 2000–December 2016.

We compare the EBAF and SYN1deg against other products and observations, at regional scales and also at four surface measurement stations. Using a number of independent observational products provides an indication of the uncertainty range of the references, which can then be used to assess the CMIP5 outputs. For the regional analysis, we use two Climate Monitoring Satellites Application Facility (CMSAF) products from February 2004–April 2015: GERB/SEVIRI edition 2 TOA all-sky broadband radiation fluxes (Clerbaux et al., 2017), and DSR from the Surface Solar Radiation Data Set - Heliosat (SARAH) Ed. 2 (Pfeifroth et al., 2017). We also use TCWV from the European Centre for Medium-Range Weather Forecasts (ECMWF) ERA-Interim reanalysis (ERA-I, Dee et al., 2011). We download all of GERB/SEVIRI, SARAH and ERA-I at a 1° x 1° resolution.

Surface measurements are scarce in this region: we use measurements from two surface measurement sites, which are part of both the Baseline Surface Radiation Network (BSRN, Ohmura et al., 1998) and the Aerosol Robotic

Network (AERONET, Holben et al., 1998), and an additional two sites from just AERONET. These sites, Tamanrasset, Algeria (22.8°N, 5.5°), Ilorin, Nigeria (8.5°N, 4.6°W), Banizoumbou, Niger (12.2°N, 1.4°W) and Ouagadougou, Burkina Faso (13.5°N, 2.7°W) are marked in Fig. 4.1. At Tamanrasset and Ilorin, all-sky and clear-sky DSR and all-sky DLR are inferred from the BSRN instruments, using the method from Long and Ackerman (2000) and Long and Turner (2008) for clear-sky inferences. Due to insufficient data availability at Iloirn and Tamanrasset, clear-sky DLR estimates are not available. AOD and TCWV are available from the AERONET instruments, at all four sites. We use AOD at 500nm, except for at Ouagadougou, where we use 440nm. As can be seen in Fig. 4.1a, Tamanrasset is within the Saharan region, Ilorin the coastal region, and Banizoumbou and Ouagadougou in the Sahel. We use data from these sites to validate the satellite and reanalysis products at the closest grid points. All data products used in the analysis are listed in Appendix C: the regional data in Table C1, and those used in surface sites in Table C2.

As part of CMIP5, a number of 'historical' coupled runs were performed, forced by variations in ISR, and observations of atmospheric composition and land-use changes (Taylor et al., 2012), from at least 1860–2005, which we use here at their native resolution. We select models by data availability: we restrict our analysis to models where up- and down- welling, short- and longwave radiation fluxes are available, in both all- and clear-skies (Appendix D, Table D1). A sub-set of these models also provide AOD at 550nm, indicated in the table. As well as the coupled model runs, we use simulations from AMIP (Gates, 1992; Taylor et al., 2012), which use observed SSTs and sea-ice as boundary conditions for atmosphere-only simulations.

4.3.2 Methods

We first examine the range of the mean annual cycles of radiative variables, TCWV and AOD from the reference data sets. We then evaluate the ability of the CMIP5 GCMs to simulate these mean annual cycles. GCMs such as those used in CMIP5 are not intended to exactly replicate the state of the atmosphere at a specific time or place, rather the general patterns of variability. Therefore, we examine the average seasonal cycles over up to 15 years. We calculate the average seasonal cycles both integrated over the regions defined in section 4.2, and also at the surface measurement sites.

We use full years for our analysis: for EBAF TOA and Surface, and ERA-I, we use 2001-2015 inclusive, for CMSAF GERB/SEVIRI and SARAH we use 2005-2014 inclusive. Using the overlapping years of 2005–2014 for EBAF TOA and Surface, CMSAF GERB/SEVIRI and SARAH, and ERA-I for the analysis does not significantly alter results. For the surface measurement sites, we use all available data between 1992–2017 inclusive, though the number of individual months used varies significantly depending on the variable and site. However, for each variable and site, the number of data points used in the monthly mean is approximately equal throughout the annual cycle (not shown). For CMIP5 coupled-model and atmosphere-only models we use 1990–2004 inclusive. We define the dry season as October–March inclusive, and the wet season as April–September. While this definition is less appropriate for the coastal region (see the description of the 'little dry season' in sec. 4.2) we apply this definition to all regions to enable a consistent analysis.

Our analysis utilises data from both point measurements (surface sites) and area-averaged (statellite products and CMIP5 output). This requires care when making comparisons. Hakuba et al. (2014) found that the climatological mean DSR from surface stations has a spatial sampling error of 0.1 $\mathrm{Wm}^{-2}$for the Ilorin

and Tamanrasset sites within a 1° grid with respect to co-located gridded data. Moreover, Schwarz et al. (2017) showed that time series of monthly mean DSR from surface sites can be considered representative for an area 100-600km around the sites location. This suggests that the climatological annual cycles of DSR obtained from BSRN sites are reasonably representative of the grid averages of the other reference products. Additionally, we find that the sites have qualitatively similar climatologies to the surrounding regions (see sec.4.4.1 and 4.5.1), which further supports our analysis approach.

4.4 Results: all-sky radiation fluxes

In this section, we first evaluate the agreement of the reference products in order to understand the spread in observational uncertainty in all-sky TOA and surface radiation flux. For the surface radiation fluxes we evaluate both the surface sites and also the wider regions. Second, we place the CMIP5 model outputs in the context of the references, to characterise key differences in the multi-model mean and range. Finally, we interpret these differences with respect to monsoon timing and progression.

4.4.1 Observational range in all-sky TOA and surface radiation fluxes

At the TOA, we use the EBAF and GERB/SEVIRI products as our primary references. We find that for all-sky monthly radiation fluxes, the annual averages of the satellite products agree to within 4 Wm^{-2} in all-sky RSR and OLR over west Africa and individual regions (Fig. 4.2a-h). We take the positive direction of OLR to be radiation to space. When analysed over all west Africa, the differences

between GERB/SEVIRI and EBAF RSR are larger in the dry season (October –March, 1.0 Wm^{-2}, Table 4.1) than in the wet season (April – September, -0.2 Wm^{-2}). However, the largest differences are in the wet season in the coastal region (-3.2 Wm^{-2}).

For the surface radiation fluxes, our primary reference comes from the BSRN surface measurement sites. We validate the other reference products (EBAF and SARAH) at the nearest gridpoint to the site. At Tamanrasset, the annual average of all-sky DSR from EBAF agrees within 5 Wm^{-2} to the BSRN value of 263 Wm^{-2}, with the annual average from SARAH markedly higher at 276 Wm^{-2} (Fig. 4.3a). There is a less consistent picture at Ilorin (Fig. 4.3b), though the annual mean from EBAF is within 6 Wm^{-2} of the BSRN value of 203 Wm^{-2}, with the annual average from SARAH again larger at 221 Wm^{-2}. However, due to the limited data available from Ilorin, this may not be an accurate representation of the annual surface insolation cycle. The annual cycle in all-sky DSR at Tamanrasset is largely similar in shape to that of the wider Saharan region (correlation coefficient r^2 =0.95 between BSRN DSR, Fig. 4.3a, and EBAF in the Saharan region, Fig. 4.2l), as is Ilorin to the coastal region (r^2 = 0.77 between BSRN DSR, Fig. 4.3b , and EBAF in the coastal region, Fig. 4.2k). Over the wider regions (Fig. 4.2i-l), we find that the EBAF all-sky DSR product is consistently lower than the other products, with the annual average over all west Africa 13.8 Wm^{-2} more in SARAH than in EBAF (Table 4.1). This difference is highest in the coastal dry season (25.1 Wm^{-2}), and lowest in the Saharan dry season (7.6 Wm^{-2}).

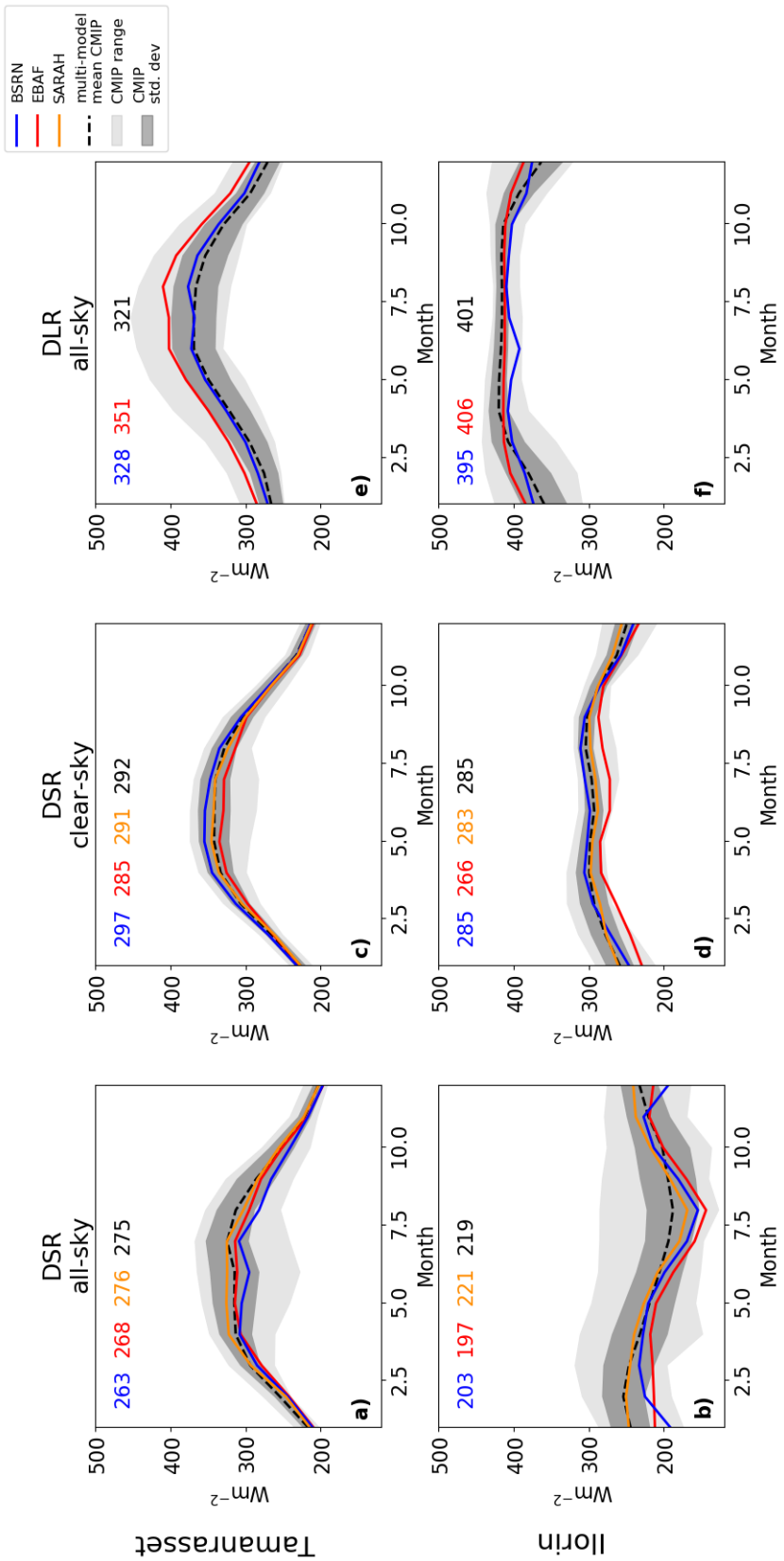

Figure 4.3: As Fig. 4.2, but for BSRN sites Tamanrasset and Ilorin. Data from BSRN, EBAF, SARAH and CMIP models. Inset numbers indicate annual average of climatology, with colours corresponding to data sets as marked in legend.

Table 4.1: All- and clear-sky annual, dry (October–March) and wet (April–September) seasonal differences in GERB/SEVIRI - EBAF TOA for RSR and OLR and CMSAF SARAH - EBAF Surface for DSR (normal print); CMIP5 coupled model multi-model - EBAF mean for OLR, RSR, DSR and DLR (bold print); CMIP5 coupled model range (italics). The positive direction for OLR is upwards.

Flux	Region	all-sky			clear-sky		
		Annual mean	Dry season mean	Wet season mean	Annual mean	Dry season mean	Wet season mean
RSR	West	0.4	1.0	-0.2			
	Africa	**-0.5**	**-0.1**	**-0.9**	**-0.8**	**-0.1**	**-1.6**
		37.2	*31.5*	*42.9*	*35.2*	*30.3*	*40.1*
	Sahel	0.2	0.8	-0.4			
		-3.8	**-2.3**	**-5.3**	**-3.8**	**-3.1**	**-4.5**
		46.8	*37.9*	*55.6*	*39.2*	*34.8*	*43.7*
	Coastal	-1.4	0.4	-3.2			
		3.1	**6.5**	**-0.3**	**5.5**	**8.6**	**2.3**
		71.4	*57.3*	*85.4*	*34.6*	*32.8*	*36.3*
	Sahara	1.0	1.7	0.4			
		-0.7	**-2.3**	**0.9**	**-2.0**	**-2.6**	**-1.3**
		45.9	*38.8*	*52.9*	*46.7*	*38.2*	*55.1*
OLR	West	-2.6	-2.4	-2.8			
	Africa	**4.6**	**5.0**	**4.2**	**-1.8**	**-1.2**	**-2.3**
		34.0	*23.8*	*44.3*	*26.1*	*18.6*	*33.7*
	Sahel	-1.4	-0.8	-1.9			
		7.3	**4.9**	**9.6**	**-1.1**	**-1.0**	**-1.1**
		44.3	*30.9*	*57.7*	*29.7*	*20.1*	*39.3*
	Coastal	-3.1	-2.5	-3.8			
		9.1	**16.9**	**1.4**	**-1.0**	**1.0**	**-3.0**
		56.9	*49.6*	*64.2*	*23.4*	*23.8*	*23.1*

	Sahara	-3.4	-3.9	-2.9			
		-1.0	**-0.6**	**-1.3**	**-3.1**	**-2.7**	**-3.5**
		39.1	*25.0*	*53.3*	*28.4*	*17.0*	*39.7*
DSR	West	13.8	13.7	13.8	10.3	9.4	11.1
	Africa	**9.3**	**8.9**	**9.7**	**8.7**	**6.7**	**10.7**
		71.5	*54.0*	*89.0*	*42.2*	*35.8*	*48.7*
	Sahel	14.7	16.4	13.0	11.0	11.8	10.2
		11.5	**11.5**	**11.5**	**9.7**	**9.0**	**10.4**
		91.1	*64.1*	*118.0*	*54.5*	*46.5*	*62.5*
	Coastal	20.7	25.1	16.3	15.0	19.7	10.2
		14.1	**15.6**	**12.4**	**15.0**	**15.9**	**14.2**
		127.2	*113.3*	*141.0*	*50.1*	*56.6*	*43.6*
	Sahara	11.4	7.6	15.1	8.8	4.3	13.2
		7.2	**5.5**	**8.9**	**6.6**	**3.0**	**10.2**
		66.2	*40.1*	*92.4*	*42.3*	*29.9*	*54.6*
DLR	West						
	Africa	**-16.6**	**-18.5**	**-14.6**	**-10.1**	**-10.7**	**-9.4**
		72.6	*72.0*	*73.3*	*61.2*	*61.0*	*61.3*
	Sahel						
		-17.9	**-22.5**	**-13.3**	**-9.3**	**-11.7**	**-6.9**
		81.7	*77.6*	*85.7*	*70.9*	*68.1*	*73.7*
	Coastal						
		-5.8	**-14.4**	**2.8**	**-4.0**	**-10.3**	**2.3**
		63.2	*82.1*	*44.2*	*50.0*	*68.6*	*31.5*
	Sahara						
		-21.0	**-16.9**	**-25.1**	**-14.4**	**-10.8**	**-18.0**
		75.1	*62.8*	*87.4*	*60.4*	*50.4*	*70.4*

The downwelling longwave radiation flux in Tamanrasset from BSRN and EBAF have a similar annual cycle (correlation coefficient $r^2 = 0.97$, Fig. 4.3e), with an annual average of 328 and 351 Wm^{-2}, respectively, with the largest differences in the wet season. Differences between reference products are smaller in Ilorin (Fig. 4.3f), with annual averages of 406 Wm^{-2} and 395 Wm^{-2} for EBAF and BSRN, respectively, which are largely in line with the wider coastal region (407 Wm^{-2}, Fig. 4.2o). However, at both Tamanrasset and Ilorin it is notable that EBAF has consistently higher values of DLR than BSRN, suggesting that EBAF may be overestimating the DLR in this region.

4.4.2 All-sky TOA and surface radiation fluxes in the CMIP5 ensemble

We now examine the coupled CMIP5 models all-sky output in the context of the reference data outlined above. At the TOA, we find that the multi-model mean all-sky RSR from the coupled CMIP5 models agrees with EBAF to within 4 Wm^{-2} in the annual mean, slightly larger than the 1–2 Wm^{-2} difference between CMSAF GERB/SEVIRI and EBAF (Fig. 4.2a-d). However, there is a large spread across the models, reaching $\sim$70 Wm^{-2} in the annual mean (Table 4.1). In the longwave, the multi-model mean all-sky OLR agrees with the EBAF values to within 9 Wm^{-2} in the annual mean, again larger than the $\sim$3 Wm^{-2} between CMSAF GERB/SEVIRI and EBAF (Fig. 4.2e-h).

There are distinct contrasts in all-sky OLR between regions and seasons in the CMIP5 models with respect to EBAF, which we interpret as a consequence of the timing and progression of the WAM in the models. Two aspects of the EBAF and CMIP5 model differences in particular point to this. First, CMIP5 mean differences with respect to EBAF are larger for all-sky OLR in the coastal dry season (16.9 Wm^{-2}, Table 4.1, Fig. 4.2g) and Sahelian wet season (9.6 Wm^{-2},

Table 4.1, Fig. 4.2f). Second, there is a distinct difference in the shape of the seasonal cycle in all-sky OLR between the reference products and CMIP5 models over the coastal region. EBAF and GERB/SEVIRI show an increase in the later part of the wet season, approximately July/August, which is not captured by the CMIP5 multi-model mean. Both of these aspects suggest that the OLR-reducing deep convective clouds associated with the monsoon in the models reach the coastal region later in the year than observed. Additionally, the deepest convective clouds do not progress over the coastal region and into the Sahel, leading to the coastal 'little dry season', as they do in radiation observations, consistent with previous research (e.g. Roehrig et al., 2013; Dunning et al., 2017). It should be noted, however, that the coastal region, as defined here, is defined as spanning 5° in latitude. Depending on the model resolution, there may not be many gridpoints within this region, and the number of land/ocean may differ model to model. This may account for some of the model range observed.

Our interpretation is supported by two derived products in the Sahel and coastal region, longwave atmospheric cloud radiative effect ($\mathrm{CRE_{LW}}$, Fig. 4.4b-c) and longwave cloud radiative forcing at the TOA ($\mathrm{CRF_{LW}^{TOA}}$, Fig. 4.4f-g). Here, we focus only on the longwave as the effects of the monsoon are more clearly seen. By removing the clear-sky values (CS) from the all-sky (AS) radiative fluxes, $\mathrm{CRF_{LW}^{TOA}}$ represents the radiative effect of the presence of clouds on the TOA longwave fluxes, as given by equation 1.5

As the presence of clouds reduces OLR, this is a negative quantity. The difference between the net longwave fluxes entering and leaving the atmospheric column in the all-sky and clear-sky defines the longwave atmospheric cloud radiative effect, $\mathrm{CRE_{LW}}$:

$$\mathrm{CRE_{LW}} = (-\mathrm{OLR_{LW}^{AS}} - \mathrm{DLR_{LW}^{AS}} + \mathrm{ULR_{LW}^{AS}}) - (-\mathrm{OLR_{LW}^{CS}} - \mathrm{DLR_{LW}^{CS}} + \mathrm{ULR_{LW}^{CS}}) \tag{4.1}$$

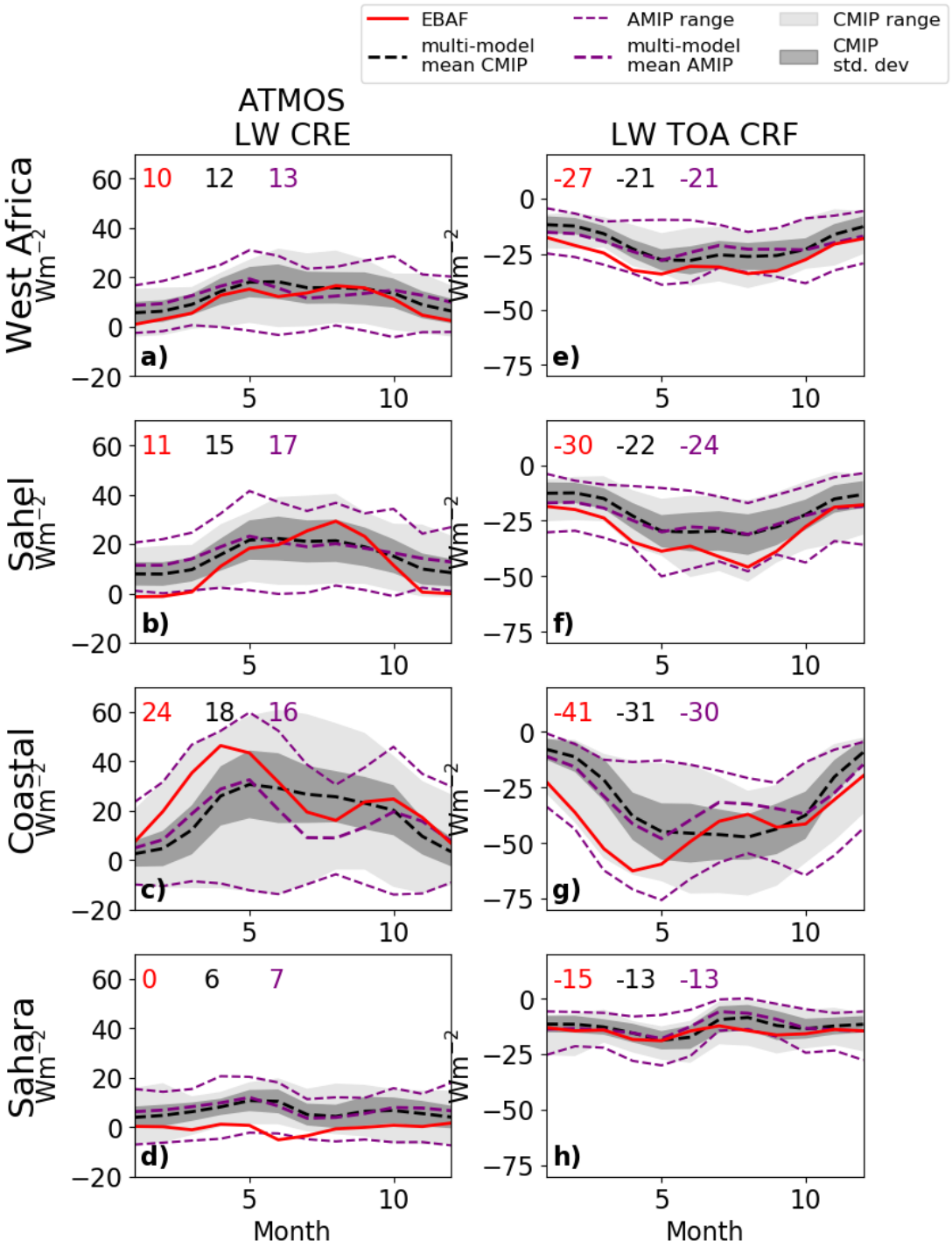

Figure 4.4: As Fig. 4.2, but for longwave cloud radiative effect (eq. 4.1), longwave cloud radiative forcing at the TOA (eq. 1.5).

This gives a measure of the change in longwave radiation entering and leaving the atmospheric column due to clouds, where a positive CRE indicates that the presence of clouds warms the atmosphere. For a more detailed discussion of these derived variables, see Miller et al. (2012).

As with the all-sky OLR, the 'little dry season' in the coastal regions is evident in the CRE_{LW} from EBAF (Fig. 4.4c), with two distinct peaks in May and October as the main part of the monsoon passes overhead, but not in the CMIP5 models. Similarly, the CRE_{LW} and CRF_{LW}^{TOA} in the Sahelian wet season (Fig. 4.4b and f) show a distinctly different seasonal cycle between the CMIP5 models and EBAF. In August, EBAF has a maximum in CRE_{LW} and a minimum in CRF_{LW}^{TOA} which are not captured by the CMIP5 models. This supports the hypothesis that the clouds which pass over the coastal region into the Sahel at the northern most extent of the monsoon are not as well developed, and thus reduce OLR to a lesser extent, in the coupled CMIP5 models than in the references. We note that models and observations define 'clear-sky' in different ways: while CERES classifies a footprint as clear-sky if cloud fraction, as determined by MODIS, is $\leq$0.1 (Loeb et al., 2018), models compute the flux as if there were no clouds present. This sampling error can lead to a dry bias in satellite estimates of clear-sky radiative fluxes, which in turn impacts CRF_{LW}^{TOA} , especially over convective regions (Allan and Ringer, 2003; Sohn et al., 2006). We now examine the ability of the coupled CMIP5 models to simulate the mean seasonal cycle of the all-sky surface fluxes. While the regional CMIP5 multi-model mean lies within the range of the reference products for all-sky DSR, the standard deviation of CMIP5 values is generally outside this range, especially in the coastal region and Sahelian wet season (Fig. 4.2i-l). The seasonal and regional contrasts in the range of CMIP5 models suggests that the monsoon effect on the radiation fluxes may also be the cause of this spread. At Tamanrasset, DLR in the CMIP5 models is lower than the direct observations from BSRN (Fig. 4.3e), a typical feature of GCMs (Wild

et al., 1995, 2013, 2015). Furthermore, over the wider regions the multi-model annual mean is consistently smaller than the EBAF product (Fig. 4.2m-p).

4.4.3 Effect of imposed SSTs

As discussed in Section 4.1, coupled models are known to suffer from SST biases, which have been linked to biases in the WAM (Roehrig et al., 2013; Dunning et al., 2017). To test to what extent the differences in radiative variables discussed above can be attributed to the SST biases in coupled models, we repeat the analysis with model output from the atmosphere-only experiments, AMIP, which use observed SSTs.

We observe closer agreement between AMIP models with EBAF and GERB/SEVIRI in some of the identified variables. For example, the shape of the seasonal cycle in all-sky OLR, atmospheric $\mathrm{CRE_{LW}}$ and $\mathrm{CRF_{LW}^{TOA}}$ in the coastal region show considerable improvement (Fig. 4.2g, Fig. 4.4c and Fig. 4.4g). However, differences between EBAF and the AMIP multi-model mean remain, especially in the coastal region, with annual mean differences remaining high (10 $\mathrm{Wm^{-2}}$), and the decrease in OLR in the multi-model mean still lagging that in EBAF by 1-2 months (Fig. 4.2g). There is also little change from the coupled model results in the Sahel (Fig. 4.4b and Fig. 4.4f). This implies that the clouds associated with the monsoon in the AMIP simulations do not have as strong an effect in the longwave as in EBAF in the early part of the monsoon, but the cloudiest part of the monsoon does progress over the coastal region into the Sahel leading to the coastal 'little dry season'. However, the limited improvements over the Sahel suggest that this progression does not extend as far northwards as that indicated by EBAF. Negligible differences are seen between the multi-model mean values of DSR and DLR for the AMIP and coupled model results (Fig. 4.2i-p). With the exception of the coastal wet season (Fig. 4.5c), we also see negligible

differences in regional TCWV between using coupled and atmosphere-only models (Figs. 4.5b-d), indicating that the dry bias seen in many CMIP5 models is not linked to SST biases.

Comparing the model range in all-sky radiative fluxes (purple dashed lines compared to shading, Fig. 4.2) in AMIP and the coupled models, we find there are negligible differences at the TOA in most regions, with the exception of the all-sky OLR in the coastal region, where the range reflects the 'little dry season' increase in July–August. At the surface, the all-sky DSR and DLR AMIP range is reduced, especially the DSR in the Sahara. There is also a reduction in AMIP model range in $\mathrm{CRE_{LW}}$ and $\mathrm{CRF_{LW}^{TOA}}$ with respect to the coupled models (Fig. 4.4). Due to the influence of SSTs on interannual variability in monsoon progression, a reduced range in the models is expected.

4.5 Results: Surface clear-sky fluxes, aerosols and water vapour

In this section, we focus on the effect of two factors, AOD and TCWV, on the downwelling clear-sky fluxes at the surface, DSR and DLR. As discussed previously, clear-sky DSR and DLR have long been noted as having consistent biases in GCMs with respect to surface measurement stations (Wild et al., 1995, 2013; Rutan et al., 2015). We begin discussing the range in clear-sky surface fluxes, AOD and TCWV from our reference products. We then examine how the CMIP5 models perform relative to this range, particularly by interpreting differences in surface clear-sky fluxes with respect to in differences in AOD and TCWV. Finally, we extend this analysis by examining how differences between EBAF/SYN1deg and CMIP5 downwelling fluxes relate to differences in AOD and TCWV in individual models.

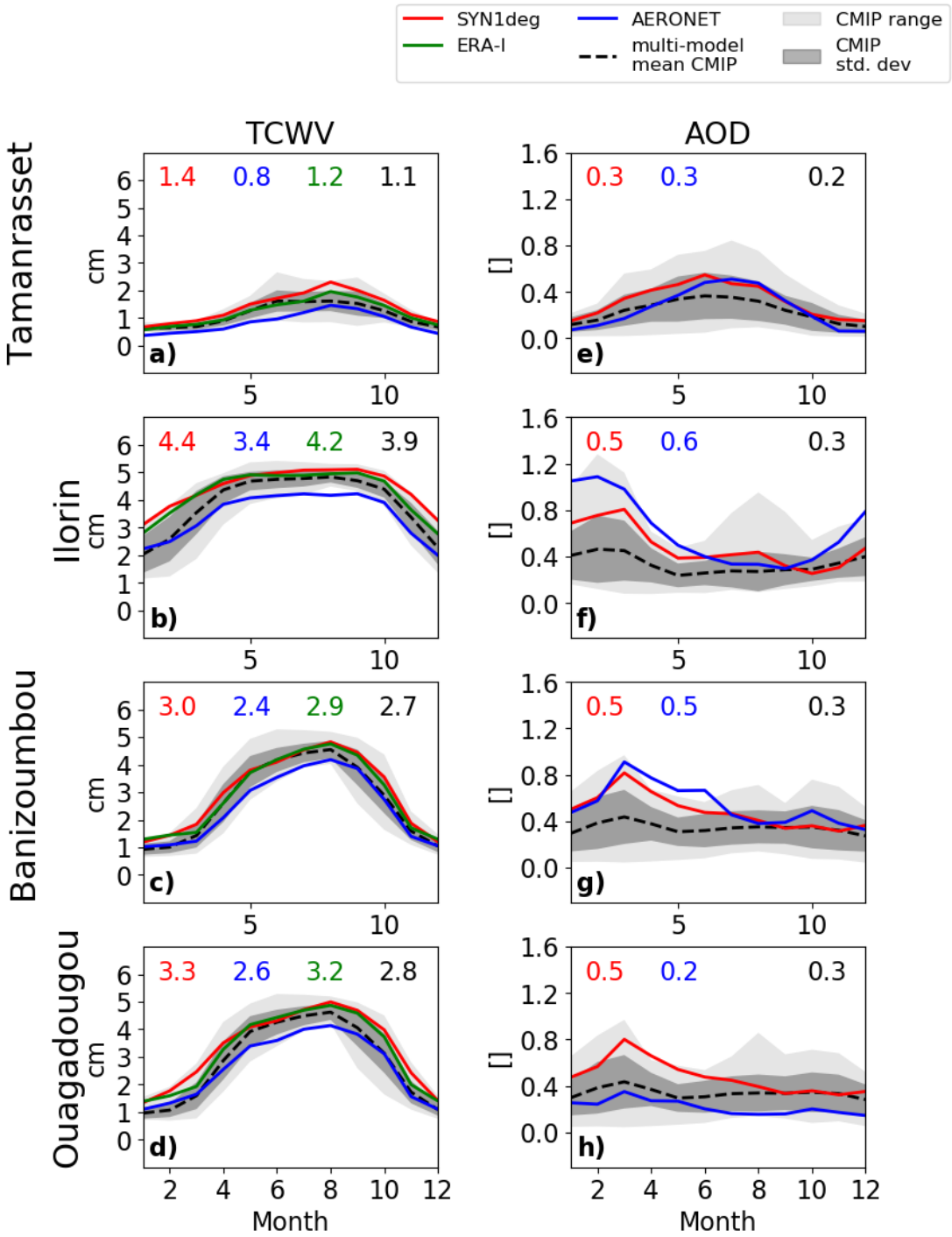

Figure 4.5: Regional annual cycles (as described in sec 4.3) from SYN1deg, CMIP5, AMIP and ERA-I. Dark grey shading indicates CMIP5 standard deviation, light grey shading indicates CMIP5 range, and thin purple lines indicate AMIP range (a-d only); thin magenta lines indicate range of models using an interactive aerosol scheme (e-h only). Inset numbers indicate annual average of climatology, with colours corresponding to data sets as marked in legend.

4.5.1 Observational range in clear-sky surface fluxes, water vapour and aerosol

In the shortwave, we see that SARAH has consistently higher DSR than EBAF under clear-sky conditions across all regions (Fig. 4.7a-d). Given that we use regional monthly means over ∼15 years, and the monthly 1° x 1° uncertainty in SARAH and EBAF clear-sky DSR are 5 Wm^{-2} (Pfeifroth et al., 2017) and 6 Wm^{-2} (Kato et al., 2018), respectively, these differences are outwith the observational uncertainties. These differeces are also consistent with the observations at Ilorin and Tamanrasset (Fig. 4.3c-d) which show that DSR from SARAH more closely fits with the seasonal cycle as inferred from the BSRN data than EBAF.

Next, we examine the TCWV and AOD fields in the reference products, using output from ERA-I and observations from AERONET as our primary reference, respectively. TCWV retrievals from AERONET are consistently lower than the other reference products (Fig. 4.6a-d), consistent with evidence that AERONET TCWV measurements suffer from a dry bias with respect to the more accurate, but not yet widely available, GPS and radiometry methods (Pérez-Ramírez et al., 2014). Using GPS as a standard, Kishore et al. (2011) find that among model outputs ERA-I, which assimilates water vapour retrievals from satellite instruments (Dee et al., 2011), performs well in its representation of TCWV, suggesting that this may be a better standard to use to evaluate CMIP5. We therefore use SYN1deg and ERA-I as our primary references for TCWV in the following section, rather than those from AERONET. SYN1deg and ERA-I have differences in annual average water vapour ≤0.3 cm, likely because the former is also based on reanalyses, albeit from a different system (sec. 4.3). We find similar (correlation coefficients $r^2 > 0.94$) ERA-I TCWV annual cycles in Tamanrasset,

Ilorin, Banizoumbou and Ouagadougou (Fig. 4.6a-d) as in the corresponding wider regions (Fig. 4.5a-d).

AOD is also similar at the AERONET sites to their wider regions (compare Fig. 4.6e to Fig. 4.5h, $r^2 = 0.74$; Fig. 4.6f to Fig. 4.5g, $r^2 = 0.86$; and Figs. 4.6g-h to Fig. 4.5f), $r^2 = 0.72$ and $r^2 = 0.43$). AOD at Tamanrasset from AERONET has a slightly later peak in July than the June peak of SYN1deg (Fig. 4.6e). In Ouagadougou (Fig. 4.6h), AOD from AERONET is much lower than that in Banizoumbou (Fig. 4.6g) and is the only site where SYN1deg has a consistent higher aerosol loading than AERONET. This is indicative of the high spatial and temporal variability in AOD: despite the relative proximity of Banizoumbou and Ouagadougou, the AERONET values are different by a factor of $\sim$2.

4.5.2 Surface radiation fluxes, water vapour and aerosol in the CMIP5 ensemble

In general, the CMIP5 models have higher values of DSR than EBAF under clear-sky conditions (Fig. 4.7a-d). The CMIP5 models also show a large range in the wet season, particularly in the Sahel (62.5 Wm^{-2}, Table 4.1). Despite this, the multi-model mean is within the range given by EBAF and SARAH across the regions (Fig. 4.7a-d) and agrees within 5 Wm^{-2} and 1 Wm^{-2} with the BSRN observation at Tamanrasset and Ilorin, respectively (Fig. 4.3c-d). While there are no clear-sky DLR inferences at the surface sites, we see that EBAF DLR is consistently higher in the regional integrations than the CMIP5 multi-model mean (Fig. 4.7e-h). This difference is highest in the Saharan wet season (-18.0 Wm^{-2}, Table 4.1).

The multi-model mean from CMIP5 has a dry bias with respect to ERA-I both at the sites (Fig. 4.6a-d) and across the wider regions (Fig. 4.5a-d). This is

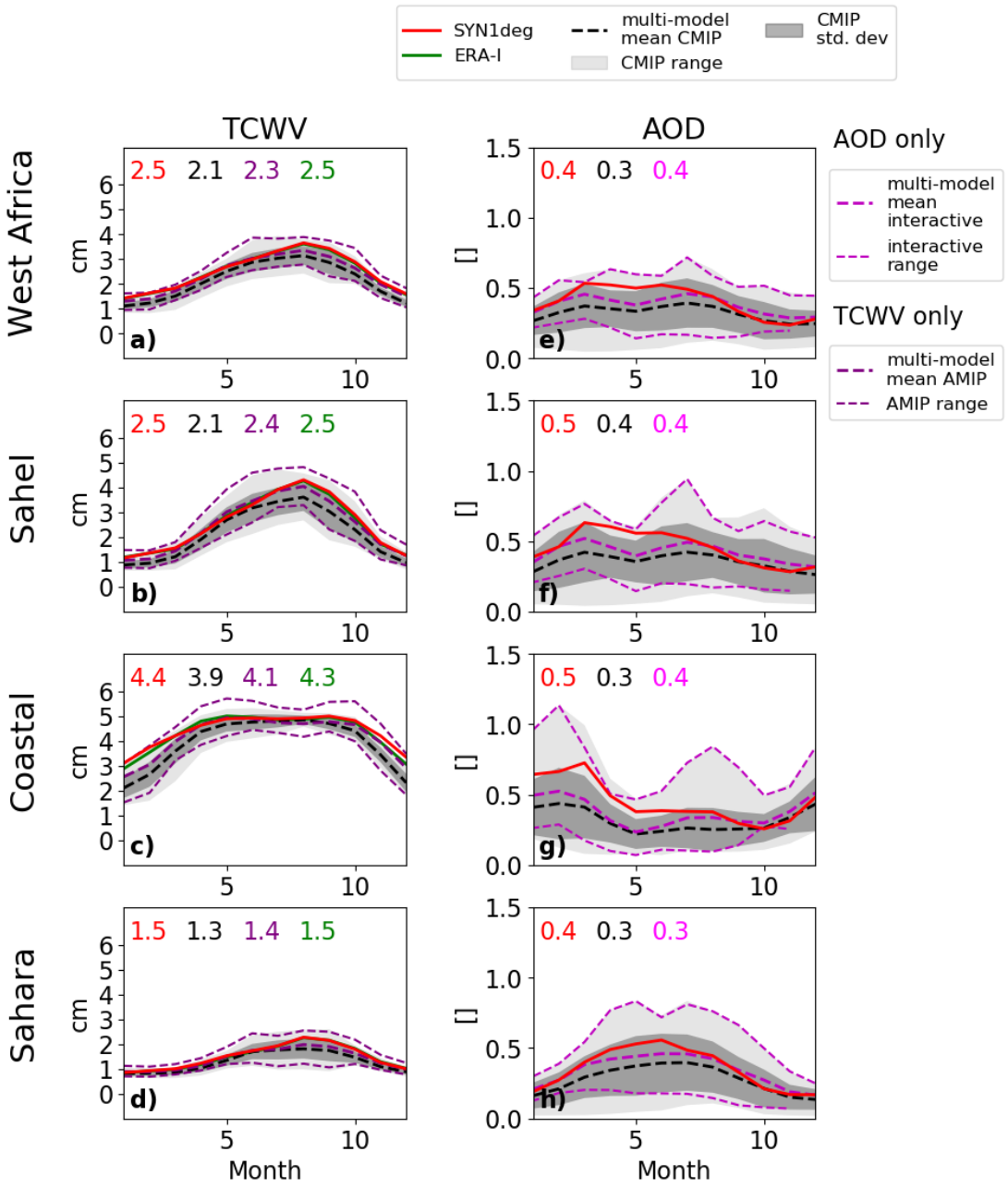

Figure 4.6: Annual cycles (as described in sec. 4.3) of TCWV at AERONET sites Tamanrasset, Ilorin, Banizoumbou and Ouagadougou. Dark grey shading indicates CMIP5 standard deviation, light grey shading indicates CMIP5 range. Inset numbers indicate annual average of climatology, with colours corresponding to data sets as marked in legend.

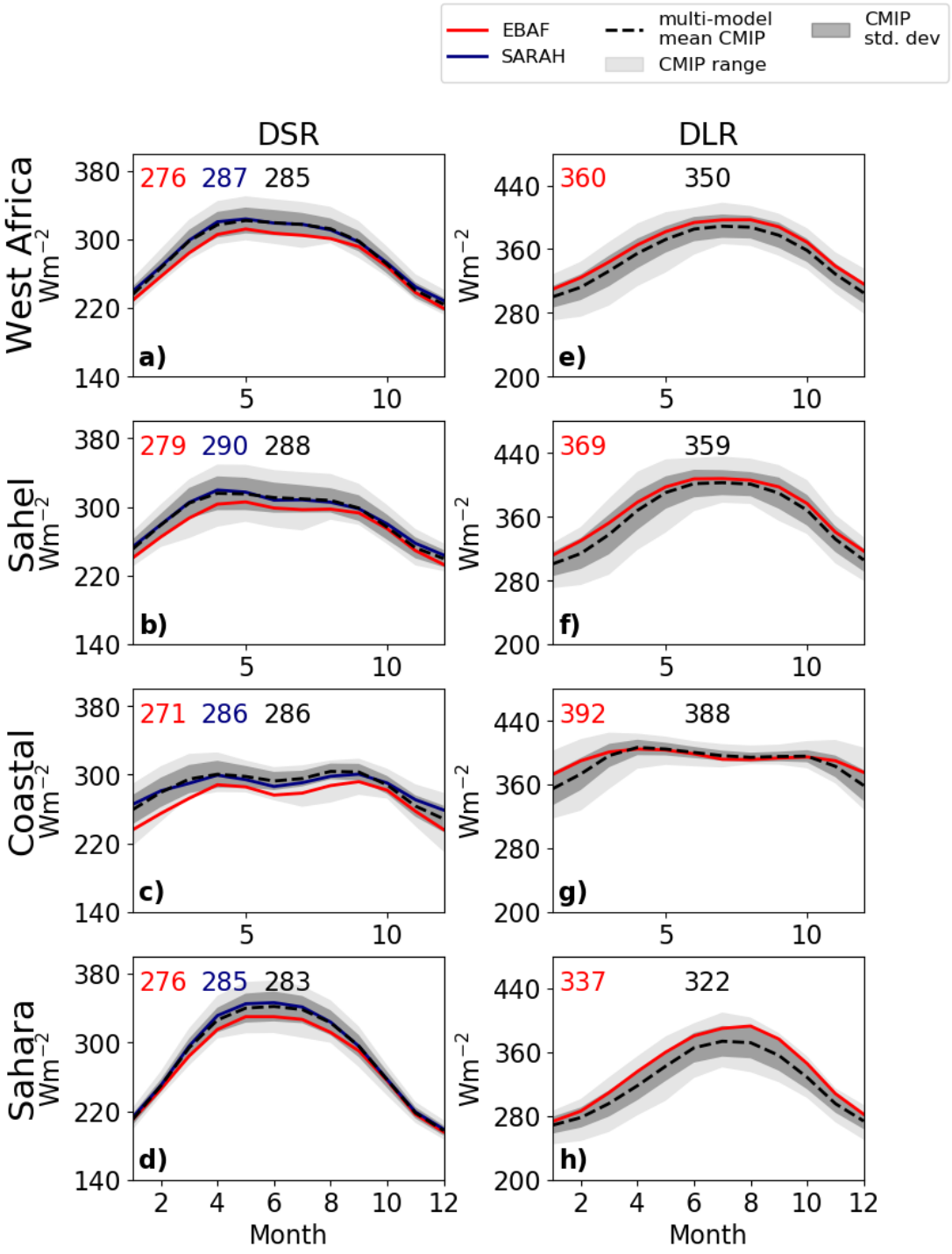

Figure 4.7: As Fig. 4.2, but for surface clear-sky fluxes.

especially the case in the dry season, where the ERA-I and SYN1deg value is outside of the range given by the CMIP5 models. This drier atmosphere in the CMIP5 models is consistent with the higher clear-sky DSR and lower clear-sky DLR with respect to EBAF.

At the sites, the CMIP5 multi-model mean in AOD is generally lower than the AERONET AOD observations (Fig. 4.6e-h). The exception to this is Ouagadougou, where there is a higher aerosol loading. Comparison of Ouagadougou and Banizoumbou in the CMIP5 models and SYN1deg, however, shows that they have very similar AOD at these two sites, indicating that neither has the high spatial variability of the observations. We note that although taking the multi-model mean of the models with an interactive aerosol scheme (Wilcox et al., 2013) at the regional level (Fig. 4.5e-h) increases the AOD by ~ 0.1, thus slightly decreasing the difference to SYN1deg, the range of the models is negligibly different from the full set of coupled models. It is harder to link general patterns in clear-sky surface fluxes with AOD than with TCWV: the CMIP5 models have a very wide range of values with respect to that from SYN1deg (Fig. 4.5e-h), though the multi-model mean is generally lower. Lower atmospheric dust aerosol loading in the CMIP5 models would also result in more solar radiation reaching the surface, and less downwelling longwave radiation.

While some disagreement exists between reference products, and there is a suggestion that EBAF may underestimate the all-sky DSR and clear-sky DLR, we continue our analysis using just the CMIP5 models and EBAF. This is for two reasons: first, in order to evaluate radiation fluxes with respect to other variables, we require self-consistent data sets, such as that provided by EBAF/SYN1deg and CMIP5. Second, while EBAF Surface/SYN1deg is essentially also model output, comparison of the sensitivity to aerosols and water vapour of clear-sky surface fluxes between EBAF and the CMIP5 models is of interest.

4.5.3 Link of clear-sky fluxes to AOD and TCWV

In this section, we aim to address two questions to determine the relative effect of TCWV and AOD on the clear sky downwelling fluxes by examining the CMIP5 models individually. The first is whether models which have a larger discrepancy in AOD or TCWV with respect to EBAF have a larger discrepancy in shortwave radiation absorbed by the atmosphere (Fig. 4.8) or downwelling longwave radiation at the surface (Fig. 4.9). The second is to probe how changes in water vapour and aerosol loading may affect the clear-sky fluxes, and how this might be different in EBAF and the CMIP5 models.

We approach the first of these questions in the following way: we start with calculating the time series of the proportion (in %) of shortwave radiation reaching the surface for each model individually, in each region, by taking the ratio of the DSR and the incident solar radiation at the TOA; next, we calculate the mean of the model - EBAF discrepancy in this proportion over that time period; we then repeat this for AOD and TCWV for each model, to obtain the mean discrepancy with SYN1deg. Figure 4.8a-d shows the CMIP5 mean model - EBAF discrepancy of the percentage of shortwave radiation reaching the surface (DSR/TSI), plotted against the mean model - SYN1deg discprepancy in AOD and TCWV, integrated across the regions. Figure 4.9a-d shows the same for clear-sky downwelling longwave radiation at the surface. We see that, in general, the largest differences in DLR and DSR are in the bottom left quadrant where the models are drier and have lower aerosol loading than SYN1deg. Indeed, as the model positions are the same in Fig. 4.8a-d and Fig. 4.9a-d, we see that some of the models which are considerably more transparent in the shortwave than EBAF (dark red in Fig. 4.8a-d) also have the smallest downwelling longwave radiation values with respect to EBAF (dark blue in Fig. 4.9a-d). We note that over all west Africa and in the coastal region, models with the largest difference in TCWV also have the largest

difference in DLR. Additionally, there are models which have more DLR than EBAF over some regions, in particular the coastal region. These models generally have a small difference in TCWV (±0.2cm) compared to SYN1deg. There is a less clear picture with AOD, though there is also no clear evidence that models with interactive aerosol schemes (marked with diamonds) have smaller differences to EBAF than those using climatologies.

To answer the second question, we extend our analysis to look at the correlations between anomalies in clear-sky DSR and DLR and anomalies in AOD and TCWV (Fig. 4.8e-f and Fig. 4.9e-f). For each model, and for EBAF, we start by calculating the anomaly of the regional mean for each month from the 15-year monthly mean of the variables. We then use a least-squares regression to correlate the anomaly in AOD and TCWV with the anomaly in clear-sky DLR and DSR. The Pearson's r^2 correlation coefficient for each correlation gives a measure for the proportion in variability of the flux anomaly explained by the variability in AOD or TCWV. Figure 4.8e-h show the r^2 correlation coefficient of DSR with AOD, plotted against that from DSR and TCWV. Figure 4.9e-h shows the same but for DLR. On both plots, the correlations within EBAF/SYN1deg are given by crosses, for comparison with the individual models.

We see that, for EBAF, clear-sky DSR has a far higher correlation coefficient with AOD than with TCWV. While some CMIP5 models do show this behaviour, the majority of the CMIP5 models show the opposite: a stronger degree of co-variability between clear-sky DSR and TCWV than between clear-sky DSR and AOD. A number of models with a large difference in the proportion of shortwave radiation reaching the surface (dark red) have a particularly weak correlation with AOD. The differences in sensitivity of clear-sky fluxes to AOD between EBAF and the models in CMIP5 could arise from a number of reasons: a result of the lower variability in AOD in the models; that EBAF uses AOD directly (as given by MATCH and MODIS, see section 4.3) while AOD in GCMs is calculated from

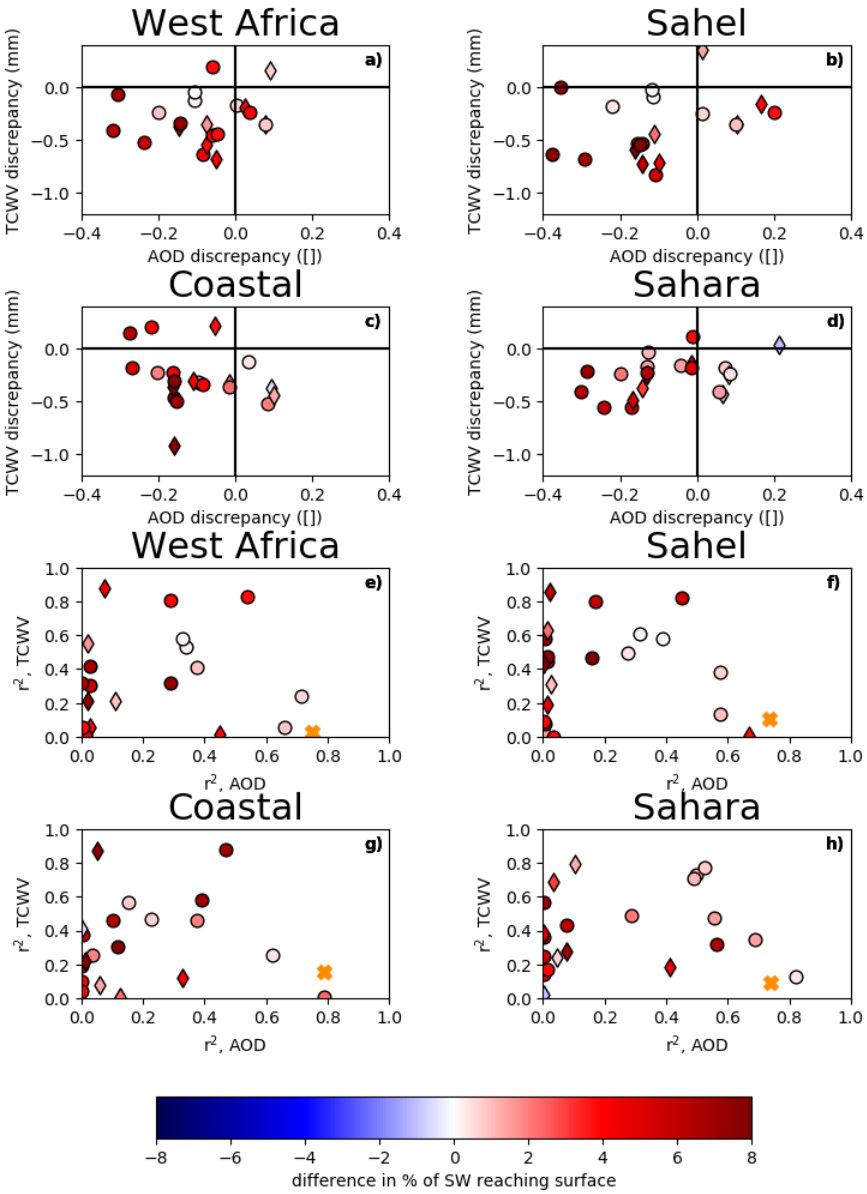

Figure 4.8: Plots a- d: points represent individual CMIP models. Colour scale indicates mean model - EBAF difference in percentage of shortwave radiation reaching the surface from the TOA (DSR/ISR) under clear-sky conditions; x-axis shows mean CMIP model- SYN1deg model difference for AOD; y axis shows mean CMIP5 model - SYN1deg difference for TCWV. Diamonds indicate models using an interactive aerosol scheme, circles models using a climatology. Plots e-f: color scale as above; x-axis indicates the Pearson's r^2 correlation coefficient between deseasonalised percentage of shortwave radiation reaching surface under clear-sky conditions and AOD; y-axis indicates similar correlation but with TCWV; yellow crosses show the position of EBAF/SYN1deg variables.

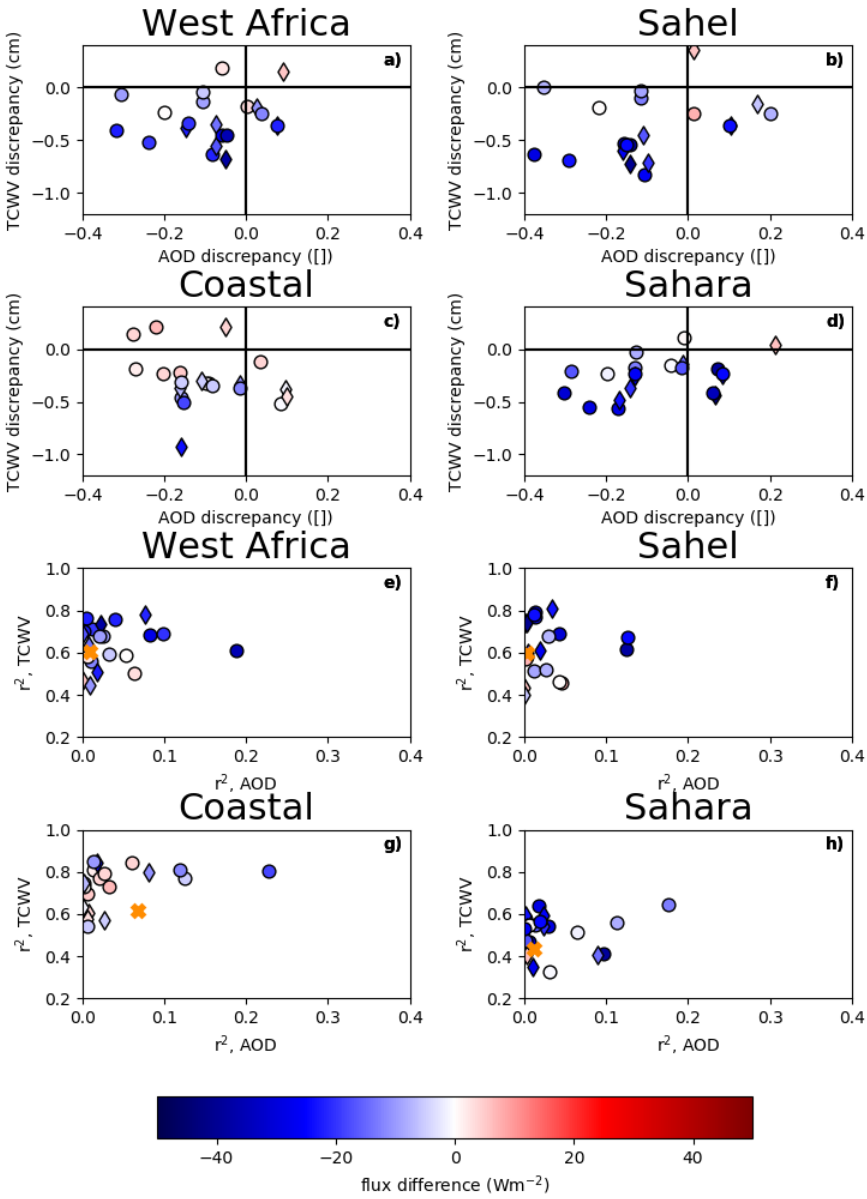

Figure 4.9: As Fig. 4.8, but for clear-sky downwelling longwave radiation.

aerosol properties; horizontal and vertical resolution of the models in comparison to EBAF; or that EBAF uses 18 shortwave channels Rutan et al. (2015), which is larger than for most GCMs (compare with, for example, the six shortwave channels used in the Met Office Hadley Centre models Walters et al. (2017)). This analysis also suggests that the clear-sky DSR is more sensitive to variations in water vapour in most of the CMIP5 models than EBAF. Again, with this measure there is no evidence that models with an interactive aerosol scheme have a larger impact on clear-sky DSR variability than those with a climatology.

For clear-sky DLR in EBAF, there is a very low correlation with AOD and a correlation of $r^2 \sim 0.6$ with TCWV in all regions. The CMIP5 models also have generally have a low correlation coefficient with AOD, and indeed some models do not include the longwave effect of dust aerosol. There is a larger spread in r^2-value for TCWV. Models which co-vary more strongly with water vapour also appear to have less clear-sky DLR with respect to EBAF (dark blue), implying that they are more sensitive to variations in water vapour than EBAF. This is particularly the case over the Sahel, the Sahara and over the wider west African region. The exception to this is the coastal region. Again, this analysis suggests that clear-sky DLR in the majority of CMIP5 models is more sensitive to water vapour than in EBAF.

4.6 Discussion and Conclusions

In this study, we compare TOA and surface fields of all-sky and clear-sky radiation fluxes over west Africa in a variety of reference products to model output from the fifth phase of Coupled Model Intercomparison Project (CMIP5). Through use of multiple reference data sets, including satellite derived products, ERA-Interim reanalysis and surface stations measurements, we are able to evaluate the

CMIP5 models within the context of these references. This also places our primary reference, CERES EBAF, in the context of other reference products, allowing us to proceed with derived radiative products from EBAF (cloud effects and forcing) and auxiliary products relating to water vapour and aerosols, which are only possible with complete, self-consistent data products such as EBAF/SYN1deg, whilst being aware of their limitations. A particular focus is the contrast between different seasons and regions within west Africa. Here, we aimed to address the extent to which the CMIP5 models agree with the range given by the reference products in the TOA and surface radiation fields. Our analysis gives rise to further questions which we address: to what extent can we link coupled model SSTs to monsoon-related differences in radiative variables; and how do AOD and TCWV modulate clear-sky downwelling surface radiation fluxes in both EBAF and the CMIP5 models?

For the first of these questions, we find that differences between the reference data sets are generally smaller than those with respect to many CMIP5 models. Though the multi-model annual mean agrees with the satellite products within 1 Wm^{-2} and 5 Wm^{-2} when averaged over west Africa for RSR and OLR respectively, there is a large range in behaviour of CMIP5 models, particularly in the coastal wet season and Sahelian dry season. At the surface, we find that, in general, the CMIP5 models overestimate the downwelling shortwave radiation, and underestimate the downwelling longwave radiation with respect to EBAF. However, analysis at Tamanrasset and Ilorin suggests that EBAF may underestimate the clear-sky shortwave radiation reaching the surface. At these sites (Fig. 4.3c-d), and also regionally (Fig. 4.7a-d), the CMSAF SARAH clear-sky product agrees more closely with the CMIP5 multi-model mean than with EBAF.

There are a number of aspects in our analysis which link radiation biases to the representation of the west African monsoon. Firstly, from examination of the

coastal region OLR patterns (Fig. 4.2g), there is clear split between the satellite-derived products (GERB/SEVIRI and EBAF) and the models/reanalysis (ERA-I, CMIP5). In particular, the coupled models are generally unable to recreate the 'little dry season', seen in the seasonal evolution of the OLR (Fig. 4.2g) and $\mathrm{CRE_{LW}}$ (Fig. 4.4c). This southward shift in CMIP5 models has been well documented (Roehrig et al., 2013), also in ERA-Interim (Dunning et al., 2016; Hill et al., 2016) though here we focus on the impacts of this on the radiation budget. We use output from atmosphere-only experiments, AMIP, to explore whether differences in radiation fluxes can be attributed to coupled model SSTs. We find that although atmosphere-only models are able to capture the coastal 'little dry season', the advance of the deepest convective clouds still occur later in the year than in the observations, and do not advance as far north into the Sahel. This is consistent with Hill et al. (2016), who note the overestimation of OLR in the Sahel in AMIP with respect to CERES products, indicating that although the southward shift is reduced, it is not limited to coupled models. Also in the shortwave, coastal low-level clouds associated with the monsoon in AMIP models have been linked to a reduction in shortwave radiation reaching the surface (Hannak et al., 2017). This suggests that factors other than the SST biases are causing differences in the representation of the WAM which lead to radiation biases.

A limitation of this study is the relatively short period of observations with respect to known interannual variability in the west African monsoon. However, using an ensemble of models for the multi-model mean reduces the impact of this. Comparisons to AMIP experiments with observed SSTs show little reduction in TOA radiation fluxes, though larger reductions in model range are observed in the surface fluxes, as well as atmospheric column quantities $\mathrm{CRE_{LW}}$ and $\mathrm{CRF_{LW}^{TOA}}$.

There are indications of other sources of radiation differences not linked to coupled model SST, especially on the downwelling surface fluxes. Our analysis of the

clear-sky dependencies on TCWV and AOD show that there are clear differences between EBAF/SYN1deg and the CMIP5 models. Most models have a drier atmosphere, with lower aerosol loading, than EBAF, and we link this to both lower clear-sky DLR and higher clear-sky DSR, and find some evidence that in some models these effects may cancel each other. Additionally, we find that water vapour in almost all the CMIP5 models contributes more to the variability in clear-sky DSR than in EBAF, but AOD contributes less. This suggests that, in the shortwave, aerosols do not modulate the atmospheric absorptivity as strongly as in EBAF, and water vapour has a larger effect. The picture is less clear in the longwave, with aerosols having little effect, but there is some evidence that models which have a larger difference in clear-sky DLR with respect to EBAF are most affected by water vapour. This implies the GCMs and EBAF have different sensitivities to water vapour. The sensitivity of clear-sky DLR to aerosol optical depth is also not clear, and closer study of in situ observations with co-incident measurements of AOD are required to better understand this both in the GCMs and EBAF.

There are a number of questions raised by this analysis, particularly about the sensitivity of surface radiation fluxes in GCMs to variations in water vapour and aerosols. The regional analysis here uses large area integrations, and there is currently insufficient co-incident radiation and aerosol and water vapour profiles data in west Africa to properly analyse whether EBAF is an appropriate reference to use over larger regions. Use of more accurate water vapour retrievals from, for example, GPS, could improve confidence in the co-variance of radiation fluxes with water vapour. However, such measurements are scarce, particularly those which are measured simultaneously with radiative and aerosol properties. Another aspect which could provide insight would be to directly contrast radiative transfer codes of GCMs and EBAF. Additionally, examination of these fields in regions

other than west Africa, where aerosol loadings and origin are different, would be an interesting contrast.

In summary, we find that all-sky radiative biases in CMIP5 GCMs are linked to the biases in coupled-model SSTs, via the subsequent misrepresentation of the west African monsoon. However, even with atmosphere-only versions of these GCMs that used fixed SSTs we find some indications that the northwards extent of the monsoon, as measured by OLR, remains too far south. We also find that many of the CMIP5 models show contrasting sensitivities to variations in atmospheric water vapour and aerosol than shown by the EBAF satellite-observed data products.

Acknowledgements

This study made use of data from a number of sources. I thank the Emilio Cuevas-Agullo, Rachel Pinker, Didier Tanre and Jean Louis Rajot for their effort in establishing and maintaining the Tamanrasset, Ilorin, Banizoumbou and Ouagadougou sites. Additionally, the work performed was done using data from EUMETSATs Satellite Application Facility on Climate Monitoring (CM SAF). I also acknowledge the World Climate Research Programme's Working Group on Coupled Modelling, which is responsible for CMIP, and I thank the climate modeling groups (listed in Table D1 of this paper) for producing and making available their model output. For CMIP the U.S. Department of Energy's Program for Climate Model Diagnosis and Intercomparison provides coordinating support and led development of software infrastructure in partnership with the Global Organization for Earth System Science Portals. I would like to thank Christoph Schär, Martin Wild, Doris Folini and the rest of the research group at the Institute for Atmosphere and Climate, ETH Zürich, for hosting me for this study, and the E3 DTP Overseas Research Travel Fund for financial support.

Appendices

C Reference data

Table C1: Data used in regional analysis. EBAF, SYN1deg and ERA-I data from 2001–2015; CMSAF GERB/SEVIRI and SARAH data from 2005–2014; and CMIP5 data from 1990–2004. The number in the table indicates how many individual months were used in calculation of annual cycle. Regions are defined in sec. 4.2 and marked in Fig. 4.1.

	TOA				**Surface**				**Atmosphere**	
Data	**RSR**		**OLR**		**DSR**		**DLR**		**TCWV**	**AOD**
	AS	CS	AS	CS	AS	CS	AS	CS		
EBAF	180	180	180	180	180	180	180	180		
SYN1deg									180	180
GERB/ SEVIRI	120		120							
SARAH					120	120				
ERA-I									180	
CMIP5	180	180	180	180	180	180	180	180	180	180

Table C2: Data used for site analysis. EBAF, SYN1deg and ERA-I data from 2001–2015; CMSAF GERB/SEVIRI and SARAH data from 2005–2014; CMIP5 data from 1990–2004; and BSRN/AERONET data taken from all available between 1992–2017. The number in the table indicates how many individual months were used in calculation of annual cycle. Sites are described in sec. 4.3 and marked in Fig. 4.1.

	Tamanrasset					Ilorin				
Data	DSR		DLR	TCWV	AOD	DSR		DLR	TCWV	AOD
	AS	CS	AS			AS	CS	AS		
BSRN	177	183	183			73	88	59		
AERO.				72	48				171	171
EBAF	180	180	180			180	180	180		
SYN1deg				180	180				180	180
SARAH	120	120				120	120			
ERA-I				180					180	
CMIP5	180	180	180	180	180	180	180	180	180	180

	Banizoumbou		Ouagadougou	
	TCWV	AOD	TCWV	AOD
BSRN				
AERO.	150	210	57	216
EBAF				
SYN1deg	180	180	180	180
SARAH				
ERA-I	180		180	
CMIP5	180	180	180	180

D CMIP5 models

Table D1: CMIP5 models used, with resolution as longitude x latitude. Model name in italics indicates aerosol optical depth is available, * indicates aerosol scheme is interactive. Bold font indicates atmosphere-only version used as well as coupled version, bold with † indicates atmosphere-only model, with no coupled version. Table based on that from Wild et al. (2015)

Modelling group	**Model**	**Resolution**
Commonwealth Scientific and Industrial Research Organisation	***ACCESS1-0***	1.88° x 1.25°
Bureau of Meteorology, Australia	***ACCESS1-3***	1.88° x 1.24°
Beijing Climate Center, China Meteorological Administration	**BCC-CSM1-1**	2.81° x 2.81°
	BCC-CSM1-1-m	1.13° x 1.13°
College of Global Change and Earth System Science Beijing Normal University, China	***BNU-ESM***	2.81° x 2.81°
Canadian Centre for Climate Modelling and Analysis, Canada	CanESM2	2.81° x 2.81°
	CamAM4†	2.81° x 2.81°
National Center for Atmospheric Research, USA	**CCSM4**	1.25° x 0.94°
NSF-DOE-NCAR, USA	CESM1-BGC	1.25° x 0.94°
	CESM1-FASTCHEM	1.25° x 0.94°
	CESM1-WACCM	2.5° x 1.88°
	CESM1-CAM5†	1.25° x 0.94°

Australian Commonwealth Scientific and Industrial Research Organization, Australia	***CSIRO-Mk3-6-0****	1.88° x 1.88°
LASG, Institute of Atmospheric Physics, Chinese Academy of Sciences, Tsinghua University	***FGOALS-s2***	2.82° x 1.67°
NOAA Geophysical Fluid Dynamics Laboratory, USA	***GFDL-CM3****	2.50° x 2.00°
	GFDL-ESM2G	2.50° x 2.00°
	GFDL-ESM2M	2.50° x 2.00°
	GFDL-HIRAM-C360†	0.31° x 0.25°
	GFDL-HIRAM-C180†	0.62° x 0.5°
NASA Goddard Institute for Space Studies, USA	GISS-E2-H-CC	2.50° x 2.00°
	GISS-E2-H	2.50° x 2.00°
	GISS-E2-R-CC	2.50° x 2.00°
	GISS-E2-R	2.50° x 2.00°
Met Office Hadley Centre, United Kingdom	*HadGEM2-CC*	1.88° x 1.24°
	*HadGEM2-ES**	1.88° x 1.24°
	HadGEM2-A†	1.88° x 1.24°
Institute for Numerical Mathematics, Russia	**INMCM4**	2.00° x 1.50°
Institut Pierre-Simon Laplace, France	**IPSL-CM5A-LR***	3.75° x 1.88°

	IPSL-CM5A-MR	2.50° x 1.25°
	IPSL-CM5B-LR	3.75° x 1.88°
Japan Agency for Marine-Earth Science and Technology, Research Institute Atmosphere and Ocean (The University of Tokyo), and National Institute for Environmental Studies	*MIROC-ESM-CHEM**	2.81° x 2.81°
	MIROC-ESM	2.81° x 2.81°
Atmosphere and Ocean Research Institute (The University of Tokyo), National Institute for Environmental Studies, and Japan Agency for Marine-Earth Science and Technology	*MIROC4h*	0.56° x 0.56°
	MIROC5	1.41° x 1.41°
Max Planck Institute for Meteorology, Germany	**MPI-ESM-LR**	1.88° x 1.88°
	MPI-ESM-MR	1.88° x 1.88°
	MPI-ESM-P	1.88° x 1.88°
Meteorological Research Institute, Japan	***MRI-CGCM3****	1.13° x 1.13°
	MRI-ESM1	1.13° x 1.13°
	MRI-AGCM3-2S†	0.19° x 0.19°
	MRI-AGCM3-2H†	0.56° x 0.56°
Norwegian Climate Centre	***NorESM1-M****	2.50° x 1.88°
	NorESM1-ME	2.50° x 1.88°

Chapter 5

Observational evidence of the response of tropospheric humidity, clouds and radiation to SST warming patterns

Abstract

Recent studies have suggested that the spatial pattern of sea surface temperature warming influences feedback strengths, and thus is a key factor in climate sensitivity. In this study, we examine observational evidence for a model-based proposed mechanism which relates changes in tropical lower tropospheric (between 1000-700hPa) stability, upper tropospheric (500-200hPa) humidity and cloud cover to different warming scenarios. We test the response of temperature and humidity profiles, clouds and top-of-the-atmosphere radiation to relative warming in tropical areas of strong ascent or descent using 14 years of monthly

mean data. We find that there is strong observational evidence for aspects of the mechanism: if warming is concentrated in areas of descent, there is a decrease in lower tropospheric stability (-1.0±0.1 KK^{-1}) and low cloud cover (∼-7%K^{-1}) with warming, coupled with a strong decrease in net shortwave radiation at the top-of-the-atmosphere (-4.1±0.7$Wm^{-2}K^{-1}$), broadly consistent with other modelling studies. Warmer SSTs in regions of strong convection are coincident with an increase in upper tropospheric humidity (3.3±0.5 %K^{-1}) driving a reduction in non-window clear-sky TOA longwave radiation (-1.0±0.3 $Wm^{-2}K^{-1}$) which is offset by an increase in the window-region driven by surface heating. The longwave cloud radiative effect (3.8±0.9 $Wm^{-2}K^{-1}$) from an increase in high cloud cover (∼7 %K^{-1}), leads to a subsequent all-sky outgoing longwave radiation decrease (-4.6±1.2 $Wm^{-2}K^{-1}$) which represents a significant radiative forcing not explicitly discussed in the proposed hypotheses.

Author contributions: for this chapter, I designed and performed the analysis under the supervision of Helen Brindley. I wrote the chapter with editing from Helen Brindley and Paul Palmer.

5.1 Introduction

The range of equilibrium climate sensitivity (ECS), as described in section 1.2.3, of current GCMs remains large (Zelinka et al., 2020). A major source of uncertainty comes from cloud feedbacks, in particular from marine tropical regions with low, shallow cumulus and stratocumulus clouds (Bony and Dufresne, 2005; Vial et al., 2013; Stevens et al., 2016) and the increase in ECS values in CMIP6 has been linked to decreases in extratropical low cloud (Zelinka et al., 2020). Radiative effects from clouds are complex and depend on a number of cloud properties, including cloud height and optical thickness. In general, low clouds have a stronger shortwave effect than longwave, due to their reflectance of solar radiation and relatively low temperature contrast with the surface. While other cloud types may have stronger radiative effects, the importance of shallow cumulus and stratocumulus clouds in climate sensitivity stems from their abundance (Chen et al., 2000; Stephens, 2005). Therefore, changes to low cloud cover have the potential to lead to large feedbacks, and subsequently strongly influence climate sensitivity. Significant direct feedbacks in the tropical ocean regions also include the closely linked lapse-rate and water vapour feedbacks, driven by relative changes in temperature and humidity between the lower and upper troposphere. Increased temperature aloft leads to increased longwave emission from higher in the troposphere and therefore increased outgoing longwave radiation (OLR): a negative feedback. However, the Clausius-Claperon relationship dictates that an increase in its temperature leads to an increase in the capacity of an air parcel to hold water vapour, a strong greenhouse gas. Under a scenario of fixed relative humidity, this leads to a decrease in outgoing longwave radiation, or a positive feedback (Allan et al., 1999; Held and Soden, 2000). Moreover, these changes in OLR are most sensitive to humidity perturbations in the upper troposphere (Brindley and Harries, 1998).

A number of recent studies point to the importance of the evolution of spatial patterns in sea surface temperatures (SSTs) on the spread of climate sensitivities (Armour et al., 2013; Andrews et al., 2015; Zhou et al., 2016; Andrews and Webb, 2018). The interplay and feedbacks between the relative temperature and humidity in the lower and upper troposphere, and thus tropospheric stability and low-level cloud cover, have been identified as of particular importance (Qu et al., 2015; Ceppi and Gregory, 2017), as well as the extent of tropospheric convective mixing and the impact this has on cloud feedbacks (Sherwood et al., 2014). The ensemble of cloud types over the Pacific warm pool have also been hypothesised to shade underlying ocean, therefore dampening the effect of SST gradients through an albedo feedback (Hartmann et al., 2001; Wall et al., 2019). Patterns of warming in the tropics have also been linked to changes in the water vapour and lapse rate feedbacks, with the ratio of warming in the tropics and extratropics a key factor in local feedback strength (Po-Chedley et al., 2018).

While the concept of ECS arises from models, observational evidence is needed, where possible, to evaluate mechanisms which have been proposed based on model experiments. Recent work has shown that seven GCMs submitted to CMIP6 are able to track anomalies in observed TOA radiation fluxes over the last decades when forced with observed SSTs. However, they do not show the observed sensitivity to SST warming in the east Pacific, suggesting they are not sensitive enough to patterned SST warming Loeb et al. (2020). Observational studies have been used to establish evidence of decreased low cloud cover with surface warming (McCoy et al., 2017), and an associated reduction in net outgoing shortwave radiation (Brient and Schneider, 2016), and generally support a higher ECS from a strong positive low cloud feedback (Fasullo and Trenberth, 2012; Sherwood et al., 2014). There is also evidence that the co-variability of relative humidity, low cloud and shortwave radiation associated with the seasonal broadening of the subtropical subsidence regions and northwards shift of the Hadley cell (Fasullo

and Trenberth, 2012). While there are arguments that using historical responses to warming may not be relevant for the future, thus questioning the utility of observational constraints to climate sensitivity (Armour, 2017), the benefits of observational evidence for process studies is clear. Here, we use observational data from the NASA *Aqua* satellite, namely temperature and humidity profiles, cloud fraction and top-of-the-atmosphere broadband radiation flux, to evaluate evidence of a hypothesised mechanism which links atmospheric and cloud responses to patterns in sea surface temperature. We begin with a description of the proposed mechanism in section 5.2. We then outline the data and methods used in this study in section 5.3, present the results in section 5.4 and draw our conclusions in section 5.5.

5.2 Tropical ocean characteristics and proposed mechanism

In this section, we summarise the main aspects of recent work which has pointed to the importance of the patterns of SST warming in determining the effect of a warming climate. The specific mechanism we discuss is hypothesised by Zhou et al. (2016) and further refined by Ceppi and Gregory (2017) and Andrews and Webb (2018), with all these studies describing essentially the same mechanism. A key determining factor is the relative warming of sea surface temperatures in convective and subsidence regions of the tropical ocean. In the tropics, solar heating leads to air warming and rising through strong convection, poleward transport aloft, and subsidence in cooler regions. These subsidence regions are associated with strong lower tropospheric stability, often with a temperature inversion at the top of the boundary layer, which leads to an effective stratification of the lower troposphere from the rest of the troposphere, and extensive marine

stratocumulus (Wood and Bretherton, 2006). In convective regions over the tropical ocean, humid air is lifted aloft through efficient vertical mixing and thus exerts influence over the free-tropospheric lapse rates over the whole tropics. It is the different response of these convective and subsidence regions to relative warming, and the subsequent strength of feedbacks within them, which have been hypothesized as being a key process in determining the climate response to warming and which we seek to evaluate observationally. A vital aspect of this hypothesized mechanism is the connection between the upper and lower levels of the atmosphere. While there is the possibility that remote effects of the warming may occur via induced horizontal motion here we focus on its local, vertical impact.

5.2.1 Scenario 1: Warming in subsidence regions

If the SST warming is concentrated in subsidence regions, much of the warming is effectively 'trapped' under the temperature inversion which caps the boundary layer at around 700hPa (Zhou et al., 2016; Andrews and Webb, 2018) leading to warmer, moister air in the lower troposphere, while humidity above the inversion remains low. The effects of this are illustrated in the schematic in Fig. 5.1a. Warmer, moister air at the top of the boundary layer results in decreased inversion strength and reduced cloud cover (Wood and Bretherton, 2006; Wood, 2012; McCoy et al., 2017). The relative warming of the surface compared to the top of the boundary layer reduces lower tropospheric stability, drawing in warm, dry air from above the inversion, which further reduces low cloud cover resulting in a strong shortwave cloud feedback (Fasullo and Trenberth, 2012; Ceppi and Gregory, 2017). As the lower troposphere (below the inversion at 700hPa) warms and becomes less stable, OLR at the TOA increases due to increased surface temperature and less absorption from low clouds. Little warming above the

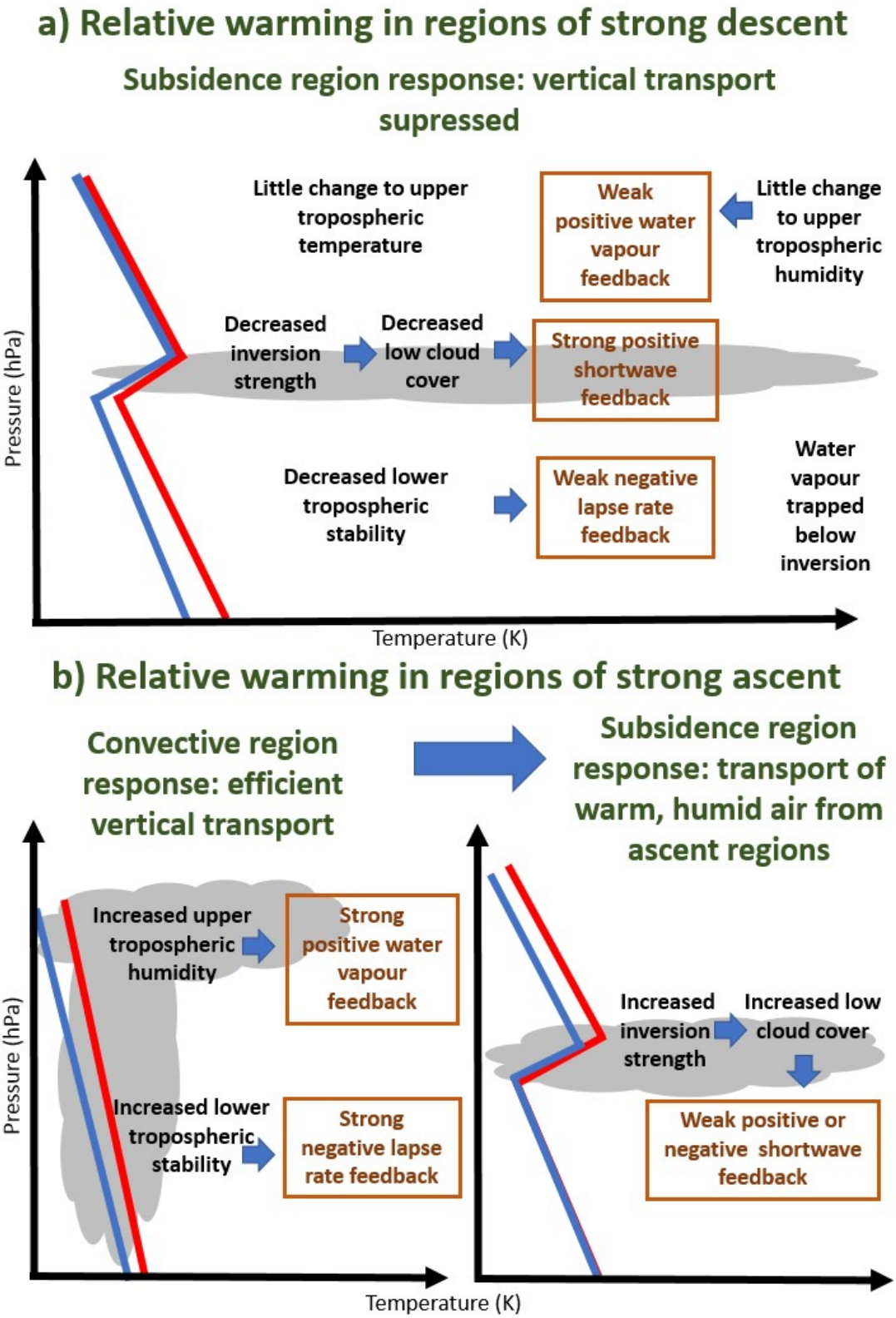

Figure 5.1: Schematic showing hypothesized response to relative warming in a) subsidence regions and b) convective regions of tropical ocean. Part b) is further split into the responses of the convective and subsidence regions. Blue and red lines indicate typical temperature profiles before and after relative warming, respectively. Based on Zhou et al. (2016) and Andrews and Webb (2018).

inversion results in the negative lapse-rate feedback being weak (Fig. 5.1a). The small change in upper tropospheric humidity also leads to a weak positive water vapour feedback (Ceppi and Gregory, 2017). Thus, the net effect is dominated by the cloud feedback, is largely positive and results in a high climate sensitivity (Andrews and Webb, 2018).

5.2.2 Scenario 2: Warming in convective regions

If surface warming is focused in tropical convective regions, the warming is efficiently transported above 700hPa, leading to similar or even greater warming in the mid-troposphere than at the surface. In this situation, stability of the atmosphere increases and, assuming no other change including in cloud cover, OLR will increase due to the relatively warmer temperatures aloft. Increased longwave emission works to counteract the original perturbation and the lapse-rate feedback is negative. However, assuming constant or near constant relative humidity, any increase in upper tropospheric temperature will also lead to an increase in specific humidity. The lapse-rate and water vapour feedbacks counteract each other, reducing the overall feedback parameter in the convective regions to have a weak positive or negative sign.

This process is laid out in Fig. 5.1b as the convective region response. However, the movement of warm, moist air aloft also affects stability in subsidence regions, as lateral transport leads to stronger subsidence, and consequently stability, in the subsidence regions. This leads to increased cloud cover, and either a weak positive or negative shortwave cloud feedback in the subsidence region (Andrews and Webb, 2018).

5.3 Data and Methods

5.3.1 Data

In this study, we use deseasonalised monthly means of radiation, cloud, temperature and humidity data from instruments on the National Aeronautics and Space Administration (NASA) *Aqua* satellite from October 2002 to September 2016 inclusive (14 full years). *Aqua* is in sun-synchronous orbit, with local overpass times of ∼13.30/1.30. By using co-incident measurements from different instruments on the same platform we are able to compare across instruments and examine changes across a range of atmospheric and cloud variables.

In particular, we use broadband all- and clear-sky TOA reflected shortwave radiation (RSR), outgoing longwave radiation (OLR) and window region (WN) radiation flux from the Clouds and Earth's Radiant Energy System (CERES) Single Scanner Footprint at one degree (SSF1deg) Edition 4A (Doelling et al., 2013; Loeb et al., 2018). For CERES, shortwave radiation is defined as 0.3–5 μm, longwave as 5–200μm, and window region 8–12 μm. In addition, we use SSF1deg cloud fraction which is derived from the proportion of clear and cloudy pixels as identified by the Moderate Resolution Imaging Spectroradiometer (MODIS). These data are split into low (surface–700mb), mid-low (700–500mb), mid-high (500–300mb), high (300–70mb) and total (surface–70mb) cloud fractions, with up to two cloud layers possible. We also use Level 2 cloud-cleared surface skin temperature and atmospheric temperature and humidity profiles at 1000, 850, 700, 600, 500, 400, 300, 200 and 150hPa from the Atmospheric Infrared Sounder (AIRS)/Advanced Microwave Sounding Unit (AMSU) (Aumann et al., 2003), version 6. As we are only using ocean data, we hereafter refer to skin temperature as sea surface temperature (SST). Finally, we use vertical velocity at 500hPa from the European Centre for Medium-Range Weather Forecasts (ECMWF) reanalysis

ERA-Interim (ERA-I) to identify regions of strong ascent and descent, as detailed in section 5.3.2. We use all ocean data at 1° x 1° resolution, between 30°S and 30°N.

It is worth noting the differences in definition between the CERES SSF1deg clear-sky radiation fluxes and the AIRS cloud-cleared profiles. The method employed in AIRS utilises clear column radiances in adjacent fields of view to infer cloud-cleared radiances in cloudy scenes with two key assumptions. First, it assumes that a particular type of cloud always has the same radiative properties which scales with cloud amount. Second, it assumes that the temperature and humidity profiles do not differ between cloudy and clear portions of a scene (Susskind et al., 2003). This cloud-clearing method may introduce cold and dry biases, particularly where there are thick clouds (Wong et al., 2015). CERES SSF1deg, by comparison, uses MODIS to identify clear-sky pixels (∼1km), with a CERES footprint (∼20km) categorised as clear-sky if 99% of MODIS pixels are cloud free (Minnis et al., 2011). This results in some missing data in clear-sky radiation fluxes. While we take the average of the day and night overpass measurements to obtain the AIRS monthly means, SSF1deg takes the radiation fluxes as measured at Aqua overpass times, interpolates these into hourly timesteps assuming an invariant scene, and takes the mean over these hourly intervals (Doelling et al., 2013). However, given that we use large spatial averages and monthly resolution data, this is unlikely to have a large impact on our results here.

5.3.2 Methods - definition of Δ $\mathbf{T}_{up}$ and Δ $\mathbf{T}_{down}$

We use and extend the method of isolating relative warming in ascending regions from Zhou et al. (2016). We define our regions of strong ascent and descent based on the vertical velocity at 500hPa (ω500). Points are first sorted into ascending ($\omega500 < 0$) and descending ($\omega500 > 0$). For each of the two regimes, the median

value of the whole tropical value (trp) is used to further sort the points into 'strongly' or 'weakly' ascending/descending at a certain time (t), latitude (n) and longitude (m) i.e if the condition

$$|\omega500(t,n,m)| > median(|\omega500(t,trp)|) \tag{5.1}$$

is satisfied for either $\omega500 > 0$ (descending) and $\omega500 < 0$ (ascending). This method effectively defines four regimes at each timestep: strong ascent, weak ascent, weak descent and strong descent, with the boundaries between strong and weak determined by the median value. Zhou et al. (2016) then use this to define ΔT_{up}, the difference between the mean SST in strongly ascending regions ($\overline{T_{up}}$) and the whole tropical ocean mean SST ($\overline{T_{trp}}$):

$$\Delta T_{up} = \overline{T_{up}} - \overline{T_{trp}}. \tag{5.2}$$

This, and ΔT_{down} calculated in the corresponding manner, gives a measure of the relative warming of the strong ascending or descending regions relative to the mean tropical ocean. One advantage of this method is that by selecting points using vertical velocity instead of geographic regions, we account for periodic shifts in areas of convection and subsidence from both seasonal variations and from large-scale dynamics, for example that from the El Niño Southern Oscillation.

To explore the response of the atmosphere in strongly ascending or descending regions to relative surface warming, we perform linear correlations between ΔT_{up} and ΔT_{down} and selected variables which have been subsetted and averaged in the same way, indicated by an overline and subscripts *up* and *down*. For example, the correlation between ΔT_{up} and $\overline{OLR_{up}}$ examines the co-variability of the outgoing longwave radiation at the top of the atmosphere in ascending regions in response to relative warming in those regions. We do this with temperature, specific and relative humidity, cloud and radiation variables. We also perform this analysis on

two derived variables: upper tropospheric humidity (UTH), defined as the mean relative humidity between 200-500hPa inclusive; and lower tropospheric stability (LTS), defined as the difference in atmospheric temperature at 700hPa and 1000hPa. For clarity, we henceforth refer to the strongly ascending/descending regions as simply 'ascending' and 'descending'. We deseasonalise all the obtained time series by removing the difference between the seasonal mean for that month and the mean across the whole time series.

To estimate the uncertainty, we use the standard error of the mean when taking the mean over the region, e.g. when calculating $\overline{OLR_{up}}$, and propagate this through any further calculations. As the means are taken over large geographical areas, the standard deviation is expected to be larger than measurement uncertainty which, if random, will scale with number of observations. For the linear regressions, we use a least-squares linear regression, weighted to the uncertainty in both x and y. From this, we use the standard error on the fit to give the uncertainty on the gradient. We also obtain the r- and p-values from the fit, to indicate the strength and significance of the relationship. We take $p < 0.001$ to indicate statistical significance.

5.4 Results

In this section, we begin by discussing the characteristics of the ascending and descending regions, in particular two key metrics identified from section 5.2: UTH and LTS. We then extend our analysis by examining the effects of relative warming on temperature, humidity and cloud fraction in the atmosphere, as well as the radiative response at the top-of-the-atmosphere. We do this first for relative warming in ascending regions, followed by descending regions.

Fig. 5.2a and b show maps of the number of times gridpoints were selected for the

ascending and descending regions. We see that, as expected, the points most often in the ascending region are in areas of deep convection, especially over the warm pool in the west Pacific. The gridpoints most often selected for the descending region are located in the sub-tropics, in particular off the western coasts of North and South America, regions associated with extensive stratiform cloud decks.

We find no significant trends in deseasonalised mean temperature for either ascending regions ($\overline{T_{up}}$, Fig. 5.2c) or descending regions ($\overline{T_{down}}$, Fig. 5.2d). We find the amplitude of deseasonalised mean SST variations in ascending regions ($\overline{T_{up}}$), to be similar in magnitude (<1 K) to that in descending regions ($\overline{T_{down}}$). Variations in the mean SST relative to the whole tropical ocean (ΔT_{up}, ΔT_{down}) show a similar amplitude and high month-to-month variability .

As expected for regions of deep convection, high cloud dominates in the ascending regions (Fig. 5.2e), with deseasonalized high cloud fraction typically 40–50 %. Low and mid cloud fractions are lower at ∼10 %. In areas of subsiding air (Fig. 5.2f) we see that low clouds dominate, as expected, with low cloud fractions of 40–50 %, and other higher cloud fractions of <10 %.

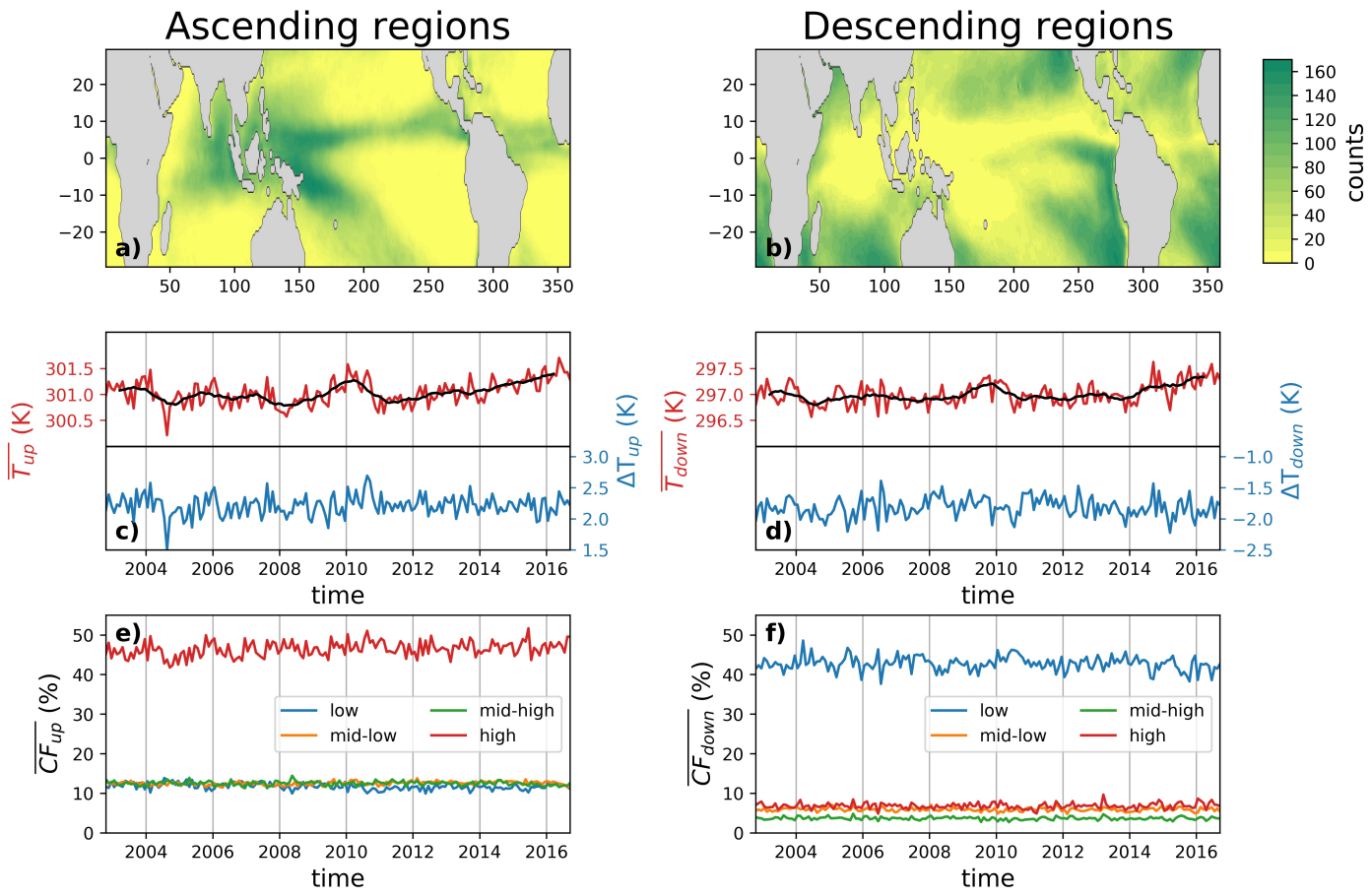

Figure 5.2: a) number of times gridpoints are selected to be in the ascending region, over the whole period this is 19% of points; b) as a), but for descending region, with 31% of points selected over the whole period; c) mean temperature in ascending regions, $\overline{T_{up}}$ with 12-month running mean (black), mean temperature in ascending regions minus mean temperature in all tropical ocean, ΔT_{up} (see section 5.3.2 for definitions); d) as c), but for descending regions; e) mean cloud fraction in ascending region, split into total, low, mid-low, mid-high and high (see section 5.3.1 for definitions); e) as f), but for descending regions.

As described in section 5.2, we expect there to be remote effects of relative warming in convective regions found in regions of subsidence (Fig. 5.1b). Here, we examine only the local effects of warming. While there is a negative correlation between ΔT_{up} and ΔT_{down}, it is not statistically significant, suggesting that relative warming in ascending and descending regions may happen concurrently. While we make no attempt here to address these remote effects, we discuss the role of horizontal motion in section 5.5.

5.4.1 Regions

We now examine two key diagnostics from the expected changes due to relative warming in ascending or descending regions (section 5.2 and Fig. 5.1), UTH (Fig. 5.3a and b) and LTS (Fig. 5.3c and d), as defined in section 5.3.2. In the ascending regions, we see a statistically significant increase in UTH ($3.3\pm0.5\%K^{-1}$) with relative warming (ΔT_{up}), consistent with the transportation of warm, moist air aloft with increased relative temperature. However, this is coupled with a small but statistically significant decrease in LTS ($-0.4\pm0.1KK^{-1}$). This is not expected from the mechanism described in section 5.2, where an increase in relative SST would be accompanied by a similar increase in temperature aloft (700hPa) with respect to the near-surface (1000hPa) (Andrews and Webb, 2018).

In descending regions, where relative warming is hypothesised to be trapped beneath the low level inversion, we see the expected decrease in stability of the lower troposphere (Fig. 5.3d), with a statistically significant decrease of $-1.0\pm0.1KK^{-1}$, and no statistically significant change in UTH.

While some aspects of this initial analysis are consistent with the proposed mechanisms, there are also some inconsistencies which warrant closer analysis, in particular the decrease in stability in the ascending regions with relative SST

warming. This motivates the following section, where we examine the changes in humidity and temperature profiles, as well as changes in cloud fraction and TOA radiation.

5.4.2 Atmospheric, cloud and TOA radiation response to relative warming

Ascending regions

In this section, we focus on relative warming in ascending regions by first examining atmospheric and cloud responses, followed by changes in TOA radiation fluxes. Figure 5.4 shows the slope, r-value and statistical significance of linear regressions between relative SST warming (ΔT_{up}) and temperature ($\overline{temp_{up}}$)(a), specific humidity ($\overline{q_{up}}$)(b) and relative humidity ($\overline{rh_{up}}$) (c) at different pressure levels in the ascending regions. This analysis approach provides us with insight about the vertical extent of SST relative warming effects. Fig. 5.4a indicates a statistically significant warming of $\sim$1.2K per K of ΔT_{up} at 1000hPa. As altitude increases, the rate of warming decreases but remains statistically significant up to 300hPa, with the weakest warming ($\sim$0.7KK^{-1}) at 600hPa. This decrease of warming with altitude in the lower troposphere results in the decrease in LTS noted above, though in general the evidence confirms the efficient transport of the warming through the troposphere.

Fig. 5.4b highlights significant, positive changes in specific humidity from 1000–150hPa, of around $\sim$1.1 gKg^{-1} per K increase ΔT_{up} at 100hPa and decreasing approximately linearly with altitude. These changes in temperature and specific humidity combine to give the relative humidity changes seen in Fig.5.4c: below 850hPa there are no significant changes, but above 850 hPa the relative humidity increases to a maximum of $\sim$5%K^{-1} at 600–500hPa. Above this, the increase in

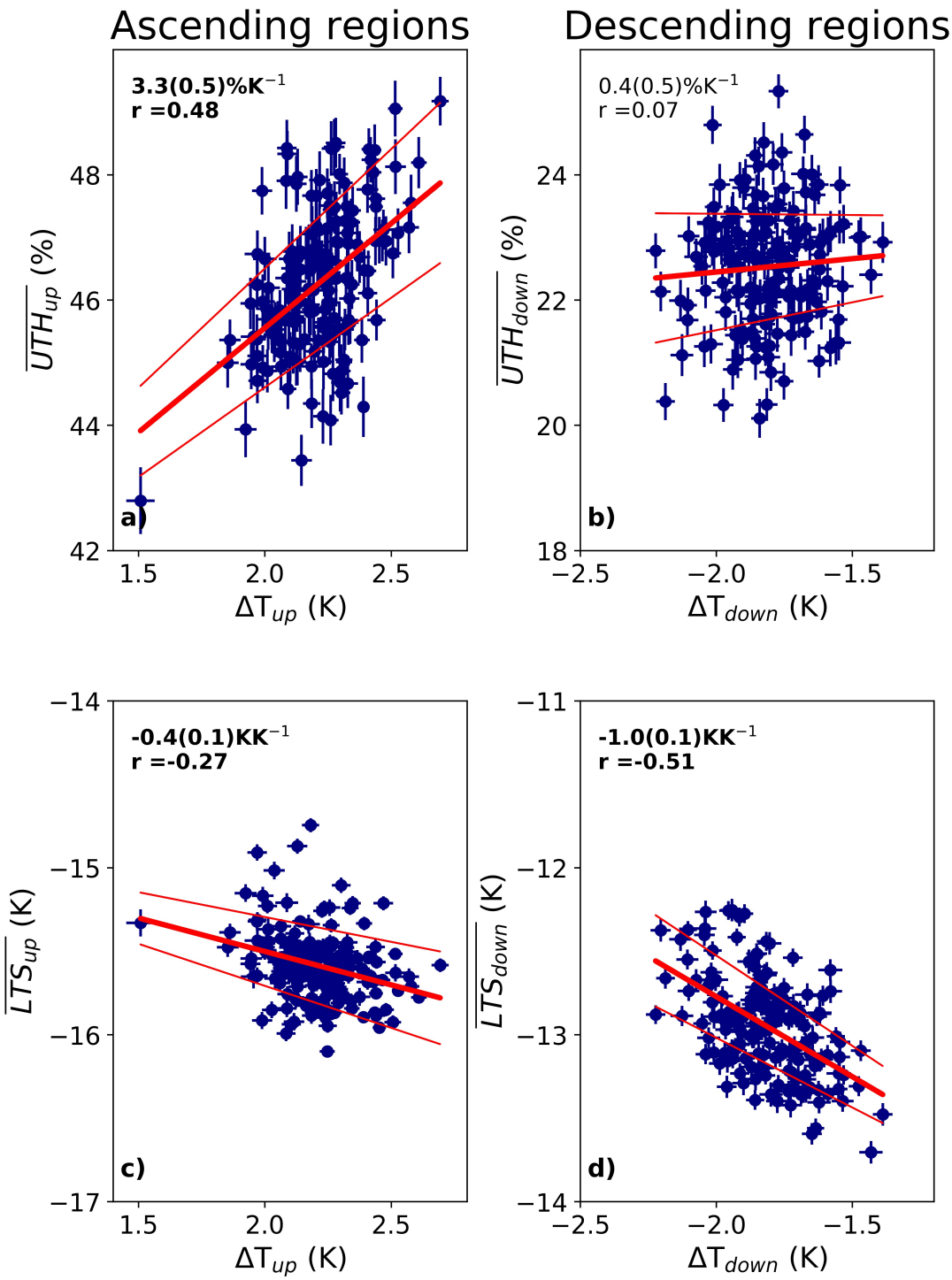

Figure 5.3: Upper tropospheric humidity in ascending (a) and descending (b) regions against relative warming ΔT_{up} and ΔT_{up}, respectively. Error bars are standard error on the mean (see section 5.3.2). Linear fit is given in bold red, with standard error as thin red lines. Text insert gives slope of regression fit and r-value, and is in bold text if statistically significant to $p \leq 0.005$. Plots c) and d) are as a) and b), but for lower tropospheric stability.

relative humidity is lower, but still statistically significant. This analysis clearly shows that the relative warming in regions of strong convection results in warm, moist air being efficiently lofted into the the upper troposphere, consistent with the hypothesised mechanism.

We now examine linear regressions in cloud fraction with ΔT_{up} (Fig. 5.4d). We see that there are significant changes in total, low mid-high and high cloud fraction of approximately 3%K^{-1}, -2.5%K^{-1} and 7%K^{-1} respectively. We interpret the increase in high cloud fraction as follows: an increase in local SST leads to an increase in convection and subsequently an increase of clouds forming at, or rising to, higher altitudes. We attribute the decrease in low cloud fraction as part of this process, and note that although the increase in high cloud may be masking the detection of low cloud, the low cloud fraction decrease is consistent with the decrease in LTS (Wood and Bretherton, 2006).

Next, we examine changes to the TOA broadband radiation fluxes associated with these atmospheric and SST changes. Figure 5.5 shows shortwave, longwave and window-region all-sky fluxes, clear-sky fluxes and cloud radiative effect (CRE, defined as all-sky - clear-sky) in ascending regions (i.e. $\overline{RSR_{up}}$, $\overline{OLR_{up}}$, $\overline{WN_{up}}$). The final row of plots shows the non-window portion of the OLR, namely $\overline{(OLR - WN)_{up}}$. In the shortwave (Fig. 5.5a-c) we note that there are no significant correlations in any of the all-sky, clear-sky and CRE fluxes. In the longwave, we see a statistically significant decrease in all-sky $\overline{OLR_{up}}$ (-4.6±1.2 Wm^{-2}K^{-1}, Fig. 5.5d), which arises from cloud effects (-3.8 ±0.9 Wm^{-2}K^{-1}, Fig. 5.5d). The decrease in CRE is consistent with our hypothesis of enhanced convection with ΔT_{up}, leading to the observed increase in high cloud fraction and a reduction in the longwave emission to space. While an enhancement in high cloud fraction might also be expected to enhance RSR we hypothesise that the small reduction in low cloud fraction is sufficient to counteract this effect.

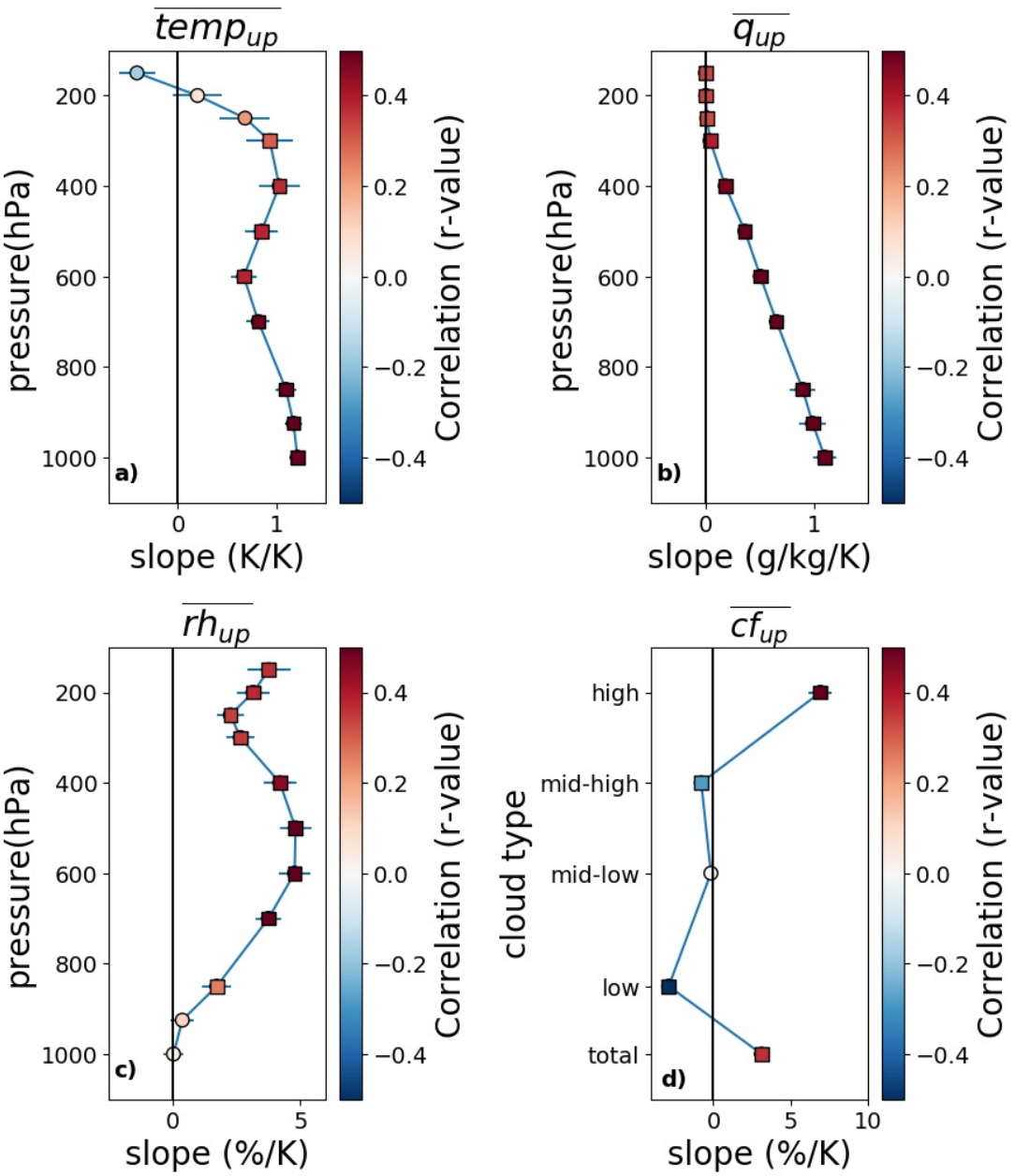

Figure 5.4: Correlation plots of atmospheric and cloud responses to relative warming in ascending regions. Plots show, for different pressure levels, slope of linear fit between ΔT_{up} and a) temperature b) specific humidity and c) relative humidity. Colour of circle or square gives r-value of the fit, with standard error on the slope as error bars. Squares indicates whether the fit is statistically significant, as defined by p <0.005, with circles representing points which are insignificant. Plot d) is similar, but shows correlation for total, low, mid-low, mid-high and high cloud fraction.

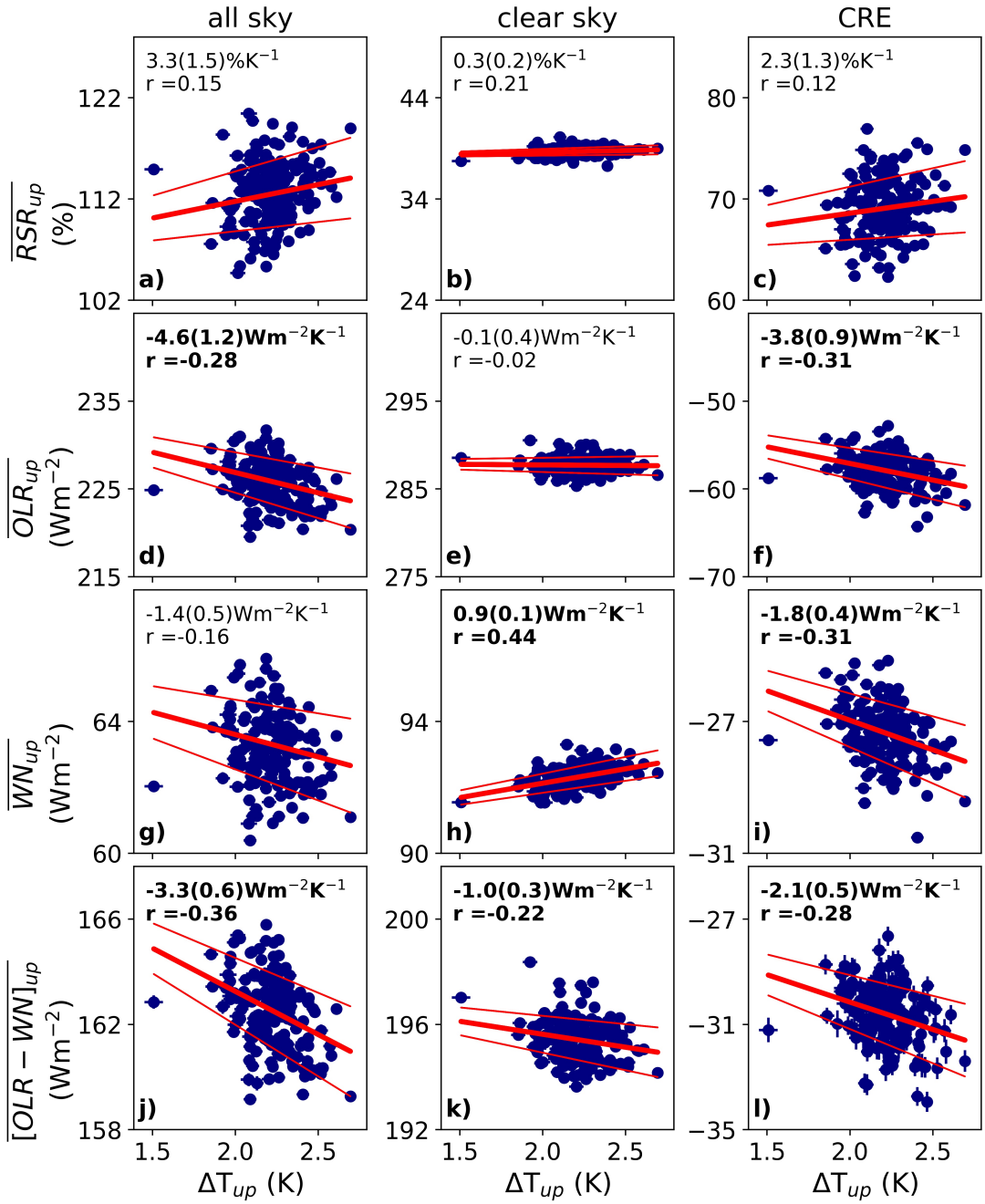

Figure 5.5: Top-of-atmosphere ascending region radiative response of all-sky, clear-sky and cloud radiative effect (CRE, defined as all-sky-clear-sky) shortwave, longwave, window and non-window (defined as total longwave - window) fluxes to changes in SST in ascending regions relative to mean tropical SST changes (ΔT_{up}). Radiation flux data from CERES SSF1deg, SST data from AIRS (see section 5.3). Text indicates slope and r-value from linear regression (bold red line), with standard errors on the regression line (thin red lines), through monthly means over ascending regions. Text insert is in bold text if statistically significant to $p \leq 0.005$.

The correlations of ΔT_{up} with window and non-window OLR gives us more insight into the physical processes occurring. The highly transparent window is sensitive to both surface conditions and the presence of cloud while non-window fluxes are more affected by changes in the mid-troposphere. Although there is no statistically significant change in clear-sky $\overline{OLR_{up}}$ (Fig. 5.4 e), this is due to the cancellation of the window and non-window effects (Fig. 5.4 h and k). Conversely, the CRE decreases in both the window region (Fig. 5.4 i) and non-window region (Fig. 5.4 l). Together, they combine to give the overall decrease in longwave CRE (Fig. 5.4 f).

We now explore these window and non-window effects in more detail. We see that the change in all-sky $\overline{OLR_{up}}$ radiation at the TOA (Fig. 5.5d) is driven by a decrease in the non-window region (-3.3$\pm$0.6Wm^{-2}K^{-1}, Fig. 5.5j). These non-window changes are due to both clear-sky (-1.0$\pm$0.3Wm^{-2}K^{-1}, Fig. 5.5k) and CRE effects (-2.1$\pm$0.5Wm^{-2}K^{-1}, Fig. 5.5l). While the CRE is also likely to be linked to increased high cloud, the clear-sky decrease is further evidence that humidity changes in the upper troposphere have a significant effect. Turning to the window region, we attribute the clear-sky window region increase (0.9$\pm$0.15Wm^{-2}K^{-1}, Fig. 5.5 h) to surface warming, which is offset by the CRE of increased high cloud fraction (-1.8$\pm$0.4Wm^{-2}K^{-1}, Fig. 5.5i), resulting in no statistically significant change in the all-sky window region (Fig. 5.4).

To summarise our results for the ascending region, we find strong observational evidence for the mechanism described by Andrews and Webb (2018). A relative increase in SST in regions of strong ascent (ΔT_{up}) leads to the vertical transport of water vapour to the upper troposphere. Temperature increases are observed throughout the troposphere, but the largest temperature changes are at the near-surface. The temperature and humidity changes result in an increase in UTH, and a decrease in LTS, with an associated small decrease in low cloud cover and a

large increase in high cloud cover. It is this increase in high cloud cover which has the dominant radiative effect leading to a strong decrease in $\overline{OLR_{up}}$ with ΔT_{up}.

Descending regions

In this section, we examine the effects of relative warming in descending areas (ΔT_{down}). As for the ascending region, we start by presenting the correlations of temperature, humidity and cloud variables in descending regions in response to relative warming, followed by the response of TOA radiation.

We see from Fig. 5.6a that there are statistically significant correlations between ΔT_{down} and $\overline{temp_{down}}$ up to 850hPa. The strength of the response decreases with altitude, from approximately 1.1KK^{-1} of ΔT_{down} at 1000hPa, to ∼0.6KK^{-1} at 850hPa. The increases in atmospheric temperature with relative surface warming are no longer statistically significant above 700hPa, consistent with the trapping effect of a temperature inversion and with the hypothesised mechanism (section 5.2). Statistically significant increases in specific humidity ($\overline{q_{down}}$, Fig. 5.6b) are also constrained to the lower parts of the troposphere and decrease in strength with altitude. However, increases are observed as high as 600hPa. The combined changes in temperature and specific humidity result in statistically significant changes in relative humidity between 850–600hPa of ∼3.5%K−1 (Fig. 5.6).

Combined, these patterns explain our section 5.4.1 observations that there is a decrease in LTS with increasing ΔT_{down}, and no increase in UTH. Temperature increases constrained to below 700hPa inversion, with the largest increases near the surface. Increases in specific humidity up to 600hPa drive an increase in relative humidity up to this altitude, but do not reach the upper (500-200hPa) troposphere. Consistent with the decrease in LTS, we see a strong decrease (∼6%K^{-1}) in low cloud cover in descending regions with relative SST warming.

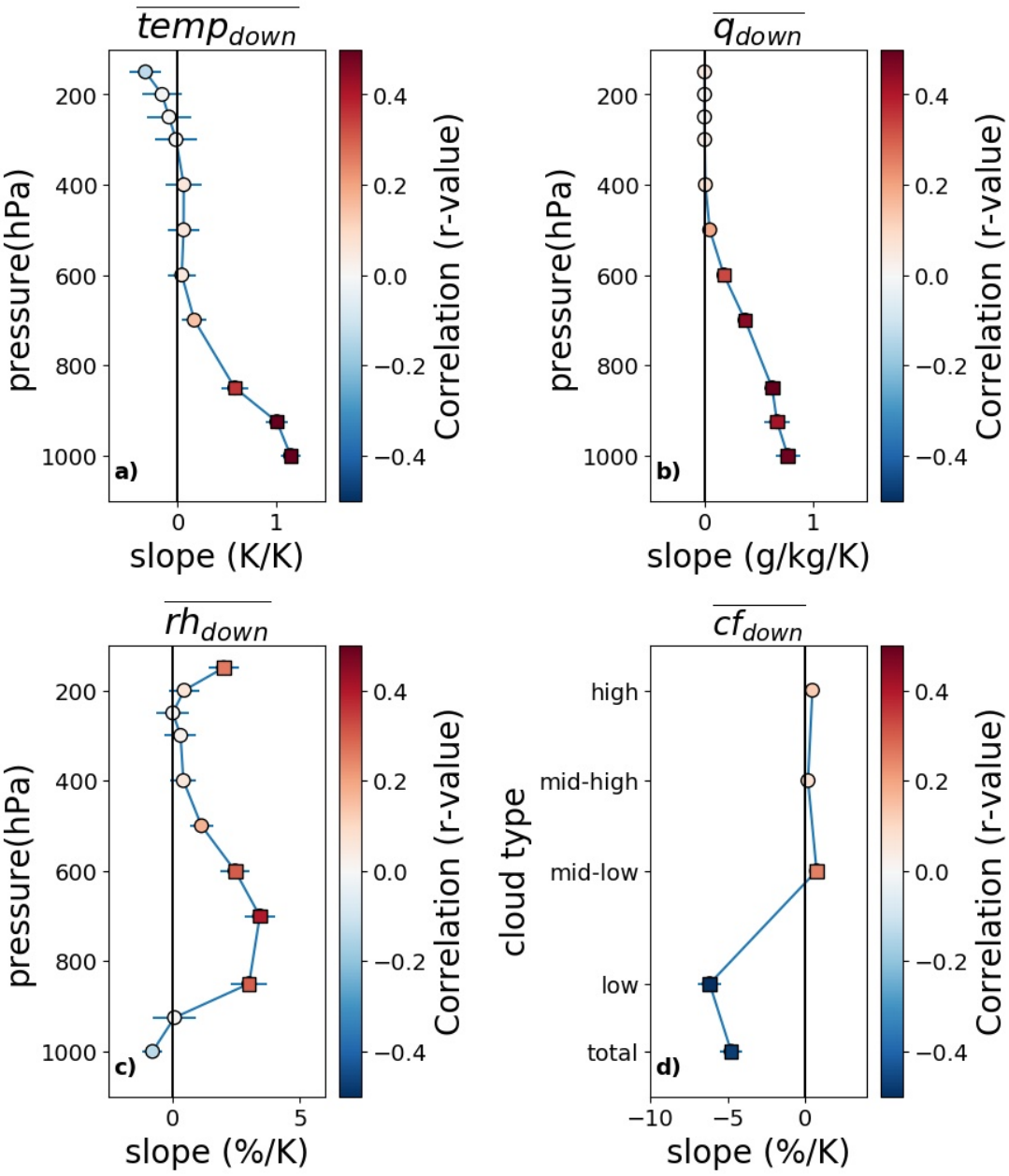

Figure 5.6: As Fig. 5.6, but for descending regions.

While there are statistically significant increases in mid-low cloud fraction, these are small and the response of the total cloud fraction is driven by changes in low cloud fraction and is therefore negative ($\sim$-5%K^{-1}).

Turning to the correlations between TOA radiation fluxes and ΔT_{down}, we see a strong response in the shortwave (Fig. 5.7a-c). There is a decrease in all-sky shortwave in descending regions ($\overline{RSR_{down}}$) of -4.1$\pm$0.7 Wm^{-2}K^{-1}, which is driven by cloud effects (Fig. 5.7c) in response to the decrease in low cloud fraction.

In the longwave, there is no statistically significant correlation between $\Delta T(down)$ and longwave all-sky, clear-sky or CRE (Fig. 5.7a-c), despite significant changes in the window region (Fig. 5.7a-c). This is due to the lack of statistically significant change in the non-window region of OLR, which accounts for the larger part of the spectrum. In the window region, we see an increase in clear-sky $\overline{OLR_{down}}$ (0.7$\pm$0.1Wm^{-2}K^{-1}, Fig. 5.7h) from surface warming, and a CRE of 0.7$\pm$0.1Wm^{-2}K^{-1} (Fig. 5.7h) which may be due to the small increase in mid-low cloud fraction.

To summarise our results for the descending region, we find evidence to support the trapping of temperature by the low level inversion, and the associated decrease in LTS and low cloud cover. However, while temperature increases are only observed up to 850hPa, there are changes in specific humidity up to 600hPa.

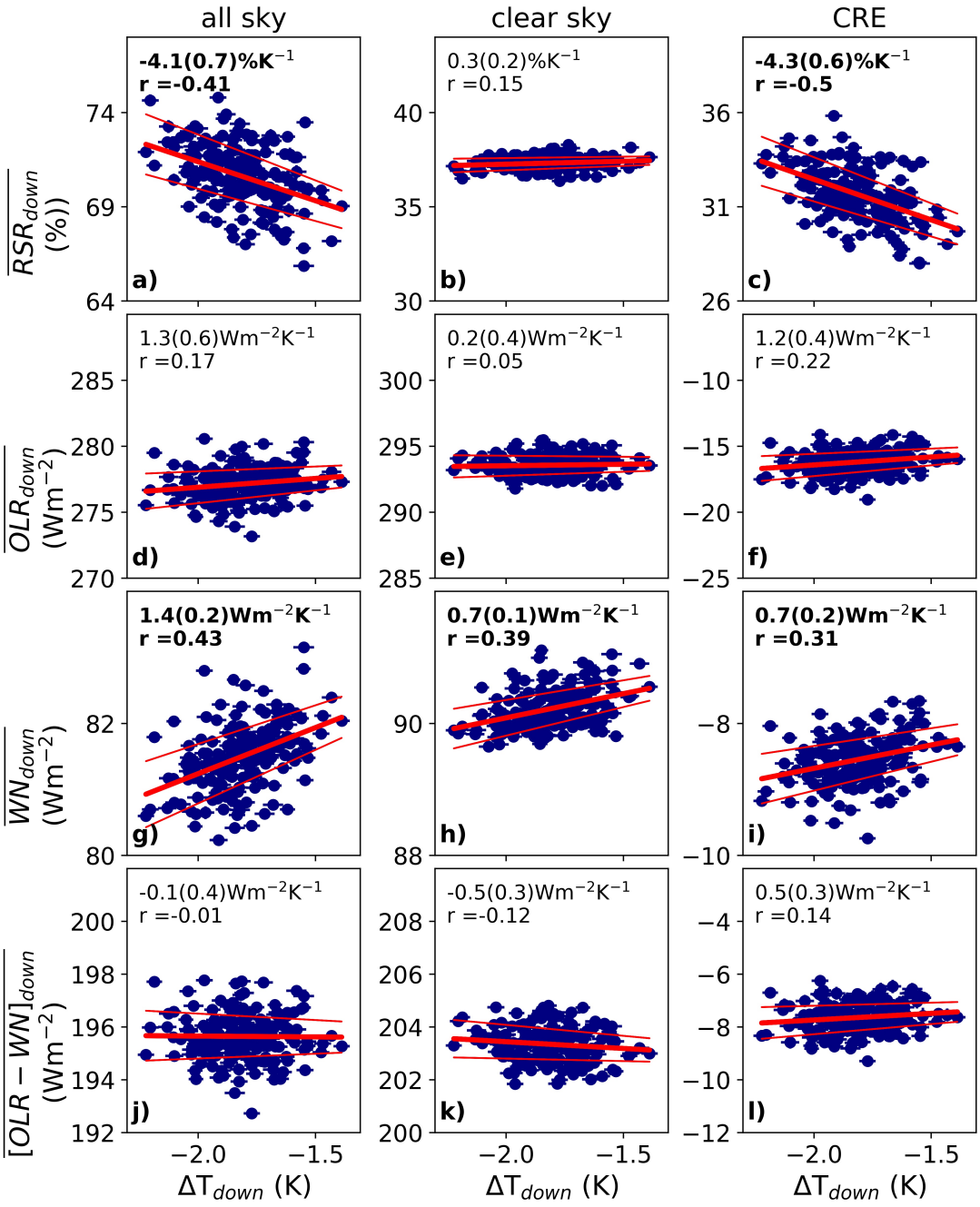

Figure 5.7: As Fig. 5.5, but for descending regions.

5.5 Discussion and Conclusions

In this study, we use temperature, humidity, cloud and radiation measurements from AIRS and CERES to evaluate evidence of a model-based proposed mechanism of the atmospheric response to relative sea surface temperature (SST) warming. We use 14 years of monthly mean data, an appropriate timescale and resolution for evaluating this mechanism since there is evidence that future warming may mimic the seasonal shifts in co-variability between relative humidity and cloud albedo (Fasullo and Trenberth, 2012). Generally, the evidence we find supports the mechanism proposed by Zhou et al. (2016) and Andrews and Webb (2018), though there are some inconsistencies which we discuss further in this section. The proposed mechanism hinges on the location of relative warming. We use the method of Zhou et al. (2016) to isolate responses of ascending regions, characterised by warm SSTs, deep convection, and descending regions, characterised by cooler SSTs, a strong inversion and low cloud, using ERA-Interim vertical velocity at 500hPa.

Patterns of SST warming in the past decades have been concentrated in the tropical marine ascent regions, and have been linked to damped warming in the last decades (Zhou et al., 2016). While we do not see evidence of this warming here, likely due to the relatively short period examined, we nevertheless expect that relative warming in areas of strong ascent would lead to warm, moist air being efficiently transported into the upper troposphere. We expect this to lead to either little change to, or an increase in, low level stability, as atmospheric temperatures at 700hPa increase at the same or higher rate than the near surface (Andrews and Webb, 2018). We also expect the humidity in the upper troposphere to increase.

Our evidence generally supports this mechanism, with a strong increase in upper tropospheric humidity (UTH) with relative warming. However, the increase in

atmospheric temperature decreases with altitude, up to 600hPa and therefore warming aloft is lower than at the near-surface. Combined with a approximately linear reduction in the specific humidity increases with altitude results in an increase in relative humidity above the 850hPa, with no changes above. This indicates the efficient vertical lofting of warm, moist air in convective regions. What is striking, however, is that the reduction in longwave cloud radiative effect from higher, cooler clouds is the greatest effect on the TOA radiation budget, implying that this may be the dominant radiative effect in the scenario of relative warming in convective regions.

In subsiding regions, we see evidence that the vertical motion of the atmosphere is suppressed by the inversion, and that there are strong temperature increases with relative SST warming in the lowest levels of the atmosphere (1000–850hPa) but no significant increases above this. This amplification of temperatures below the inversion leads to the reduction of lower tropospheric stability and a strong decrease in low cloud cover, with a resultant decrease in TOA outgoing shortwave radiation flux. This is consistent with previous work which has found that the strongest radiative effects of warming in subsidence regions is from shortwave cloud effects, followed by a less negative lapse-rate, linked to lower tropospheric stability and inversion strength (Ceppi and Gregory, 2017). However, we do also see note statistically significant changes in specific humidity, and therefore also relative humidity, at higher altitudes (up to 600hPa).

Despite this, the largest changes in specific humidity are close to the surface, which may also affect cloud cover: the amplification of specific humidity below the inversion has been highlighted as a key controlling factor in low cloud thinning and reduction (van der Dussen et al., 2015).

Finally, as noted in section 5.3, our method does not strictly separate the local and remote effects of this mechanism. From the hypothesised mechanism (section

5.2) we might expect that relative warming in convective regions would result in increased lower tropospheric stability and low cloud cover in subsiding regions. While we do not observe these effects directly here, they may be reducing the extent of the local effects, namely a decrease in LTS and low cloud cover, which we do observe.

Despite some uncertainty due to the observational data coverage, we believe our conclusions are robust. The large spatial averages and the use of monthly averages mean that missing clear-sky data are unlikely to have a large impact on our conclusions. The independent, co-located CERES and AIRS data show a consistent picture, adding weight to our analysis, and there is also general agreement in behaviour with ERA-Interim (not shown). As OLR is also available from AIRS for both all- and clear-sky conditions, we test how our analysis may be affected by the different sampling approaches of AIRS and CERES (described in section 5.3), by reproducing Figs. 5.5d, e and 5.7d, e using just data from AIRS (not shown). The behaviour in both ascending and descending regions is broadly similar to that when using AIRS and CERES data together, suggesting this is unlikely to affect our conclusions. We also test the effect of differing solar zenith angles in selected regions, by examining the proportion of incoming solar radiation reflected at the TOA, and find that this does not affect our conclusions (not shown). While systematic biases in the AIRS data may affect the magnitude of the correlations shown here, our key conclusions are unlikely to be affected. Another aspect is the sensitivity to the choice of median for defining regions of strong ascent and descent. We argue that a broad selection criteria is appropriate to select a coherent geographical region to reduce noise and focus on robust, large-scale relationships. The use of monthly mean vertical motion may include days of compensatory negative and positive motion, though again the use of large-area spatial means should mitigate against this. Furthermore, the maps of strongly ascending and descending regions are broadly as expected.

Our work here raises some interesting questions for future study. Firstly, it has been focused on the local effects of relative warming: how warming in ascending/descending regions affects the atmospheric temperature, humidity, clouds and radiative properties in the regions themselves. However, many of the modelling studies draw particular attention to the effects of warming in ascending areas on free-tropospheric temperature and humidity, and the subsequent effect on subsiding region stability and low cloud cover (Zhou et al., 2016; Andrews and Webb, 2018). While our work here has addressed an underlying mechanism (the ability of relative warming to impact upper tropospheric properties), it would be an interesting question for future work to assess observational evidence of remote effects. Additionally, we examine month-to-month variability here, with no attempt to quantify the effects of prolonged warming, nor do we take the relative geographical size of the regions, and therefore the total effect on global radiation budget, into account. It would be of interest to know understand whether temperature and humidity changes in ascending or descending regions are uniform, or whether there are spatial patterns which could be linked, for example, to monsoon systems.

In conclusion, while our study largely supports the hypothesised mechanism, there are some aspects where we suggest some modifications. It would be of interest to know to what extent GCMs are able to reproduce these aspects, and also how the magnitude of the temperature, humidity, cloud and TOA radiation changes compare. In particular, we note the large longwave cloud effect of relative warming in ascending regions.

Chapter 6

Discussion and Conclusion

In this final section, I review and discuss the main aims of my thesis within the context of previous studies, followed by a critical assessment of the methods I used and their limitations. I then discuss questions raised by this work and possible avenues of future work.

6.1 Discussion of aims of this thesis

In broad terms, the aim of my thesis has been to use observations and models together in order to interpret TOA and surface radiation fluxes and the processes which drive them, as described in section 1.1. Chapters 3 and 4 were largely centred around the evaluation of NWP and climate model radiative fluxes, establishing benchmark observational metrics and interpreting differences with respect to atmospheric properties such as clouds, aerosols and water vapour. While Chapter 5 was also concerned with the co-variability of clouds and atmospheric temperature and humidity profiles, my analysis focused specifically on assessing observational evidence of a mechanism believed to be important in

determining equilibrium climate sensitivity, which had been hypothesised based on climate model simulations.

6.1.1 Model evaluation: radiative biases and links to atmospheric processes

Chapters 3 and 4 were mostly concerned with evaluating model output of radiation fluxes and other relevant variables, though over very different temporal and spatial scales. In Chapter 3, I used observational data from a single point, Niamey (13°29'N, 2°11'E), at a daily frequency. This data was suitable for evaluation of 43r1, a later cycle of ECMWF's IFS than that used for ERA-Interim. Reanalysis aims to simulate the state of the atmosphere at a particular time and place, with a short time step (15 minutes) and a small grid ($\sim$ 29 km), and regularly assimilates observational data.

In contrast to this, the GCMs I evaluate in Chapter 4 are not designed for forecasting at a particular time and place, rather to simulate the large-scale dynamics and features of the Earth's climate. While I also use atmosphere-only models in Chapter 4, which are forced with observed SSTs, the majority of the analysis is with coupled model runs which run freely from their initialisation, therefore a particular year in the model output does not correspond to that particular year from observations. The temporal frequency of the output is also longer (1 month) and the horizontal grid sizes vary but are generally of the order of $\sim$100km. Therefore, I use larger spatial averages and a 15 year monthly seasonal cycle for the evaluation.

Despite the differences in the models, NWP models such as 43r1 and GCMs share some similar aspects, and it is of interest to study both in conjunction with observations. As Walsh et al. (2009) argue, reanalyses often use similar

formulations of clouds and radiation as GCMs, they circumvent some of the unconstrained errors of GCMs by assimilating data. As well as this, NWP model output is often available at higher temporal frequency than that from GCMs, which can provide insight into the correspondence of bias across temporal scales.

Radiation fluxes

A key motivation of this thesis has been interpreting differences in the observed and modelled radiation fluxes at the TOA and the surface. While I discuss sources of radiation bias in modelled radiation fluxes in the following sections, in particular those associated with clouds, water vapour and aerosol, it is necessary to start with an evaluation of biases in radiation fluxes themselves. In general, I found that 43r1 overestimated the solar radiation reaching the surface as downwelling shortwave radiation (DSR), and underestimated how much was reflected back to space as reflected shortwave radation (RSR). The overestimation of DSR led, despite some influence of the surface albedo, to an overestimate of the upwelling shortwave radiation (USR). Broadly, this was also the case in the GCMs examined in Chapter 4: the multi-model mean of RSR was lower than observations for RSR and higher for DSR, though the models showed considerable spread. In the longwave, I found that 43r1 had a tendency to underestimate the surface downwelling longwave radiation (DLR) and upwelling longwave radiation (ULR) fluxes, and overestimate the outgoing longwave radiation (OLR) to space. Again, this was broadly consistent with the multi-model mean of the CMIP5 models in Chapter 4.

These results generally agree with past studies: for GCMs on a global scale, Li et al. (2013) and Dolinar et al. (2015) found an underestimation of RSR and an

overestimation of OLR, while surface studies have documented the excess clear-sky DSR and underestimation of clear-sky DLR at the surface (Wild et al., 1995, 2013).

Clouds

The energy budget of Niamey, and the wider west African region, is heavily determined by clouds associated with the west African monsoon, and it is clear from Chapters 3 and 4, as well as other studies, that this remains challenging for both reanalyses and GCMs. As described in sections 3.1.1 and 5.4.1 the monsoon is characterised by the progression of deep convective clouds which pass northwards over the coastal region and into the Sahel, before retreating, bringing a distinctive wet and dry season to the latter region and a 'little dry season' to the former. In Chapter 4, I found that the predominant problem associated with monsoon cloudiness in the CMIP5 coupled models stemmed from the timing and extent of the monsoon. Modelled monsoon onset was later in the year and the northwards extent too far south, with respect to the reference products, which were largely, though not entirely, linked to their SSTs, consistent with past studies (Roehrig et al., 2013). While I did not find evidence of a mistiming of the monsoon in 43r1 in 2006, the year studied in Chapter 3, a wider study of multi-year onset and cessation dates of the monsoon found a late onset in ERA-I in west Africa (Dunning et al., 2016). Nevertheless, in Chapter 3 I did find evidence that the representation of the clouds associated with the monsoon is responsible for some of the radiation bias in 43r1 consistent with the GCMs evaluated in Chapter 4.

The deep convective clouds associated with the monsoon have an effect in both the long- and shortwave (e.g. Slingo et al., 2009). In Chapter 3 I linked the lack of ice content of the clouds in 43r1 to too much solar radiation reaching the surface, and too little solar radiation being reflected at the TOA: for example, the

discrepancy between 43r1 and the observational ice water path (IWP) explained 43% of the variability in the discrepancy in RSR. In Chapter 4, while there are also indications of too much shortwave radiation reaching the surface in all-sky conditions, the links to cloud properties were less clear (not shown). Previous studies, however, have shown evidence that a lack of cloud ice leads to GCM shortwave bias (Li et al., 2013). Instead, I examined the effects of clouds on the radiation budget from the longwave perspective, specifically using the TOA cloud radiative forcing (CRF, difference between all- and clear-sky OLR) and atmospheric cloud radiative effect (CRE, the net longwave radiation flux entering the atmospheric column). Even when using the atmosphere-only models, I found that the CMIP5 modelled longwave CRE and CRF was reduced with respect to the satellite estimates from CERES EBAF, consistent with other studies (Hill et al., 2016). While the definitions of clear-sky in satellite products and observations (discussed further in section 6.2.2) may account for some of this difference, this points to a tendency of the GCMs to underestimate the longwave impact of the deep clouds associated with the monsoon.

Aerosols

Another source of model bias which was common to both 43r1 and the CMIP5 models, was that of the representation of aerosol. Aerosol, in particular black carbon from the burning of biomass and mineral dust from the Sahara, is another major factor in the radiation budget at both the surface and the TOA in the west African region (Slingo et al., 2006). As discussed in section 1.3, aerosol is highly variable in both time and space, and therefore poses challenges for models, evident in both Chapters 3 and 4: while there is a seasonal cycle (Figs. 3.4c, 4.5 and 4.6) in aerosol optical depth (AOD), linked to the wet/dry season, this varies between sites which are geographically quite close (Fig. 4.6g-h), and there can be large day-to-day variations at the same site (Fig. 3.4c).

In general, I found that both 43r1 and the GCMs in CMIP5 underestimated AOD with respect to the references used. While in Chapter 3, I attributed some of the observation and 43r1 differences to the use of an aerosol climatology, in Chapter 4 selecting just models which used an interactive scheme did not necessarily lead to an improvement in the multi-model mean. I suggest further work to address this in section 6.3. In Figs. 4.8 and 4.9 I found models which have a particularly low bias in AOD tended to overestimate clear-sky DSR and underestimate clear-sky DLR with respect to EBAF/SYN1deg. Work by Wild (1999) linked the lower aerosol loadings in GCMs to significant radiation biases, and more recent work suggests it remains a problem for both NWP models (Haywood et al., 2005; Milton et al., 2008) and GCMs (e.g. Wild et al., 2006).

Aside from the absolute amounts of AOD, the contrasting sensitivities of surface broadband radiation fluxes in models with respect to the references was examined in both Chapters 3 and 4. In Chapter 3, there was a higher degree of co-variability between dry-season DSR and AOD in the observation than in 43r1, where there was no statistically significant correlation. Similarly, in Chapter 4, I found that the clear-sky DSR in the CMIP5 models was largely insensitive to variations in AOD, far less so than EBAF/SYN1deg (Fig. 4.8). While the methods of these two calculations are very different (daily all-sky DSR data over one year at a single point in Chapter 3, large area averaged clear-sky DSR monthly anomaly from a seasonal mean in Chapter 4) and therefore it is not possible to make a direct comparison between the two, there are indications that the observations indicate a higher degree of sensitivity in DSR than in a reanalysis (43r1), and that the sensitivity seen in a different product that uses reanalysis (EBAF/SYN1deg) is higher than the majority of GCMs.

In the longwave, the opposite is true. In Chapter 3, I found that while there was little co-variability between AOD and DLR in the Atmospheric Radiation Measurement (ARM) Mobile Facility (AMF) data ($r^2 = 0.04$ over the whole year,

Table 3.5), there was a statistically significant correlation in 43r1 ($r^2 = 0.31$). Correspondingly in Chapter 4, the observed correlation coefficient between AOD and clear-sky DLR was low, with a number of the GCMs used showing a greater sensitivity than EBAF/SYN1deg (Fig. 4.9). While there is the same significant caveat to this observation regarding the different calculations in Chapters 3 and 4 described above, this is nonetheless interesting. What is not clear from my analysis is whether the co-variability between DLR and AOD is a direct effect on radiation, or whether it arises through interactions between aerosols and clouds: I suggest approaches to clarify this in section 6.3.

Water vapour

The atmospheric humidity profiles provided by the AMF sonde ascents provided the estimates of TCWV used in Chapter 3. Aside from the first dry season, the 43r1 modelled TCWV simulated the variability over the year with a correlation coefficient $r^2 = 0.8$ (Table 3.3), with a bias of TCWV over the whole year of 0.2 cm. Unfortunately, there were no reliable estimates of TCWV from the surface stations I used in Chapter 4, so therefore the reference I used was from ERA-Interim, an earlier cycle of ECMWF's IFS: that 43r1 had performed well against the radiosonde observations in Chapter 3 therefore added confidence to this as a reference for the GCMs in CMIP5.

As with AOD, an aim in the analysis was to understand the degree of sensitivity in surface flux variations to TCWV. For all-sky DSR at Niamey, I found that there was a lower degree of co-variability in the observations than in 43r1, especially in the first dry season (compare $r^2 = 0.11$ to 0.64 for the observations and 43r1, respectively in Table 3.4). It is possible that this higher correlation may be due to the lack of sensitivity to AOD. As the DSR observations were for all-sky conditions, it is not explicit if the co-variability between DSR and TCWV is

through direct absorption or indirectly through clouds. However, the statistically insignificant correlation between TCWV and IWP means there is no strong evidence for TCWV affecting DSR through the examined cloud properties. For the GCMs examined in Chapter 4, models which were drier than EBAF/SYN1deg tended to overestimate shortwave radiation reaching the surface under clear-sky conditions (Fig. 4.8a-d), and almost all of the models had a higher degree of correlation between TCWV anomalies and clear-sky DSR anomalies than EBAF/SYN1deg (Fig. 4.8e-h). The general picture points to a higher sensitivity of clear-sky DSR to TCWV in models than in observations. As these are clear-sky estimates, the suggestion is that the water vapour influences DSR through direct absorption of shortwave radiation. Fildier and Collins (2015) found that the spatial distribution of water vapour in GCMs, as well as the low spectral resolution of their radiation codes, led to a large inter-model spread in clear-sky shortwave absorption. While these factors were not directly investigated, these are potential underlying reasons for the differences in co-variability presented in this study.

For DLR, there is also a stronger degree of co-variability with TCWV in 43r1 (r^2 = 0.91 over the whole year, Table 3.5) than in the observations (r^2 = 0.53). In Chapter 4, I found that models which were particularly dry tended to have the largest biases in clear-sky DLR. However, while the CMIP5 models had a range of correlation coefficients between clear-sky DLR and TCWV, EBAF/SYN1deg was approximately in the middle of this range.

6.1.2 Observational evidence of model-based hypothesis

My analysis in Chapter 5 assessed observational evidence to support a mechanism which had been hypothesised from climate model experiments. My work in Chapter 5 therefore demonstrates another facet of model evaluation. Climate

models are required for projections of future changes to climate, and while it is important that they are able to simulate the observed radiation budget, it is also vital that we can find evidence that mechanisms affecting model behaviour are observed in the real climate system. This is particularly the case for processes key to the climate's sensitivity, such as changes to water vapour and low cloud.

Despite this difference in approach from Chapters 3 and 4, the themes of the analysis in Chapter 5 were similar: I was interested in exploring how the TOA broadband radiation flux co-varied with atmospheric properties, including water vapour and cloud properties. Therefore, aspects of my work in Chapters 3 and 4 provided context for and informed my analysis in Chapter 5.

While relative warming of SSTs was the driver of the effects I studied in Chapter 5, it was the intermediary changes in clouds, temperature and humidity which directly influenced changes in the TOA radiation fluxes. Therefore, a strength of this study was the use of two independent and co-incident satellite products: TOA broadband radiation fluxes, including the window region, from CERES SSF1deg and temperature and humidity profiles from AIRS. This allowed me to interpret different lines of evidence for the hypothesised mechanism.

The cloud properties I used in this study were limited to cloud fraction at different heights, but this was sufficient to broadly contrast the two regimes and compare with the hypothesised mechanism. When warming was concentrated in regions of strong descent, there was a strong decrease in low cloud, which I linked to the decrease in RSR at the TOA. This broadly agreed with the hypothesised mechanism (Zhou et al., 2016; Ceppi and Gregory, 2017; Andrews and Webb, 2018), and was consistent with the observed link between lower tropospheric stability and low cloud (Wood and Bretherton, 2006). In the contrasting scenario, when there was relative warming in regions of strong ascent, I found an increase in high cloud fraction and a decrease in low cloud fraction. I interpreted the strong

decrease in OLR in these regions as a consequence of more high cloud forming, or an increase in convective cloud. A key finding of this work was that this longwave effect in ascending regions was larger in magnitude than the shortwave effect in descending regions, which was not explicitly discussed in the hypothesis (Andrews and Webb, 2018). While in this study I did not directly compare quantitatively how the observations compare with model output, I discuss this as an avenue for further study in section 6.3.

Another key aspect of Chapter 5 was the vertical distribution of water vapour and how changes in this affects OLR. From a radiation perspective, the window region data from CERES provided further insight than just examination of OLR. For example, the small but statistically significant reduction in clear-sky OLR in ascending regions was due to changes in the non-window region (Fig. 5.4k) counteracting the effects of surface warming in the window region (Fig. 5.4h), pointing towards the importance of the effects of upper-troposphere humidity on clear-sky OLR.

Chapter 3 also touched upon the links between humidity profiles, available from the AMF (Fig. 3.5) and OLR. Comparison of daily relative humidity profiles with 43r1 suggested that there were dry biases between 700-500hPa, and wet biases 500-200hPa. Further to this, when contrasting the correlation coefficients of OLR to upper tropospheric humidity (UTH, defined as the mean relative humidity between 200-500hPa), I found that 43r1 had a far higher degree of co-variability ($r^2 = 0.54$) than the observations ($r^2 = 0.13$). This may be due to observations being intrinsically more 'noisy' than model output, but could warrant further investigation both in reanalysis and for GCMS. For example, it would be interesting to compare the AIRS/CERES data with output from GCMs, especially in light of previous studies indicating GCMs also tend to overestimate UTH with respect to the lower troposphere (Pierce et al., 2006; Po-Chedley and Fu, 2012).

6.2 Discussion of methods used

Having summarised and drawn together the conclusions of this thesis, I now critically discuss the methods I have used and the challenges of using observations and models together.

6.2.1 Different spatial and temporal scales

A key aspect of all three research chapters has been how to appropriately combine observations and model output of varying time and spatial scales, and across different regimes. One potential difficulty has been the combining point measurements from surface stations with area-means from satellite products and model output. While efforts are made to pick locations representative of the wider area, for example the AMF in Niamey, this will inevitably be imperfect. The representativeness of point measurements of wider area means has been the subject of study, for example for DSR (Schwarz et al., 2017), though it is difficult to generalise this to other variables. Despite this, the in-situ measurements from surface stations are often the only true observations available, and it is therefore vital that model and satellite products are validated against them.

A key analysis approach in this thesis has been through defining and contrasting regions or regimes within the larger dataset. In Chapter 4 I contrasted different regions within west Africa, which allowed better attribution of effects to processes such as the west African monsoon. This also allowed me to compare the surface station data to the wider region, which supported the use of point measurements for model evaluation. In Chapter 5, the regions defined were not geographically static in time, but rather shifted on a monthly basis to isolate areas of strong convection and subsidence, as was necessary for the analysis. Splitting data by

time also provided insight: the distinction of wet and dry seasons in Chapters 3 and 4 highlighted contrasting correlations and biases according to season.

6.2.2 Sources of observational uncertainty

Uncertainty is an inherent part of using observational data, arising predominantly from measurement uncertainty and assumptions made in the processing of data products. An important part of my work in this thesis has been to understand how this uncertainty affects my analysis and the conclusions I draw. In Chapter 3, uncertainty estimates of the variables used were provided by the AMF, and by previous studies for GERB/SEVIRI (Ansell et al., 2014). I then propagated them through for use in the multi-variable linear models to give an indication of the linear model's uncertainty. In Chapter 4, my approach was to use the surface data and satellite products to produce a reference range with which to evaluate the models, implicitly taking the different observational processes and instruments into account. I used a different approach to observational uncertainty in Chapter 5: assuming uncertainties to be random, the large-area averages resulted in small measurement uncertainty as it scales with the square root of number of observations used. Therefore, I used the standard error of the mean as my uncertainty estimate instead. This gave an idea of the range of values used across my mean, and gave confidence that my regime definition procedure was selecting points with similar characteristics. Including uncertainty in both variables when performing linear regressions also allowed the regressions to be weighted accordingly.

I discussed one important source of uncertainty in both Chapters 4 and 5 where it was particularly relevant: that of the differences in the definitions of clear-sky radiation fluxes, not only between observations and models but also between different satellite products. In models, the radiation fields are calculated with no

clouds present. For observations, clear-sky radiation fluxes have to be calculated from clear-sky data only, or inferred from neighbouring scenes. For CERES products, clear-sky monthly means are calculated from scenes where cloud fraction is $\leq 1\%$, as determined by MODIS and may therefore differ in number over a month. For the SYN1deg and SSF1deg products this can result in missing data, while for the filled product of EBAF these are inferred from partly cloudy scenes (Loeb et al., 2018). Further to this, selecting only clear-sky scenes introduces a sampling bias, relevant to estimates of CRE and CRF (Allan and Ringer, 2003). There are also differences between CERES and AIRS clear-sky definitions, with the latter adopting a 'cloud-clearing' approach as opposed to clear-sky. As described in Chapter 5, cloud-clearing involves inferring the clear-sky radiance of a cloudy column from adjacent fields of view assuming that the temperature and humidity profiles are the same, and that the same cloud type will have the same radiative effect (Susskind et al., 2003). Again, this may lead to a sampling bias as drier, colder scenes are selected, and may particularly affect the deep convective regions (Wong et al., 2015).

6.2.3 Combining surface products

Constructing a range of references from available surface stations, reanalysis and satellite products with which to evaluate model output was a useful exercise and demonstrated, for example, the close agreement of satellite TOA radiation products over west Africa. However, the range and nature of the data used in Chapter 4 meant that it was difficult to clearly define the metric with which I was evaluating the CMIP5 output particularly at the surface and therefore it was difficult to come to concrete conclusions.

While networks like BSRN and AERONET provide invaluable in-situ data, their use in model evaluation studies such as Chapter 4 comes with considerable

limitations. Missing data, including some gaps of several months, posed a significant problem for analysis. This, and the lack of co-incident data of different variables necessitated using average seasonal cycles. While this did provide some insight and allowed for comparison with coupled model average seasonal cycles, it was difficult to perform more detailed analysis. For example, it would have been interesting to better evaluate the SYN1deg AOD time series against that from AERONET, especially for the subsequent analysis of the co-variability with surface radiation fluxes. Difficulties in missing data and non-overlapping time series highlight how invaluable consistent data sets are, like that from the AMF in Niamey used in Chapter 3. It also demonstrates the benefits of long-term, self-consistent products like that provided by CERES EBAF/SYN1deg. These products are also area-averages over a regular grid, and filled so that there are no missing data points (though of course the assumptions made in this increase the uncertainty in the estimates).

Despite these issues, there are compelling reasons to include in-situ measurements where possible into model evaluation studies, not least because, as discussed in Chapter 2, they provide some of the only 'true' measurements of radiation fluxes and associated variables. In light of my work in Chapter 4, however, I would argue that in cases where direct measurements are scarce and suffer from missing data, it may be more appropriate to use them to evaluate reanalysis or satellite products at their specific time and location, rather than try to use them to evaluate the general patterns of variability in GCMs.

6.2.4 How useful is a multi-model mean?

Another issue raised by the analysis in Chapter 4 is the use of a multi-model mean: specifically, how to interpret it and in what situations it might be useful. A recurring theme in that Chapter was that the multi-model mean was within

the observational range, but the spread of model outputs, as defined by the model range and the standard deviation, was large. While sometimes there were general conclusions which could be drawn, for example the tendency of models to overestimate DSR with respect to the references, it was sometimes clear that the multi-model mean was the result of combining very different model behaviours. While error cancellation between models can be useful for improving climate projections, as discussed by Knutti et al. (2010), it does not address the issue of why the CMIP5 models simulate such different TOA radiation fluxes.

My decision to look at the CMIP5 ensemble behaviour rather than the performance of individual models was partly because of this use of multi-model means in the wider literature, but also because of my aim for a wide-ranging study to look at common behaviours. However, the aspects of Chapter 4 which yielded better defined conclusions were when I asked more specific questions: for example, by probing whether a subset of models with interactive aerosol schemes improved estimates of DSR.

Finally, this thesis has relied on model output freely available from reanalyses such as ERA-Interim and GCMs such as those submitted to CMIP5. While exploiting these resources rather than running model experiments to study model behaviour is undeniably time efficient, there are some limitations. For example, in Chapter 3, it was difficult to disentangle the competing effects of surface heating, ground heat storage and turbulent heat fluxes in driving the discrepancy in ULR in the observations and 43r1. Experimenting with different model set-ups, for example by changing the skin temperature or shortwave absorption of the surface, could perhaps lead to more insight into causes of observation and model differences.

6.3 Further work

The studies in this thesis provide scope for future research, as touched upon in my discussion above. As a final section, I propose some areas of future research based on my work here.

The AMF data I used in Chapter 3 provided an opportunity for a detailed study of surface, TOA and atmospheric variables. However, a consequence of using these data in Chapter 3 is that this analysis is specific to this point, and it is difficult to know to what extent the conclusions would hold under different conditions, even within west Africa. One area for future study could be to contrast the co-variability in water vapour and aerosol observed in Niamey with other regions. For example, it would be interesting to repeat the study in a region which was less affected by the monsoon and the subsequent strong seasonal contrasts in surface albedo, cloudiness and aerosol loading, or more strongly influenced by different types of aerosol. Similarly, there is only one year of data and this study does not address interannual variability. It would also be interesting to know the predictive ability of the linear models constructed, to see, for example, the extent to which the linear models developed using one year of data apply to subsequent years.

Both of these suggestions, however, hinge on the availability of surface station data. The scarcity of surface measurements suggests that re-developing the approach in Chapter 3 to use solely satellite data, validated where possible against in situ measurements, might be more feasible. The linear models for the TOA fluxes were largely based on the satellite products of ice and liquid water path, in-conjunction with AOD and upper tropospheric humidity from the AMF. A further study could perhaps focus on these TOA fluxes, and test the co-variability of the fluxes with other satellite products, not only cloud properties such as ice and liquid water path, but also AOD, water vapour profiles and possibly vegetation indices such as NDVI. This would allow for greater area coverage over longer

time periods, and could therefore be used to contrast different regions and for interannual variability.

Finally, in Chapter 3 I used multi-variable linear models of radiation fluxes which were able to reproduce the observed variability to different degrees of success. Although there is utility in interpreting this first approximation, the relationships between aerosol, cloud and water vapour with radiation fluxes are unlikely to be linear. The limitations of the use of linear regressions for these processes could be explored with radiative transfer calculations, which would allow for more detailed analysis of the physical basis and appropriateness of a linear approximation.

Another interesting question raised by both Chapters 3 and 4 was the contrasting sensitivities in observations, reanalysis and GCMs surface fluxes to changes in water vapour and aerosol loading. In particular, whether aerosols were affecting clear-sky DLR directly or through cloud processes was not clear, and it would be of interest to include cloud properties into a more detailed sensitivity study. The analysis in Chapter 4 was qualitative and broad due to the nature of the study, and it would be interesting to take individual models and study their co-variability between these factors with respect to EBAF/SYN1deg. This could lead to better identification of the links between differences in co-variability and radiative flux bias with respect to EBAF/SYN1deg. Further to this, a more detailed look at how different aerosol schemes compare, for example splitting the models into categories which use a fully interactive scheme, those which incorporate either or both of the first and second aerosol indirect effects, or those which rely on a climatology.

For EBAF/SYN1deg to be used in sensitivity studies, further comparison with observations are needed to understand its utility as a reference. For this, co-incident measurements of clear-sky radiation fluxes, aerosol variables and water vapour would be required. While there are some co-incident AOD and surface

radiation flux measurements available from AERONET in west Africa, as used in Chapter 4, they are of relatively short periods of time and with data gaps. Additionally, as discussed, the water vapour estimates from AERONET differ significantly from those from other methods. In light of these difficulties, a study on the co-variability of clear-sky surface fluxes with aerosol and water vapour in other reanalyses may be a more feasible initial comparison.

Another aspect which may be of interest for further work could be how the co-variability of clear-sky surface radiation fluxes with water vapour or AOD changes over different temporal scales. For example, to what extent the relationships change as the means move from daily, to monthly or annual timescales. A method which takes both the spatial and temporal variability into account, for example empirical orthogonal function analysis, could be of use in identifying dominant modes and linking them to physical processes.

While Chapter 4 showed, consistent with past research, that the ability of GCMs to model the radiation budget of west Africa is significantly affected by the progression of the west African monsoon, it did so qualitatively using a mean annual cycle. It might be of interest to try and quantify the effects of longer or shorter monsoons on aspects which have direct impact on humans. For example, one such question could be what the impact on DSR, integrated over a year, is of a late monsoon onset. This could have implications for modelling of crop growing, or production of solar energy.

Finally, the work in Chapter 5 focused on the local, vertical effects of warming, and did not address the remote effects of relative warming in convective regions (Fig. 5.1b). Further study could focus on the observational evidence of the effect that relative warming in convective regions has on subsidence regions, and whether this is consistent with the hypothesised increase in inversion strength and low cloud. This could potentially be done using a similar method of defining convective and

subsidence regions to the one presented here, though consideration of horizontal motion would be required to properly link the changes in the different regions.

Chapter 5 looked at month-to-month variability, rather than the effects of prolonged relative warming in the different regimes. A question raised by this analysis is how changes in relative SST warming might evolve over time, and the implications for temperature, humidity and clouds for prolonged warming. For this, possible future research could make use of observations, reanalysis and model output. There are longer-term cloud and radiation products available (for example the European Space Agency's Climate Change Initiative products), which could be used with reanalysis to increase the period examined from 14 years to ∼30 years. This period may allow for identification of a period when there was prolonged relative heating in winter ascending or descending regions, which would make an interesting comparison to the month-to-month analysis here.

If periods of prolonged warming in regions of either strong convection or subsidence can be identified, this would raise a number of interesting questions. In particular, if subsidence regions are subject to prolonged, relative SST warming, what are the impacts on the stability of the lower troposphere and the inversion strength, and how to these scale with the duration of the relative warming? Similarly, if SSTs in convective regions relatively warm for extended periods, how does this impact subsidence regions, and how does this scale with the duration of the warming? Including evolution over time in the analysis could give a better idea of the potential impacts of different future warming scenarios.

While the work here has examined monthly means, as sampled by AIRS and CERES at their overpass times of 13:30, there are strong dirunal cycles in the atmospheric temperature and humidity, clouds and radiation. These have not been studied here, but it would be of interest to explore the effects of relative SST warming on the dirunal cycle, and how these relate to the monthly means. Study

of this would require use of reanalysis for higher frequency atmospheric profile information, which could perhaps be used in conjunction with other CERES radiation products, such as SYN1deg.

Finally, it would also be of interest to know to what extent GCMs simulate the same relationships, for example between UTH, lower tropospheric stability and SST warming, when subsetted and analysed in the same way as the observational data in Chapter 5. It may be possible to quantify these relationships, and use them in conjunction with the ECS values of the individual models, which could have interesting applications for constraining sensitivity estimates with observations. A method such as the one used by Fasullo and Trenberth (2012), which showed a relationship between model ECS and relative humidity in key parts of the troposphere, could be used, combined with observational values.

The release of GCM output submitted to CMIP6 also opens up avenues for further research. As Zelinka et al. (2020) report, the ECS range from CMIP6 has widened from CMIP5, now at 1.8–5.6K, linked to changes in low cloud. Further study could compare the responses of TOA radiation budget, cloud and atmospheric water vapour to patterns in SST warming in both CMIP5 and CMIP6 output, as well as observations.

References

J. O. Adejuwon and T. O. Odekunle. Variability and the severity of the 'little dry season' in southwestern Nigeria. *Journal of Climate*, 19(3):483–493, 2006. doi: 10.1175/JCLI3642.1.

A. Agustí-Panareda, A. Beljaars, M. Ahlgrimm, G. Balsamo, O. Bock, R. Forbes, A. Ghelli, F. Guichard, M. Köhler, R. Meynadier, and J.-J. Morcrette. The ECMWF re-analysis for the AMMA observational campaign. *Quarterly Journal of the Royal Meteorological Society*, 136(651):1457–1472, 2010. doi: 10.1002/qj.662.

C. D. Ahrens. *Meteorology Today: An Introduction to Weather, Climate, And the Environment*. Thomson Brooks/Cole, 8th edition, 2007.

B. A. Albrecht. Aerosols, cloud microphysics, and fractional cloudiness. *Science*, 245(4923):1227–1230, 1989. doi: 10.1126/science.245.4923.1227.

R. P. Allan. Combining satellite data and models to estimate cloud radiative effect at the surface and in the atmosphere. *Meteorological Applications*, 18(3): 324–333, 2011. doi: 10.1002/met.285.

R. P. Allan and M. A. Ringer. Inconsistencies between satellite estimates of longwave cloud forcing and dynamical fields from reanalyses. *Geophysical Research Letters*, 30(9), 2003. doi: 10.1029/2003GL017019.

R. P. Allan, K. P. Shine, A. Slingo, and J. A. Pamment. The dependence of clear-sky outgoing long-wave radiation on surface temperature and relative humidity. *Quarterly Journal of the Royal Meteorological Society*, 125(558): 2103–2126, 1999. doi: 10.1002/qj.49712555809.

T. Andrews and M. J. Webb. The dependence of global cloud and lapse rate feedbacks on the spatial structure of tropical Pacific warming. *Journal of Climate*, 31(2):641–654, 2018. doi: 10.1175/JCLI-D-17-0087.1.

T. Andrews, J. M. Gregory, M. J. Webb, and K. E. Taylor. Forcing, feedbacks and climate sensitivity in CMIP5 coupled atmosphere-ocean climate models. *Geophysical Research Letters*, 39(9), 2012. doi: 10.1029/2012GL051607.

T. Andrews, J. M. Gregory, and M. J. Webb. The dependence of radiative forcing and feedback on evolving patterns of surface temperature change in climate models. *Journal of Climate*, 28(4):1630–1648, 2015. doi: 10.1175/JCLI-D-14-00545.1.

C. Ansell, H. E. Brindley, Y. Pradhan, and R. Saunders. Mineral dust aerosol net direct radiative effect during GERBILS field campaign period derived from SEVIRI and GERB. *Journal of Geophysical Research: Atmospheres*, 119(7): 4070–4086, 2014. doi: 10.1002/2013JD020681.

K. C. Armour. Energy budget constraints on climate sensitivity in light of inconstant climate feedbacks. *Nature Climate Change*, 7:331–335, 2017. doi: 10.1038/nclimate3278.

K. C. Armour, C. M. Bitz, and G. H. Roe. Time-varying climate sensitivity from regional feedbacks. *Journal of Climate*, 26(13):4518–4534, 2013. doi: 10.1175/JCLI-D-12-00544.1.

H. H. Aumann, M. T. Chahine, C. Gautier, M. D. Goldberg, E. Kalnay, L. M. McMillin, H. Revercomb, P. W. Rosenkranz, W. L. Smith, D. H. Staelin, L. L. Strow, and J. Susskind. AIRS/AMSU/HSB on the Aqua mission: design, science objectives, data products, and processing systems. *IEEE Transactions on Geoscience and Remote Sensing*, 41(2):253–264, 2003. doi: 10.1109/TGRS.2002.808356.

J. R. Banks, H. E. Brindley, M. Hobby, and J. H. Marsham. The daytime cycle in dust aerosol direct radiative effects observed in the central Sahara during the Fennec campaign in June 2011. *Journal of Geophysical Research Atmospheres*, 119(24):13861–13876, 2014. doi: 10.1002/2014JD022077.

B. R. Barkstrom. The earth radiation budget experiment (erbe). *Bulletin of the American Meteorological Society*, 65(11):1170–1185, 1984. doi: 10.1175/1520-0477(1984)065<1170:TERBE>2.0.CO;2.

P. Bechtold, N. Semane, P. Lopez, J.-P. Chaboureau, Beljaars A., and N. Bormann. Representing equilibrium and nonequilibrium convection in large-scale models. *Journal of the Atmospheric Sciences*, 71(2):734–753, 2014. doi: 10.1175/JAS-D-13-0163.1.

N. Bellouin, J. Quaas, E. Gryspeerdt, S. Kinne, P. Stier, D. Watson-Parris, O. Boucher, K. S. Carslaw, M. Christensen, A.-L. Daniau, J.-L. Dufresne, G. Feingold, S. Fiedler, P. Forster, A. Gettelman, J. M. Haywood, U. Lohmann, F. Malavelle, T. Mauritsen, D. T. McCoy, G. Myhre, J. Mlmenstdt, D. Neubauer, A. Possner, M. Rugenstein, Y. Sato, M. Schulz, S. E. Schwartz, O. Sourdeval, T. Storelvmo, V. Toll, D. Winker, and B. Stevens. Bounding global aerosol radiative forcing of climate change. *Reviews of Geophysics*, 58 (1), 2020. doi: 10.1029/2019RG000660.

O. Bellprat and F. Doblas-Reyes. Attribution of extreme weather and climate events overestimated by unreliable climate simulations. *Geophysical Research Letters*, 43(5):2158–2164, 2016. doi: 10.1002/2015GL067189.

N. Benas, S. Finkensieper, M. Stengel, G.-J. van Zadelhoff, T. Hanschmann, R. Hollmann, and J. F. Meirink. The MSG-SEVIRI-based cloud property data record CLAAS-2. *Earth System Science Data*, 9(2):415–434, 2017. doi: 10.5194/essd-9-415-2017.

P. Berrisford, D.P. Dee, P. Poli, R. Brugge, K. Fielding, M. Fuentes, P.W. Kållberg, S. Kobayashi, S. Uppala, and A. Simmons. The ERA-Interim archive version 2.0, 2011. URL `https://www.ecmwf.int/node/8174`.

S. Bony and J.-L. Dufresne. Marine boundary layer clouds at the heart of tropical cloud feedback uncertainties in climate models. *Geophysical Research Letters*, 32(20), 2005. doi: 10.1029/2005GL023851.

O. Boucher, D. Randall, P. Artaxo, C. Bretherton, G. Feingold, P. Forster, V.-M. Kerminen, Y. Kondo, H. Liao, U. Lohmann, P. Rasch, S.K. Satheesh, S. Sherwood, B. Stevens, and X.Y. Zhang. Chapter 7: Clouds and aerosols. *Climate Change 2013: The Physical Science Basis. Contribution of Working Group I to the Fifth Assessment Report of the Intergovernmental Panel on Climate Change*, page 571658, 2013. doi: 10.1017/CBO9781107415324.016.

F. Brient and T. Schneider. Constraints on climate sensitivity from space-based measurements of low-cloud reflection. *Journal of Climate*, 29(16):5821–5835, 2016. doi: 10.1175/JCLI-D-15-0897.1.

H. E. Brindley. Estimating the top-of-atmosphere longwave radiative forcing due to Saharan dust from satellite observations over a west African surface site. *Atmospheric Science Letters*, 8(3):74–79, 2007. doi: 10.1002/asl.155.

H. E. Brindley and J. E. Harries. The impact of far I.R. absorption on clear sky greenhouse forcing: sensitivity studies at high spectral resolution. *Journal of Quantitative Spectroscopy and Radiative Transfer*, 60(2):151 – 180, 1998. doi: https://doi.org/10.1016/S0022-4073(97)00152-0.

R. J. Brindley, H. E.and Bantges. The spectral signature of recent climate change. *Current Climate Change Reports*, 2(3):112–126, 2016. doi: 10.1007/s40641-016-0039-5.

M. Calisto, D. Folini, M. Wild, and L. Bengtsson. Cloud radiative forcing intercomparison between fully coupled CMIP5 models and CERES satellite data. *Annales Geophysicae*, 32(7):793–807, 2014. doi: 10.5194/angeo-32-793-2014.

G. Caniaux, H. Giordani, J.-L. Redelsperger, F. Guichard, E. Key, and M. Wade. Coupling between the Atlantic cold tongue and the West African monsoon in boreal spring and summer. *Journal of Geophysical Research: Oceans*, 116(C4), 2011. doi: 10.1029/2010JC006570.

P. Ceppi and J. M. Gregory. Relationship of tropospheric stability to climate sensitivity and Earth's observed radiation budget. *Proceedings of the National Academy of Sciences*, 2017. doi: 10.1073/pnas.1714308114.

R. D. Cess, M. Zhang, B. A. Wielicki, D. F. Young, X.-L. Zhou, and Y. Nikitenko. The influence of the 1998 El Niño upon cloud-radiative forcing over the pacific warm pool. *Journal of Climate*, 14(9):2129–2137, 2001. doi: 10.1175/1520-0442(2001)014<2129:TIOTEN>2.0.CO;2.

M. T. Chahine, T. S. Pagano, H. H. Aumann, R. Atlas, C. Barnet, J. Blaisdell, L. Chen, M. Divakarla, E. J. Fetzer, M. Goldberg, C. Gautier, S. Granger, S. Hannon, F. W. Irion, R. Kakar, E. Kalnay, B. H. Lambrigtsen, S.-Y. Lee, J. Le Marshall, W. W. Mcmillan, L. Mcmillin, E. T. Olsen, H. Revercomb, P. Rosenkranz, W. L. Smith, D. Staelin, L. L. Strow, J. Susskind, D. Tobin, W. Wolf, and L. Zhou. AIRS: Improving weather forecasting and providing new data on greenhouse gases. *Bulletin of the American Meteorological Society*, 87 (7):911–926, 2006. doi: 10.1175/BAMS-87-7-911.

T. Chen, W. B. Rossow, and Y. Zhang. Radiative effects of cloud-type variations. *Journal of Climate*, 13(1):264–286, 2000. doi: 10.1175/1520-0442(2000)013<0264:REOCTV>2.0.CO;2.

N. Clerbaux. Algorithm theoretical basis document top of atmosphere radiation SEVIRI/GERB data record. *EUMETSAT Satellite Application Facility on Climate Monitoring*, 2016. URL `https://www.cmsaf.eu/`.

N. Clerbaux, M. Urbain, A. Ipe, E. Baudrez, A. Velazquez-Blazquez, T. Akkermans, R. Hollmann, P. Fuchs, N. Selbach, and M. Werscheck. CM SAF TOA Radiation GERB/SEVIRI Data Record - Edition 2. *Satellite Application Facility on Climate Monitoring*, 2017. URL `https://www.cmsaf.eu/`.

W. D. Collins, P. J. Rasch, B. E. Eaton, B. V. Khattatov, J.-F. Lamarque, and C. S. Zender. Simulating aerosols using a chemical transport model with assimilation of satellite aerosol retrievals: Methodology for INDOEX. *Journal of Geophysical Research: Atmospheres*, 106(D7):7313–7336, 2001. doi: 10.1029/2000JD900507.

W. D. Collins, V. Ramaswamy, M. D. Schwarzkopf, Y. Sun, R. W. Portmann, Q. Fu, S. E. B. Casanova, J.-L. Dufresne, D. W. Fillmore, P. M. D. Forster, V. Y. Galin, L. K. Gohar, W. J. Ingram, D. P. Kratz, M.-P. Lefebvre, J. Li, P. Marquet, V. Oinas, Y. Tsushima, T. Uchiyama, and W. Y. Zhong. Radiative

forcing by well-mixed greenhouse gases: Estimates from climate models in the Intergovernmental Panel on Climate Change (IPCC) Fourth Assessment Report (AR4). *Journal of Geophysical Research: Atmospheres*, 111(D14), 2006. doi: 10.1029/2005JD006713.

R. A. Colman and B. J. McAvaney. On tropospheric adjustment to forcing and climate feedbacks. *Climate Dynamics*, 36(9):1649, 2011. doi: 10.1007/s00382-011-1067-4.

R. E. Comer, A. Slingo, and R. P. Allan. Observations of the diurnal cycle of outgoing longwave radiation from the Geostationary Earth Radiation Budget instrument. *Geophysical Research Letters*, 34(2), 2007. doi: 10.1029/2006GL028229.

K. H. Cook and E. K. Vizy. Coupled model simulations of the West African Monsoon System: Twentieth- and twenty-first-century simulations. *Journal of Climate*, 19(15):3681–3703, 2006. doi: 10.1175/JCLI3814.1.

D. P. Dee, S. M. Uppala, A. J. Simmons, P. Berrisford, P. Poli, S. Kobayashi, U. Andrae, M. A. Balmaseda, G. Balsamo, P. Bauer, P. Bechtold, A. C. M. Beljaars, L. van de Berg, J. Bidlot, N. Bormann, C. Delsol, R. Dragani, M. Fuentes, A. J. Geer, Haimberger L., Healy S. B., Hersbach H., E. V. Hlm, L. Isaksen, P. Kllberg, M. Khler, M. Matricardi, A. P. McNally, B. M. MongeSanz, J.J. Morcrette, B.K. Park, C. Peubey, P. de Rosnay, C. Tavolato, J.N. Thpaut, and F. Vitart. The ERAInterim reanalysis: configuration and performance of the data assimilation system. *Quarterly Journal of the Royal Meteorological Society*, 137(656):553–597, 2011. doi: 10.1002/qj.828.

S. Dewitte, L. Gonzalez, N. Clerbaux, A. Ipe, C. Bertrand, and B. De Paepe. The Geostationary Earth Radiation Budget Edition 1 data processing algorithms. *Advances in Space Research*, 41(11):1906–1913, 2008. doi: 10.1016/j.asr.2007.07.042.

D. R. Doelling, N. G. Loeb, D. F. Keyes, M. L. Nordeen, D. Morstad, C. Nguyen, B. A. Wielicki, D. F. Young, and M. Sun. Geostationary enhanced temporal interpolation for CERES flux products. *Journal of Atmospheric and Oceanic Technology*, 30(6):1072–1090, 2013. doi: 10.1175/JTECH-D-12-00136.1.

D. R. Doelling, M. Sun, L. T. Nguyen, M. L. Nordeen, C. O. Haney, D. F. Keyes, and P. E. Mlynczak. Advances in geostationary-derived longwave fluxes for the CERES synoptic (SYN1deg) product. *Journal of Atmospheric and Oceanic Technology*, 33(3):503–521, 2016. doi: 10.1175/JTECH-D-15-0147.1.

E. K. Dolinar, X. Dong, B. Xi, J. H. Jiang, and H. Su. Evaluation of CMIP5 simulated clouds and TOA radiation budgets using NASA satellite observations. *Climate Dynamics*, 44(7-8):2229–2247, 2015. doi: 10.1007/s00382-014-2158-9.

C. M. Dunning, E. C. L. Black, and R. P. Allan. The onset and cessation of seasonal rainfall over Africa. *Journal of Geophysical Research: Atmospheres*, 121(19):11,405–11,424, 2016. doi: 10.1002/2016JD025428.

C. M. Dunning, R. P. Allan, and E. Black. Identification of deficiencies in seasonal rainfall simulated by CMIP5 climate models. *Environmental Research Letters*, 12(11):114001, 2017. doi: 10.1088/1748-9326/aa869e.

J. T. Fasullo and K. E. Trenberth. A less cloudy future: The role of subtropical subsidence in climate sensitivity. *Science*, 338(6108):792–794, 2012. doi: 10.1126/science.1227465.

B. Fildier and W.D. Collins. Origins of climate model discrepancies in atmospheric shortwave absorption and global precipitation changes. *Geophysical Research Letters*, 42(20), 2015. doi: 10.1002/2015GL065931.

G. Flato, J. Marotzke, B. Abiodun, P. Braconnot, S.C. Chou, W. Collins, P. Cox, F. Driouech, S. Emori, V. Eyring, C. Forest, P. Gleckler, E. Guilyardi, C. Jakob, V. Kattsov, C. Reason, and M. Rummukainen. Chapter 9: Evaluation of Climate Models. *Climate Change 2013: The Physical Science Basis. Contribution of Working Group I to the Fifth Assessment Report of the Intergovernmental Panel on Climate Change*, pages 741–866, 2013. doi: 10.1017/CBO9781107415324.

S. M. Freidenreich and V. Ramaswamy. Analysis of the biases in the downward shortwave surface flux in the GFDL CM2.1 general circulation model. *Journal of Geophysical Research: Atmospheres*, 116(D8), 2011. doi: 10.1029/2010JD014930.

W. L. Gates. AMIP: The Atmospheric Model Intercomparison Project. *Bulletin of the American Meteorological Society*, 73(12):1962–1970, 1992. doi: 10.1175/1520-0477(1992)073<1962:ATAMIP>2.0.CO;2.

F. Glassmeier, A. Possner, B. Vogel, H. Vogel, and U. Lohmann. A comparison of two chemistry and aerosol schemes on the regional scale and the resulting impact on radiative properties and liquid- and ice-phase aerosol–cloud interactions. *Atmospheric Chemistry and Physics*, 17(14):8651–8680, 2017.

P. J. Gleckler, K. E. Taylor, and C. Doutriaux. Performance metrics for climate models. *Journal of Geophysical Research: Atmospheres*, 113(D6), 2008. doi: 10.1029/2007JD008972.

L. J. Gray, J. Beer, M. Geller, J. D. Haigh, M. Lockwood, K. Matthes, U. Cubasch, D. Fleitmann, G. Harrison, L. Hood, J. Luterbacher, G. A. Meehl, D. Shindell, B. van Geel, and W. White. Solar influences on climate. *Reviews of Geophysics*, 48(4), 2010. doi: 10.1029/2009RG000282.

J. M. Gregory, W. J. Ingram, M. A. Palmer, G. S. Jones, P. A. Stott, R. B. Thorpe, J. A. Lowe, T. C. Johns, and K. D. Williams. A new method for diagnosing radiative forcing and climate sensitivity. *Geophysical Research Letters*, 31(3), 2004. doi: 10.1029/2003GL018747.

J. J. Gristey, J. C. Chiu, R. J. Gurney, C. J. Morcrette, P. G. Hill, J. E. Russell, and H. E. Brindley. Insights into the diurnal cycle of global earth outgoing radiation using a numerical weather prediction model. *Atmospheric Chemistry and Physics*, 18(7):5129–5145, 2018.

E. Gryspeerdt, J. Quaas, and N. Bellouin. Constraining the aerosol influence on cloud fraction. *Journal of Geophysical Research: Atmospheres*, 121(7):3566–3583, 2016. doi: 10.1002/2015JD023744.

M. Z. Hakuba, D. Folini, A. Sanchez-Lorenzo, and M. Wild. Spatial representativeness of ground-based solar radiation measurements - extension to the full Meteosat disk. *Journal of Geophysical Research: Atmospheres*, 119(20):11,760–11,771, 2014. doi: 10.1002/2014JD021946.

L. Hannak, P. Knippertz, A. H. Fink, A. Kniffka, and G. Pante. Why do global climate models struggle to represent low-level clouds in the West African summer monsoon? *Journal of Climate*, 30(5):1665–1687, 2017. doi: 10.1175/JCLI-D-16-0451.1.

J. E. Harries, J. E. Russell, J. A. Hanafin, H. Brindley, J. Futyan, J. Rufus, S. Kellock, G. Matthews, R. Wrigley, A. Last, J. Mueller, R. Mossavati, J. Ashmall, E. Sawyer, D. Parker, M. Caldwell, P. M. Allan, A. Smith, M. J. Bates, B. Coan, B. C. Stewart, D. R. Lepine, L. A. Cornwall, D. R. Corney, M. J. Ricketts, D. Drummond, D. Smart, R. Cutler, S. Dewitte, N. Clerbaux, L. Gonzalez, A. Ipe, C. Bertrand, A. Joukoff, D. Crommelynck, N. Nelms, D. T. Llewellyn-Jones, G. Butcher, G. L. Smith, Z. P. Szewczyk, P. E. Mlynczak, A. Slingo, R. P. Allan, and M. A. Ringer. The Geostationary Earth Radiation Budget Project. *Bulletin of the American Meteorological Society*, 86(7):945–960, 2005. doi: 10.1175/BAMS-86-7-945.

L. Harrison, J. Michalsky, and J. Berndt. Automated multifilter rotating shadowband radiometer: an instrument for optical depth and radiation measurements. *Applied Optics*, 33(22):5118–5125, 1994. doi: 10.1364/AO.33.005118.

D. J Hartmann, A. M. G. Klein Tank, M. Rusticucci, L. V. Alexander, S. Brönnimann, Y. A.-R. Charabi, F. J. Dentener, E. J. Dlugokencky, D. R. Easterling, A. Kaplan, B. J. Soden, P. W. Thorne, M. Wild, and P. Zhai. Chapter 2: Observations: Atmosphere and Surface. *Climate Change 2013: The Physical Science Basis. Contribution of Working Group I to the Fifth Assessment Report of the Intergovernmental Panel on Climate Change*, pages 159–254, 2013. doi: 10.1017/CBO9781107415324.008.

D. L. Hartmann. Chapter 3 Atmospheric Radiative Transfer and Climate. In *Global Physical Climatology*, volume 56 of *International Geophysics*, pages 40 – 80. Academic Press, 1994. doi: 10.1016/S0074-6142(08)60560-4.

D. L. Hartmann, M. E. Ockert-Bell, and M. L. Michelsen. The effect of cloud type on earth's energy balance: Global analysis. *Journal of Climate*, 5(11):1281–1304, 1992. doi: 10.1175/1520-0442(1992)005<1281:TEOCTO>2.0.CO;2.

D. L. Hartmann, L. A. Moy, and Q. Fu. Tropical convection and the energy balance at the top of the atmosphere. *Journal of Climate*, 14(24):4495–4511, 2001. doi: 10.1175/1520-0442(2001)014<4495:TCATEB>2.0.CO;2.

S. Hasternath and P. Lamb. Some aspects of the circulation and climate over the eastern equatorial Atlantic. *Monthly Weather Review*, 105:1019–1023, 1977. doi: 10.1175/1520-0493(1977)105<1019:SAOCAC>2.0.CO;2.

J. M. Haywood, R. P. Allan, I. Culverwell, T. Slingo, S. Milton, J. Edwards, and N. Clerbaux. Can desert dust explain the outgoing longwave radiation anomaly over the Sahara during July 2003? *Journal of Geophysical Research: Atmospheres*, 110(D5), 2005. doi: 10.1029/2004JD005232.

I. M. Held and B. J. Soden. Water vapor feedback and global warming. *Annual Review of Energy and the Environment*, 25(1):441–475, 2000. doi: 10.1146/annurev.energy.25.1.441.

P. G. Hill, R. P. Allan, J. C. Chiu, and T. H. M. Stein. A multisatellite climatology of clouds, radiation, and precipitation in southern West Africa and comparison to climate models. *Journal of Geophysical Research: Atmospheres*, 121(18): 10,857–10,879, 2016. doi: 10.1002/2016JD025246.

R. J. Hogan and A. Bozzo. Mitigating errors in surface temperature forecasts using approximate radiation updates. *Journal of Advances in Modeling Earth Systems*, 7(2):836–853, 2015. doi: 10.1002/2015MS000455.

B. N. Holben, T. F. Eck, I. Slutsker, D. Tanr, J. P. Buis, A. Setzer, E. Vermote, J. A. Reagan, Y. J. Kaufman, T. Nakajima, F. Lavenu, I. Jankowiak, and A. Smirnov. AERONETA federated instrument network and data archive for aerosol characterization. *Remote Sensing of Environment*, 66(1):1 – 16, 1998. doi: 10.1016/S0034-4257(98)00031-5.

B. T. Johnson, S. R. Osborne, J. M. Haywood, and M. A. J. Harrison. Aircraft measurements of biomass burning aerosol over West Africa during DABEX. *Journal of Geophysical Research: Atmospheres*, 113(23):1–15, 2008. doi: 10.1029/2007JD009451.

S. Kato, N. G. Loeb, D. A. Rutan, F. G. Rose, S. Sun-Mack, and Y. Miller, W. F.and Chen.

S. Kato, N. G. Loeb, F. G. Rose, D. R. Doelling, D. A. Rutan, T. E. Caldwell, L. Yu, and R. A. Weller. Surface irradiances consistent with CERES-derived top-of-atmosphere shortwave and longwave irradiances. *Journal of Climate*, 26 (9):2719–2740, 2013. doi: 10.1175/JCLI-D-12-00436.1.

S. Kato, F. G. Rose, D. A. Rutan, T. J. Thorsen, N. G. Loeb, D. R. Doelling, X. Huang, W. L. Smith, W. Su, and S.-H. Ham. Surface irradiances of Edition 4.0 Clouds and the Earths Radiant Energy System (CERES) Energy Balanced and Filled (EBAF) data product. *Journal of Climate*, 31(11):4501–4527, 2018. doi: 10.1175/JCLI-D-17-0523.1.

P. Kishore, M. Venkat Ratnam, S. P. Namboothiri, I. Velicogna, G. Basha, J. H. Jiang, K. Igarashi, S. V. B. Rao, and V. Sivakumar. Global (50S50N) distribution of water vapor observed by COSMIC GPS RO: Comparison with GPS radiosonde, NCEP, ERA-Interim, and JRA-25 reanalysis data sets. *Journal of Atmospheric and Solar-Terrestrial Physics*, 73(13):1849 – 1860, 2011. doi: https://doi.org/10.1016/j.jastp.2011.04.017.

P. Knippertz, A. H. Fink, R. Schuster, J. Trentmann, J. M. Schrage, and C. Yorke. Ultralow clouds over the southern West African monsoon region. *Geophysical Research Letters*, 38(21), 11 2011. ISSN 1944-8007. doi: 10.1029/2011GL049278.

P. Knippertz, H. Coe, J. C. Chiu, M. J. Evans, A. H. Fink, N. Kalthoff, C. Liousse, C. Mari, R. P. Allan, B. Brooks, S. Danour, C. Flamant, O. O. Jegede, F. Lohou, and J. H. Marsham. The DACCIWA Project: DynamicsAerosolChemistryCloud Interactions in West Africa. *Bulletin of the American Meteorological Society*, 96(9):1451–1460, 2015a. doi: 10.1175/BAMS-D-14-00108.1.

P. Knippertz, M. J. Evans, P. R. Field, A. H. Fink, C. Liousse, and J. H. Marsham. The possible role of local air pollution in climate change in West Africa. *Nature Climate Change*, 5(9):815–822, 2015b.

R. Knutti and G. C. Hegerl. The equilibrium sensitivity of the earth's temperature to radiation changes. *Nature Geoscience*, 1:735–734, 2008. doi: 10.1038/ngeo337.

R. Knutti, R. Furrer, C. Tebaldi, J. Cermak, and G. A. Meehl. Challenges in combining projections from multiple climate models. *Journal of Climate*, 23 (10):2739–2758, 2010. doi: 10.1175/2009JCLI3361.1.

R. Knutti, M. A. A. Rugenstein, and G. C. Hegerl. Beyond equilibrium climate sensitivity. *Nature Geoscience*, 10:727 – 736, 2017. doi: 10.1038/ngeo3017.

T. S. L'Ecuyer. Earth's energy balance. *International Encyclopedia of Geography*, pages 1–7, 2017. doi: 10.1002/9781118786352.wbieg1132.

T. S. L'Ecuyer, Y. Hang, A. V. Matus, and Z. Wang. Reassessing the effect of cloud type on Earth's energy balance in the age of active spaceborne observations. Part I: top of atmosphere and surface. *Journal of Climate*, 32: 6197–6217, 2019. doi: 10.1175/JCLI-D-18-0753.1.

M. Lélé and P. J. Lamb. Variability of the Intertropical Front (ITF) and rainfall over the West African Sudan-Sahel zone. *Journal of Climate*, 23(14):3984–4004, 2010. doi: 10.1175/2010JCLI3277.1.

J.-L. F. Li, D. E. Waliser, G. Stephens, S. Lee, T. L'Ecuyer, S. Kato, N. Loeb, and H.-Y. Ma. Characterizing and understanding radiation budget biases in CMIP3/CMIP5 GCMs, contemporary GCM, and reanalysis. *Journal of Geophysical Research: Atmospheres*, 118(15):8166–8184, 2013. doi: 10.1002/jgrd.50378.

N. G. Loeb and N. Manalo-Smith. Top-of-atmosphere direct radiative effect of aerosols over global oceans from merged CERES and MODIS observations. *Journal of Climate*, 18(17):3506–3526, 2005. doi: 10.1175/JCLI3504.1.

N. G. Loeb, K. J. Priestley, D. P. Kratz, E. B. Geier, R. N. Green, B. A. Wielicki, P. O'Rawe Hinton, and S. K. Nolan. Determination of unfiltered radiances from the Clouds and the Earth's Radiant Energy System Instrument. *Journal of Applied Meteorology*, 40(4):822835, 2001. doi: 10.1175/1520-0450(2001)0402.0.CO;2.

N. G. Loeb, N. Manalo-Smith, S. Kato, W. F. Miller, S. K. Gupta, P. Minnis, and B. A. Wielicki. Angular distribution models for top-of-atmosphere radiative flux estimation from the Clouds and the Earth's Radiant Energy System instrument on the Tropical Rainfall Measuring Mission satellite. Part I: Methodology. *Journal of Applied Meteorology*, 42(2):240–265, 2003. doi: 10.1175/1520-0450(2003)042<0240:ADMFTO>2.0.CO;2.

N. G. Loeb, B. A. Wielicki, F. G. Rose, and D. R. Doelling. Variability in global top-of-atmosphere shortwave radiation between 2000 and 2005. *Geophysical Research Letters*, 34(3), 2007. doi: 10.1029/2006GL028196.

N. G. Loeb, B. A. Wielicki, D. R. Doelling, G. L. Smith, D. F. Keyes, S. Kato, N. Manalo-Smith, and T. Wong. Toward optimal closure of the Earth's top-of-atmosphere radiation budget. *Journal of Climate*, 22(3):748766, 2009. doi: 10.1175/2008JCLI2637.1.

N. G. Loeb, W.and Wong T. Kato, S.and Su, D. R.and Norris J. R. Rose, F. G.and Doelling, and X. Huang. Advances in understanding top-of-atmosphere radiation variability from satellite observations. *Surveys in Geophysics*, 33(3): 359–385, 2012. doi: 10.1007/s10712-012-9175-1.

N. G. Loeb, D. R. Doelling, H. Wang, W. Su, C. Nguyen, J. G. Corbett, L. Liang, C. Mitrescu, F. G. Rose, and S. Kato. Clouds and the Earths Radiant Energy System (CERES) Energy Balanced and Filled (EBAF) Top-of-Atmosphere (TOA) Edition-4.0 Data Product. *Journal of Climate*, 31(2):895–918, 2018. doi: 10.1175/JCLI-D-17-0208.1.

N. G. Loeb, H. Wang, R. P. Allan, T. Andrews, K. Armour, J. N. S. Cole, J-L Dufresne, P. Forster, A. Gettelman, H. Guo, T. Mauritsen, Y. Ming, D. Paynter, C. Proistosescu, M. F. Stuecker, U. Willén, and K. Wyser. New generation of climate models track recent unprecedented changes in Earth's radiation budget observed by CERES. *Geophysical Research Letters*, 47(5), 2020. doi: 10.1029/2019GL086705. URL `https://agupubs.onlinelibrary.wiley.com/doi/abs/10.1029/2019GL086705`.

C. N. Long and T. P. Ackerman. Identification of clear skies from broadband pyranometer measurements and calculation of downwelling shortwave cloud effects. *Journal of Geophysical Research: Atmospheres*, 105(D12):15609–15626, 2000. doi: 10.1029/2000JD900077.

C. N. Long and D. D. Turner. A method for continuous estimation of clear-sky downwelling longwave radiative flux developed using arm surface measurements. *Journal of Geophysical Research: Atmospheres*, 113(D18), 2008. doi: 10.1029/2008JD009936.

A. Mackie, P. I. Palmer, and H. Brindley. Characterizing energy budget variability at a Sahelian site: a test of NWP model behaviour. *Atmospheric Chemistry and Physics*, 17(24):15095–15119, 2017. doi: 10.5194/acp-17-15095-2017.

J. H. Marsham, D. J. Parker, M. C. Todd, J. R. Banks, H. E. Brindley, L. Garcia-Carreras, A. J. Roberts, and C. L. Ryder. The contrasting roles of water and dust in controlling daily variations in radiative heating of the summertime Saharan heat low. *Atmospheric Chemistry and Physics*, 16(5):3563–3575, 2016. doi: 10.5194/acp-16-3563-2016.

E. R. Martin, C. Thorncroft, and B. B. Booth. The Multidecadal Atlantic SST - Sahel Rainfall Teleconnection in CMIP5 Simulations. *Journal of Climate*, 27 (2):784–806, 2014. doi: 10.1175/JCLI-D-13-00242.1.

M. Maslin and P. Austin. Climate models at their limit? *Nature*, 486:183–184, 2012. doi: 10.1038/486183a.

A. V. Matus and T. S. L'Ecuyer. The role of cloud phase in earth's radiation budget. *Journal of Geophysical Research: Atmospheres*, 122(5):2559–2578, 2017. doi: 10.1002/2016JD025951.

D. T. McCoy, R. Eastman, D. L. Hartmann, and R. Wood. The change in low cloud cover in a warmed climate inferred from AIRS, MODIS, and ERA-Interim. *Journal of Climate*, 30(10):3609–3620, 2017. doi: 10.1175/JCLI-D-15-0734.1.

S. A. McFarlane, J. H. Mather, and T. P. Ackerman. Analysis of tropical radiative heating profiles: A comparison of models and observations. *Journal of Geophysical Research*, 112(D14):1–22, 2007. doi: 10.1029/2006JD008290.

S. A. McFarlane, E. I. Kassianov, J. Barnard, C. Flynn, and T. P. Ackerman. Surface shortwave aerosol radiative forcing during the Atmospheric Radiation Measurement Mobile Facility deployment in Niamey, Niger. *Journal of Geophysical Research: Atmospheres*, 114:1–17, 2009. doi: 10.1029/2008JD010491.

G. A. Meehl, C. Covey, B. McAvaney, M. Latif, and R. J. Stouffer. Overview of the coupled model intercomparison project (CMIP). *Bulletin of the American Meteorological Society*, 86(1), 8 2005. doi: 10.5194/gmd-9-1937-2016.

J. J. Michalsky, J. A. Schlemmer, W. E. Berkheiser, J. L. Berndt, L. C. Harrison, N. S. Laulainen, N. R. Larson, and J. C. Barnard. Multiyear measurements of aerosol optical depth in the Atmospheric Radiation Measurement and Quantitative Links programs. *Journal of Geophysical Research: Atmospheres*, 106(D11):12099–12107, 2001. doi: 10.1029/2001JD900096.

M. A. Miller, V. P. Ghate, and R. K. Zahn. The radiation budget of the West African Sahel and its controls: A perspective from observations and global climate models. *Journal of Climate*, 25(17):5976–5996, 2012. doi: 10.1175/JCLI-D-11-00072.1.

M. J. Miller and A. Slingo. The ARM mobile facility and its first international deployment - measuring radiative flux divergence in west Africa. *Bulletin Of The American Meteorological Society*, 88(8):1229–1244, 2007. doi: 10.1175/BAMS-88-8-1229.

R. L. Miller, A. Slingo, J. C. Barnard, and E. Kassianov. Seasonal contrast in the surface energy balance of the Sahel. *Journal of Geophysical Research Atmospheres*, 114(13):1–19, 2009. doi: 10.1029/2008JD010521.

S. F. Milton, G. Greed, M. E. Brooks, J. Haywood, B. Johnson, R. P. Allan, A. Slingo, and W. M. F. Grey. Modeled and observed atmospheric radiation balance during the West African dry season: Role of mineral dust, biomass burning aerosol, and surface albedo. *Journal of Geophysical Research: Atmospheres*, 113(23):1–24, 2008. doi: 10.1029/2007JD009741.

P. Minnis, S. Sun-Mack, D. F. Young, P. W. Heck, D. P. Garber, Y. Chen, D. A. Spangenberg, R. F. Arduini, Q. Z. Trepte, W. L. Smith, J. K. Ayers, S. C. Gibson, W. F. Miller, G. Hong, V. Chakrapani, Y. Takano, K. Liou,

Y. Xie, and P. Yang. CERES Edition-2 cloud property retrievals ssing TRMM VIRS and Terra and Aqua MODIS dataPart I: Algorithms. *IEEE Transactions on Geoscience and Remote Sensing*, 49(11):4374–4400, 2011. doi: 10.1109/TGRS.2011.2144601.

P. E. Mlynczak, G. L. Smith, and D. R. Doelling. The annual cycle of earth radiation budget from Clouds and the Earths Radiant Energy System (CERES) data. *Journal of Applied Meteorology and Climatology*, 50(12):2490–2503, 2011. doi: 10.1175/JAMC-D-11-050.1.

G. Myhre, D. Shindell, F.-M. Bron, W. Collins, J. Fuglestvedt, J. Huang, D. Koch, J.-F Lamarque, B. Lee, D. Mendoza, T. Nakajima, A. Robock, G. Stephens, T. Takemura, and H. Zhang. Chapter 8: Anthropogenic and Natural Radiative Forcing. *Climate Change 2013: The Physical Science Basis. Contribution of Working Group I to the Fifth Assessment Report of the Intergovernmental Panel on Climate Change*, pages 659–740, 2013. doi: 10.1017/ CBO9781107415324.018.

P. A. O'Gorman and C. A. Muller. How closely do changes in surface and column water vapor follow Clausius Clapeyron scaling in climate change simulations? *Environmental Research Letters*, 5(2):025207, 2010. doi: 10.1088/1748-9326/5/2/025207.

A. Ohmura, E. G. Dutton, B. Forgan, C. Fröhlich, H. Gilgen, H. Hegner, A. Heimo, G. König-Langlo, B. McArthur, G. Müller, R. Philipona, R. Pinker, C. H. Whitlock, K. Dehne, and M. Wild. Baseline Surface Radiation Network (BSRN/WCRP): New precision radiometry for climate research. *Bulletin of the American Meteorological Society*, 79(10):2115–2136, 1998. doi: 10.1175/1520-0477(1998)079<2115:BSRNBW>2.0.CO;2.

J.'Bayo Omotosho. Spatial variation of rainfall in Nigeria during the little dry season. *Atmospheric Research*, 22(2):137 – 147, 1988. doi: 10.1016/0169-8095(88)90004-X.

L. Oreopoulos and E. Mlawer. The Continual Intercomparison of Radiation Codes (CIRC). *Bulletin of the American Meteorological Society*, 91(3):305–310, 2010. doi: 10.1175/2009BAMS2732.1.

N. Oreskes, K. Shrader-Frechette, and K. Belitz. Verification, validation, and confirmation of numerical models in the Earth sciences. *Science*, 263(5147): 641–646, 1994. doi: 10.1126/science.263.5147.641.

D. Pérez-Ramírez, D. N. Whiteman, A. Smirnov, H. Lyamani, B. N. Holben, R. Pinker, M. Andrade, and L. Alados-Arboledas. Evaluation of AERONET precipitable water vapor versus microwave radiometry, GPS, and radiosondes at ARM sites. *Journal of Geophysical Research: Atmospheres*, 119(15):9596–9613, 2014. doi: 10.1002/2014JD021730.

U. Pfeifroth, S. Kothe, R. Müller, J. Trentmann, R. Hollmann, P. Fuchs, and M. Werscheck. Surface radiation data set - Heliosat (SARAH) - edition 2. *Satellite Application Facility on Climate Monitoring*, 2017. doi: 10.5676/EUM_SAF_CM/SARAH/V002.

U. Pfeifroth, A. Sanchez-Lorenzo, V. Manara, J. Trentmann, and R. Hollmann. Trends and variability of surface solar radiation in Europe based on surface- and satellite-based data records. *Journal of Geophysical Research: Atmospheres*, 123(3):1735–1754, 2018. doi: 10.1002/2017JD027418.

D. W. Pierce, T. P. Barnett, E. J. Fetzer, and P. J. Gleckler. Three-dimensional tropospheric water vapor in coupled climate models compared with observations from the AIRS satellite system. *Geophysical Research Letters*, 33(21), 2006. doi: 10.1029/2006GL027060.

S. Po-Chedley and Q. Fu. Discrepancies in tropical upper tropospheric warming between atmospheric circulation models and satellites. *Environmental Research Letters*, 7(4):044018, 2012. doi: 10.1088/1748-9326/7/4/044018.

S. Po-Chedley, K. C. Armour, C. M. Bitz, M. D. Zelinka, B. D. Santer, and Q. Fu. Sources of intermodel spread in the lapse rate and water vapor feedbacks. *Journal of Climate*, 31(8):3187–3206, 2018. doi: 10.1175/JCLI-D-17-0674.1.

Y. Qian, T. J. Yasunari, S. J. Doherty, M. G. Flanner, W. K. M. Lau, J. Ming, H. Wang, M. Wang, S. G. Warren, and R Zhang. Light-absorbing particles in snow and ice: Measurement and modeling of climatic and hydrological impact. *Advances in Atmospheric Sciences*, pages 64–91, 2015. doi: 10.1007/s00376-014-0010-0.

X. Qu, S. A. Hall, A..and Klein, and P. M. Caldwell. The strength of the tropical inversion and its response to climate change in 18 CMIP5 models. *Climate Dynamics*, 45(1):375–396, 2015. doi: 10.1007/s00382-014-2441-9.

D. A. Randall, R. A. Wood, S. Bony, R. Colman, T. Fichefet, J. Fyfe, V. Kattsov, A. Pitman, J. Shukla, J. Srinivasan, R. J. Stouffer, A Sumi, and K. E. Taylor. Chapter 8: Climate models and their evaluation. *Climate Change 2007: The Physical Science Basis. Contribution of Working Group I to the Fourth Assessment Report of the Intergovernmental Panel on Climate Change*, pages 589–662, 2007.

I. Richter, S.-P. Xie, S. K. Behera, T. Doi, and Y. Masumoto. Equatorial Atlantic variability and its relation to mean state biases in CMIP5. *Climate Dynamics*, 42(1):171–188, 2014. doi: 10.1007/s00382-012-1624-5.

D. A. Ridley, C. L. Heald, and J. M. Prospero. What controls the recent changes in African mineral dust aerosol across the Atlantic? *Atmospheric Chemistry and Physics*, 14(11):5735–5747, 2014. doi: 10.5194/acp-14-5735-2014.

R. Roehrig, D. Bouniol, F. Guichard, F. Hourdin, and J.-L. Redelsperger. The present and future of the West African Monsoon: A process-oriented assessment of CMIP5 simulations along the AMMA transect. *Journal of Climate*, 26(17): 6471–6505, 2013. doi: 10.1175/JCLI-D-12-00505.1.

D. A. Rutan, S. Kato, D. R. Doelling, F. G. Rose, L. T. Nguyen, T. E. Caldwell, and N. G. Loeb. CERES synoptic product: Methodology and validation of surface radiant flux. *Journal of Atmospheric and Oceanic Technology*, 32(6): 1121–1143, 2015. doi: 10.1175/JTECH-D-14-00165.1.

J. Schmetz, P. Pili, S. Tjemkes, D. Just, J. Kerkmann, S. Rota, and A. Ratier. Supplement to An Introduction to Meteosat Second Generation (MSG). *Bulletin of the American Meteorological Society*, 83(7):991–991, 2002. doi: 10.1175/BAMS-83-7-Schmetz-1.

K. von Schuckmann, M. D. Palmer, K. E. Trenberth, A. Cazenave, D. Chambers, N. Champollion, J. Hansen, S. A. Josey, N. Loeb, P.-P. Mathieu, B. Meyssignac, and M. Wild. An imperative to monitor Earth's energy imbalance. *Nature Climate Change*, 6(2):138–144, 2016. doi: 10.1038/nclimate2876.

J. Schulz, P. Albert, H.-D. Behr, D. Caprion, H. Deneke, S. Dewitte, B. Dürr, P. Fuchs, A. Gratzki, P. Hechler, R. Hollmann, S. Johnston, K.-G. Karlsson, T. Manninen, R. Müller, M. Reuter, A. Riihelä, R. Roebeling, N. Selbach, A. Tetzlaff, W. Thomas, M. Werscheck, E. Wolters, and A. Zelenka. Operational climate monitoring from space: the EUMETSAT Satellite Application Facility on Climate Monitoring (CM-SAF). *Atmospheric Chemistry and Physics*, 9(5):1687–1709, 2009. doi: 10.5194/acp-9-1687-2009.

M. Schwarz, D. Folini, M. Z. Hakuba, and M. Wild. Spatial representativeness of surface-measured variations of downward solar radiation. *Journal of Geophysical Research: Atmospheres*, 122(24):13,319–13,337, 2017. doi: 10.1002/2017JD027261.

J J Settle, N A Bharmal, G J Robinson, and A Slingo. Sampling uncertainties in surface radiation budget calculations in RADAGAST. *Journal of Geophysical Research: Atmospheres*, 113(D13):D00E02, 2008. doi: 10.1029/2008JD010509.

S. C. Sherwood, S. Bony, and J.-L. Dufresne. Spread in model climate sensitivity traced to atmospheric convective mixing. *Nature*, 505:37–42, 2014. doi: 10.1038/nature12829.

A. Slingo, T. P. Ackerman, R. P. Allan, E. I. Kassianov, S. A. McFarlane, G. J. Robinson, J. C. Barnard, M. A. Miller, J. E. Harries, J. E. Russell, and S. Dewitte. Observations of the impact of a major Saharan dust storm on the atmospheric radiation balance. *Geophysical Research Letters*, 33(24): L24817, 2006. doi: 10.1029/2006GL027869.

A. Slingo, N. A. Bharmal, G. J. Robinson, J. J. Settle, R. P. Allan, H. E. White, P. J. Lamb, M. Issa Ll, D. D. Turner, S. McFarlane, E. Kassianov, J. Barnard, C. Flynn, and M. Miller. Overview of observations from the radagast experiment in Niamey, Niger: Meteorology and thermodynamic variables. *Journal of Geophysical Research: Atmospheres*, 113(D13), 2008. doi: 10.1029/2008JD009909.

A. Slingo, H. E. White, N. A. Bharmal, and G. J. Robinson. Overview of observations from the RADAGAST experiment in Niamey, Niger: 2. Radiative fluxes and divergences. *Journal of Geophysical Research: Atmospheres*, 114 (D13), 2009. doi: 10.1029/2008JD010497.

G. L. Smith, K. J. Priestley, and N. G. Loeb. Clouds and Earth Radiant Energy System: From Design to Data. *IEEE Transactions on Geoscience and Remote Sensing*, 52(3):1729–1738, 2014. doi: 10.1109/TGRS.2013.2253782.

B. J. Soden and I.M. Held. An assessment of climate feedbacks in coupled ocean–atmosphere models. *Journal of Climate*, 19(14):3354–3360, 2006. doi: 10.1175/JCLI3799.1.

B.-J. Sohn, J. Schmetz, R. Stuhlmann, and J.-Y. Lee. Dry bias in satellite-derived clear-sky water vapor and its contribution to longwave cloud radiative forcing. *Journal of Climate*, 19(21):5570–5580, 2006. doi: 10.1175/JCLI3948.1.

R. E. Stanfield, X. Dong, B. Xi, A. Kennedy, A. D. Del Genio, P. Minnis, and J. H. Jiang. Assessment of NASA GISS CMIP5 and post-CMIP5 simulated clouds and TOA radiation budgets using satellite observations. Part I: Cloud fraction and properties. *Journal of Climate*, 27(11):4189–4208, 2014. doi: 10.1175/JCLI-D-13-00558.1.

G. L. Stephens. Cloud feedbacks in the climate system: A critical review. *Journal of Climate*, 18(2):237–273, 2005. doi: 10.1175/JCLI-3243.1.

B. Stevens, S. C. Sherwood, S. Bony, and M. J. Webb. Prospects for narrowing bounds on Earth's equilibrium climate sensitivity. *Earth's Future*, 4(11):512–522, 2016. doi: 10.1002/2016EF000376.

W. Su, J. Corbett, Z. Eitzen, and L. Liang. Next-generation angular distribution models for top-of-atmosphere radiative flux calculation from CERES instruments: methodology. *Atmospheric Measurement Techniques*, 8(2):611–632, 2015. doi: 10.5194/amt-8-611-2015.

B. Sultan and S. Janicot. The West African monsoon dynamics. Part II: The preonset and onset of the summer monsoon. *Journal of Climate*, 16(21):3407–3427, 2003. doi: 10.1175/1520-0442(2003)016<3407:TWAMDP>2.0.CO;2.

J. Susskind, C. D. Barnet, and J. M. Blaisdell. Retrieval of atmospheric and surface parameters from AIRS/AMSU/HSB data in the presence of clouds. *IEEE Transactions on Geoscience and Remote Sensing*, 41(2):390–409, 2003. doi: 10.1109/TGRS.2002.808236.

M. B. Sylla, P. M. Nikiema, P. Gibba, I. Kebe, and N. A. B. Klutse. *Climate Change over West Africa: Recent Trends and Future Projections*, pages 25–40. Springer International Publishing, 2016. ISBN 978-3-319-31499-0. doi: 10.1007/978-3-319-31499-0_3.

K. E. Taylor, R. J. Stouffer, and G. A. Meehl. An overview of CMIP5 and the experiment design. *Bulletin of the American Meteorological Society*, 93(4):485–498, 2012. doi: 10.1175/BAMS-D-11-00094.1.

P. C. Taylor. Tropical outgoing longwave radiation and longwave cloud forcing diurnal cycles from CERES. *Journal of the Atmospheric Sciences*, 69(12):3652–3669, 2012. doi: 10.1175/JAS-D-12-088.1.

I. Tegen, P. Hollrig, M. Chin, I. Fung, D. Jacob, and J. Penner. Contribution of different aerosol species to the global aerosol extinction optical thickness: Estimates from model results. *Journal of Geophysical Research: Atmospheres*, 102(D20):23895–23915, 1997. doi: 10.1029/97JD01864.

B. Tian, E. J. Fetzer, B. H. Kahn, J. Teixeira, E. Manning, and T. Hearty. Evaluating CMIP5 models using AIRS tropospheric air temperature and specific humidity climatology. *Journal of Geophysical Research: Atmospheres*, 118(1):114–134, 2013. doi: 10.1029/2012JD018607.

M. K. Tippett and A. Giannini. Potentially predictable components of african summer rainfall in an SST-forced GCM simulation. *Journal of Climate*, 19(13):3133–3144, 2006. doi: 10.1175/JCLI3779.1.

K. E. Trenberth, J. T. Fasullo, and M. A. Balmaseda. Earth's energy imbalance. *Journal of Climate*, 27(9):3129–3144, 2014. doi: 10.1175/JCLI-D-13-00294.1.

K. E. Trenberth, Y. Zhang, J. T. Fasullo, and S. Taguchi. Climate variability and relationships between top-of-atmosphere radiation and temperatures on Earth. *Journal of Geophysical Research: Atmospheres*, 120(9):3642–3659, 2015. doi: 10.1002/2014JD022887.

S. Twomey. Pollution and the planetary albedo. *Atmospheric Environment*, 8 (12):1251 – 1256, 1974. doi: 10.1016/0004-6981(74)90004-3.

J. J. van der Dussen, S. R. de Roode, S. Dal Gesso, and A. P. Siebesma. An LES model study of the influence of the free tropospheric thermodynamic conditions on the stratocumulus response to a climate perturbation. *Journal of Advances in Modeling Earth Systems*, 7(2):670–691, 2015. doi: 10.1002/2014MS000380.

J. Vial, J.-L. Dufresne, and S. Bony. On the interpretation of inter-model spread in CMIP5 climate sensitivity estimates. *Climate Dynamics*, 41(11):3339–3362, Dec 2013. doi: 10.1007/s00382-013-1725-9.

E. K. Vizy and K. H. Cook. Development and application of a mesoscale climate model for the tropics: Influence of sea surface temperature anomalies on the West African monsoon. *Journal of Geophysical Research: Atmospheres*, 107 (D3), 2002. doi: 10.1029/2001JD000686.

C. J. Wall, D. L. Hartmann, and J. R. Norris. Is the net cloud radiative effect constrained to be uniform over the tropical warm pools? *Geophysical Research Letters*, 2019. doi: 10.1029/2019GL083642.

J. E. Walsh, W. L. Chapman, and D. H. Portis. Arctic cloud fraction and radiative fluxes in atmospheric reanalyses. *Journal of Climate*, 22(9):2316–2334, 2009. doi: 10.1175/2008JCLI2213.1.

D. Walters, I. Boutle, M. Brooks, T. Melvin, R. Stratton, S. Vosper, H. Wells, K. Williams, N. Wood, T. Allen, A. Bushell, D. Copsey, P. Earnshaw, J. Edwards, M. Gross, S. Hardiman, C. Harris, J. Heming, N. Klingaman, R. Levine, J. Manners, G. Martin, S. Milton, M. Mittermaier, C. Morcrette, T. Riddick, M. Roberts, C. Sanchez, P. Selwood, A. Stirling, C. Smith, D. Suri, W. Tennant, P. L. Vidale, J. Wilkinson, M. Willett, S. Woolnough, and P. Xavier. The Met Office Unified Model Global Atmosphere 6.0/6.1 and JULES Global Land 6.0/6.1 configurations. *Geoscientific Model Development*, 10(4):1487–1520, 2017. doi: 10.5194/gmd-10-1487-2017.

H. Wang and W. Su. Evaluating and understanding top of the atmosphere cloud radiative effects in Intergovernmental Panel on Climate Change (IPCC) Fifth Assessment Report (AR5) Coupled Model Intercomparison Project Phase 5 (CMIP5) models using satellite observations. *Journal of Geophysical Research: Atmospheres*, 118(2):683–699, 2013. doi: 10.1029/2012JD018619.

W. Washington and C. Parkinson. *An Introduction to Three-Dimensional Climate Modeling*. University Science Books, 2 edition, 02 2005. ISBN 1-891389-35-1.

B. A. Wielicki, B. R. Barkstrom, E. F. Harrison, R. B. Lee III, G. L. Smith, and J. E. Cooper. Clouds and the Earth's Radiant Energy System (CERES): An Earth Observing System Experiment. *Bulletin of the American Meteorological Society*, 77(5):853–868, 1996. doi: 10.1175/1520-0477(1996)077<0853:CATERE>2.0.CO;2.

B. A. Wielicki, T. Wong, R. P. Allan, A. Slingo, J. T. Kiehl, B. J. Soden, C. T. Gordon, A. J. Miller, S.-K. Yang, D. A. Randall, F. Robertson, J. Susskind, and H. Jacobowitz. Evidence for large decadal variability in the tropical mean radiative energy budget. *Science (New York, N.Y.)*, 295(5556):841–844, 2002. doi: 10.1126/science.1065837.

L. J. Wilcox, E. J. Highwood, and N. J. Dunstone. The influence of anthropogenic aerosol on multi-decadal variations of historical global climate. *Environmental Research Letters*, 8(2):024033, 2013. doi: 10.1088/1748-9326/8/2/024033.

M. Wild. Discrepancies between model-calculated and observed shortwave atmospheric absorption in areas with high aerosol loadings. *Journal of Geophysical Research: Atmospheres*, 104(D22):27361–27371, 1999. doi: 10.1029/1999JD900925.

M. Wild, A. Ohmura, H. Gilgen, and E. Roeckner. Validation of general circulation model radiative fluxes using surface observations. *Journal of Climate*, 8(5):1309–1324, 1995. doi: 10.1175/1520-0442(1995)008<1309:VOGCMR>2.0.CO;2.

M. Wild, C. N. Long, and A. Ohmura. Evaluation of clear-sky solar fluxes in GCMs participating in AMIP and IPCCAR4 from a surface perspective. *Journal of Geophysical Research: Atmospheres*, 111(D1), 2006. doi: 10.1029/2005JD006118.

M. Wild, D. Folini, C. Schär, N. Loeb, E. G. Dutton, and G. König-Langlo. The global energy balance from a surface perspective. *Climate Dynamics*, 40(11): 3107–3134, 2013. doi: 10.1007/s00382-012-1569-8.

M. Wild, D. Folini, M. Z. Hakuba, C. Schär, S. I. Seneviratne, S. Kato, D. Rutan, C. Ammann, E. F. Wood, and G. König-Langlo. The energy balance over land and oceans: an assessment based on direct observations and CMIP5 climate models. *Climate Dynamics*, 44(11):3393–3429, 2015. doi: 10.1007/s00382-014-2430-z.

M. Wild, A. Ohmura, C. Schär, G. Müller, D. Folini, M. Schwarz, M. Z. Hakuba, and A. Sanchez-Lorenzo. The Global Energy Balance Archive (GEBA) version 2017: a database for worldwide measured surface energy fluxes. *Earth System Science Data*, 9(2):601–613, 2017. doi: 10.5194/essd-9-601-2017.

S. Wong, E. J. Fetzer, M. Schreier, G. Manipon, E. F. Fishbein, B. H. Kahn, Q. Yue, and F. W. Irion. Cloud-induced uncertainties in AIRS and ECMWF temperature and specific humidity. *Journal of Geophysical Research: Atmospheres*, 120(5):1880–1901, 2015. doi: 10.1002/2014JD022440.

R. Wood. Stratocumulus clouds. *Monthly Weather Review*, 140(8):2373–2423, 2012. doi: 10.1175/MWR-D-11-00121.1.

R. Wood and C. S. Bretherton. On the relationship between stratiform low cloud cover and lower-tropospheric stability. *Journal of Climate*, 19(24):6425–6432, 2006. doi: 10.1175/JCLI3988.1.

D. F. Young, P. Minnis, D. R. Doelling, G. G. Gibson, and T. Wong. Temporal interpolation methods for the Clouds and the Earths Radiant Energy System (CERES) experiment. *Journal of Applied Meteorology*, 37(6):572–590, 1998. doi: 10.1175/1520-0450(1998)037<0572:TIMFTC>2.0.CO;2.

M. D. Zelinka, T. A. Myers, D. T. McCoy, S. Po-Chedley, P. M. Caldwell, P. Ceppi, S. A. Klein, and K. E. Taylor. Causes of higher climate sensitivity in CMIP6 models. *Geophysical Research Letters*, 2020. doi: 10.1029/2019GL085782.

Ning Zeng. Drought in the Sahel. *Science*, 302(5647):999–1000, 2003. doi: 10.1126/science.1090849.

M. H. Zhang, W. Y. Lin, S. A. Klein, J. T. Bacmeister, S. Bony, R. T. Cederwall, A. D. Del Genio, J. J. Hack, N. G. Loeb, U. Lohmann, P. Minnis, I. Musat, R. Pincus, P. Stier, M. J. Suarez, M. J. Webb, J. B. Wu, S. C. Xie, M.S. Yao, and J. H. Zhang. Comparing clouds and their seasonal variations in 10 atmospheric general circulation models with satellite measurements. *Journal of Geophysical Research: Atmospheres (19842012)*, 110(D15), 2005. doi: 10.1029/2004JD005021.

C. Zhou, M. D. Zelinka, and S. A. Klein. Impact of decadal cloud variations on the Earth's energy budget. *Nature Geoscience*, 9:871–875, 2016. doi: 10.1038/ngeo2828.

C. Zhou, M. D. Zelinka, and S. A. Klein. Analyzing the dependence of global cloud feedback on the spatial pattern of sea surface temperature change with a Green's function approach. *Journal of Advances in Modeling Earth Systems*, 9 (5):2174–2189, 2017. doi: 10.1002/2017MS001096.

L. Zhou, R. E. Dickinson, Y. Tian, R. S. Vose, and Y. Dai. Impact of vegetation removal and soil aridation on diurnal temperature range in a semiarid region: Application to the Sahel. *Proceedings of the National Academy of Sciences*, 104 (46):17937–17942, 2007. doi: 10.1073/pnas.0700290104.